

1997 IEEE Nuclear and Space Radiation Effects Conference

Short Course

Applying Computer Simulation Tools to Radiation Effects Problems

**21 July 1997
Snowmass Conference Center
Snowmass Village, Colorado**

Copyright © 1996 by The Institute of Electrical and Electronics Engineers, Inc. All rights reserved. Instructors are permitted to photocopy isolated articles for noncommercial classroom use without fee. For all other copying, reprint, or replication permission, write to Copyrights and Permissions Department, IEEE Publishing Services, 445 Hoes Lane, Piscataway, NJ, 08855-1331

1997 NSREC

SHORT COURSE

SECTION I

Modeling Space Radiation Environments

**Janet Barth
Goddard Space Flight Center**

1997 IEEE NSREC Short Course

Janet Barth

NASA/Goddard Space Flight Center
Earth Sciences Directorate/Code 900
Greenbelt, Maryland 20771

1.0 Introduction	3
2.0 Solar Processes	4
3.0 The Earth's Magnetosphere.....	7
3.1 The Earth's Magnetic Field.....	8
3.1.1 Internal Field Models	9
3.1.2 External Field Models	11
3.2 Magnetic Storms and Sub-Storms.....	13
4.0 Coordinate Systems for Defining the Radiation Environment	15
4.1 The B-L Coordinate System	15
4.2 Magnetic Rigidity & Geomagnetic Attenuation.....	18
4.3 Atmospheric Depth and Rigidity	21
5.0 Naturally Occurring Particles.....	22
5.1 Trapped Protons and Electrons - Earth	22
5.1.1 Origin of Trapped Protons and Electrons	22
5.1.2 NASA's Trapped Particle Models	31
5.1.3 Trapped Proton Distribution	34
5.1.4 Trapped Electron Distribution.....	37
5.1.5 Problems with the AE-8 and AP-8 Models.....	40
5.1.6 Dynamic Models - A Beginning	42
5.2 Trapped Heavy Ions - Earth.....	46
5.3 Trapped Particles - Other Planets.....	47
5.4 Galactic Cosmic Ray Heavy Ions	48
5.4.1 Origin of Galactic Cosmic Ray Heavy Ions	48
5.4.2 Galactic Cosmic Ray Models	51
5.4.3 Distribution of GCR Particles in Space.....	52
5.4.4 Problems with the Models.....	54
5.5 Solar Wind	54
5.6 Solar Particles	54
5.6.1 Origin of Solar Particles.....	55
5.6.2 Solar Proton Models.....	61
5.6.3 Models for Heavier Solar Ions	63
5.6.4 Solar Particle Distribution in Space.....	64
5.6.5 Problems with the Solar Particle Models	66
6.0 Man-made Particles	66
7.0 The Secondary Environment.....	67
7.1 Interactions with Spacecraft Materials	67
7.2 Atmospheric Neutrons.....	68
7.2.1 Origin of Atmospheric Neutrons	68
7.2.2 Atmospheric Neutron Models	69

7.2.3 Problems with the Neutron Models	71
8.0 Summary and Recommendations	72
8.1 Summary of Environment and Available Models	72
8.2 Model Improvements.....	75
9.0 Acknowledgments	76

1.0 Introduction

As the next millennium approaches, we are increasingly dependent on successful space systems, whether they be military, research, or commercial missions. In the 1970s the view was widely held that designing radiation-hardened (rad-hard) spacecraft and systems would become a “non-problem” with the development of inherently radiation-hardened electronic components. Unfortunately that is not the reality of today. In fact, reducing radiation effects on spacecraft systems to manageable levels is more complex than ever. The need for systems with high levels of performance has outpaced the capabilities of available rad-hard components and technology. At the same time, the demand for electronics capacity in commercial markets has greatly decreased the manufacturer’s interest in developing rad-hard components, driving up the cost of rad-hard parts and making them increasingly unavailable. The rad-hard market share is simply too small. The decreased support for radiation hardened component design and technology in the military sector has compounded the problem. Increasingly, system performance requirements must be met by using commercial technologies that have complex responses to the radiation environment.

These device and system trends have required increased use of radiation management techniques, such as, the use of radiation-tolerant components, the use of specialized shielding, system redundancy, effects mitigation and circumvention, criticality analysis, and failure mode analysis. Also, there is a new awareness of the need for investment in research in the area of radiation hardened components.

Today, successful programs rely more than ever on accurate, application specific definitions of the radiation environment. In turn, the accuracy of such definitions depends on the availability of adequate models of the environment. Two criticisms of the radiation environment models are that they don’t reflect the dynamic nature of the environment and that the uncertainty factors are too large. Why have these shortcomings become more important?

Over the past ten years we have seen the emergence of new radiation effects problems, the prime example being single event effects in VLSI devices. And with some recent satellite failures and analysis of anomalies from the CRRES satellite showing that most anomalies were due to deep dielectric charging, there has been increased interest in electron induced charging/discharging problems. Designing a system hardened to both of these hazards requires that the extremes of the environment be evaluated. Unfortunately, many of the older models provide only average values or the extremes of the environment are overestimated.

Another development in spacecraft technology influencing new modeling efforts is the advent of smaller, lighter, low power satellites. Essentially, we are dealing with a problem of designing satellites with greatly reduced built-in shielding, while at the same time, using parts that are more radiation sensitive. This has driven the need for radiation models with lower uncertainty factors so that lower design margins can be applied.

The objectives of this section of the short course are to review the basic physics and theory of the definition of the radiation environment, present the available models, and define the limits of

the applicability of the models to the real environment. Section 2 describes solar processes and explains their importance to understanding the transient and trapped radiation environment in the near-Earth region. Section 3 describes the Earth's magnetosphere and magnetic storms, and Section 4 reviews the coordinate systems that are commonly used to map the spatial distribution of the particles. Section 5 describes the major components of the natural radiation environments that are hazardous to spacecraft, namely, particles trapped in the near-Earth regions and particles transiting near-Earth regions, i.e., galactic cosmic ray heavy ions (GCRs) and solar protons and heavier ions. This section describes the origin of the particle populations and reviews the basic physics that describes their behavior in space. Where possible, measurements of particle populations are given. Finally, the models used to define these environments are described and errors in the models and the limits of their application are discussed. The particle distribution in space as defined by the models is included in these sections. A brief discussion of the environments of other planets is given in Section 6. Section 7 introduces radiation environments resulting from interactions of primary particles with spacecraft structures and with other particles, particularly, atmospheric neutrons. Finally, Section 8 gives summary tables of the components of the radiation environment and the models used to define their distribution and their effects on spacecraft electronics.

2.0 Solar Processes[1]

Because the Sun is a gas, its solar magnetic field is convoluted and highly variable. Both the long term variation in the magnetic field that occurs in a 22-year cycle and the short term variations in the form of intense, short lived storms are responsible for observable changes in the interplanetary and near-Earth radiation levels.

The two storm phenomena occurring on the Sun that affect particle levels are solar flares and coronal mass ejections (CMEs). Solar flares are seen as sudden brightenings in the photosphere near sunspots* (see **Figure 2.1**). Flares are intense releases of energy involving tearing and reconnection of strong magnetic field lines. In fact, they are the solar systems largest explosive events. Large increases in the solar wind density in interplanetary space are measured after solar flare occurrence because the energy released from the flare accelerates particles in the solar plasma to high energies.

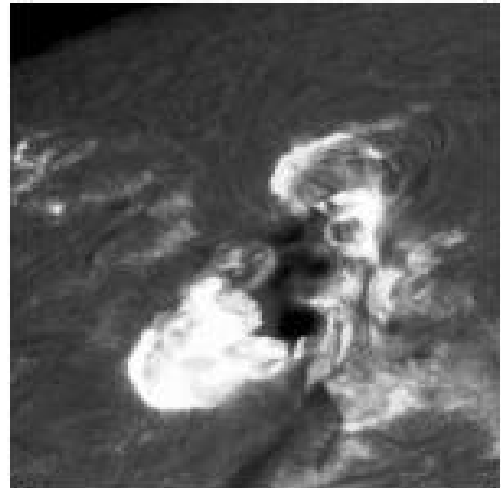


Figure 2.1: Brightening seen with a solar flare.

* cooler areas of the sun seen as dark “spots” through a telescope

CMEs occur in the layer of the sun outside of the photosphere, the chromosphere. The chromosphere can be seen only when filtering out the bright light of the photosphere. In **Figure 2.2**, the chromosphere is seen as a bright rim around the sun. CMEs are observed as large bubbles of gas and magnetic field (see **Figure 2.3**). They release approximately 10^{17} grams of plasma into interplanetary space. The mechanism for the plasma release is not completely understood. CMEs result in large increases in solar wind velocity. It is the shock wave of the plasma release that is associated with particle acceleration and magnetic storms at the Earth. CMEs are poorly associated with flares but, in very large event CMEs, both CMEs and flares occur together.[2] The particle composition of CMEs and solar flares is discussed in Section 5.6.1.

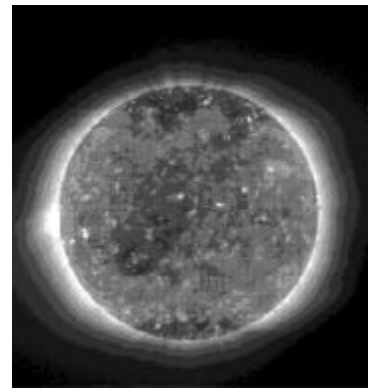


Figure 2.2: Bright rim around the sun is the chromosphere.

The sun's outer atmosphere, the corona (see **Figure 2.4**), extends several solar diameters into interplanetary space. The corona continuously emits a stream of protons, electrons, doubly charged helium ions, and small amounts of other heavy ions, collectively called the solar wind. It was once thought that the region where the solar wind could no longer be detected, i.e., the boundary of the heliosphere,* was not far beyond Jupiter (800 million km). However, the Pioneer 10 spacecraft, presently at 10 billion kilometers from Earth, is still measuring solar wind. Scientists now believe that the boundary could lie as far as 17 billion kilometers from the Earth.[3]

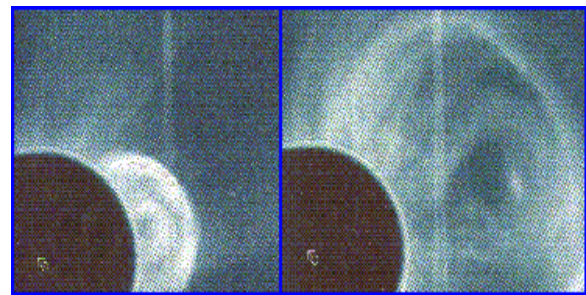


Figure 2.3: Bubble of gas associated with a coronal mass ejection. *NASA/SMM 24 Oct. 1989*

The high temperature of the corona inputs sufficient energy to allow electrons to escape the gravitational pull of the sun. The effect of the electron ejections is a charge imbalance resulting in the ejection of protons and heavier ions from the corona. The ejected gas is so hot that the particles are homogenized into a dilute plasma. The energy density of the plasma exceeds that of its magnetic field so the solar magnetic field is “frozen” into the plasma.

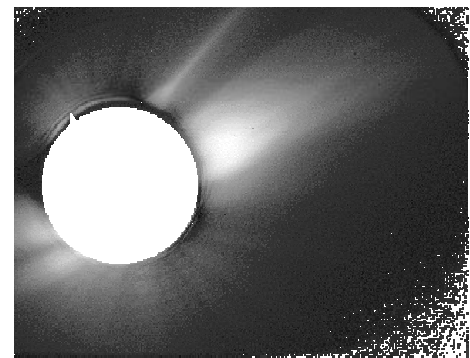


Figure 2.4: The corona extends several solar diameters.

This electrically neutral plasma streams radially outward from the sun at a velocity of approximately 300 to 900 kilometers per second with a temperature on the order of 10^4 to 10^6 K.

*the domain controlled by the solar emissions of plasma and magnetic field extending several hundred times the sun-earth distance

While the solar wind is millions of metric tons of matter moving at a million kilometers per hour, its density is so low that the physics is that of a vacuum. [3] The energies of the particles range from approximately 0.5 to 2.0 keV/nuc. The average density of the solar wind is 1 to 30 particles/cm³. **Figure 2.5** shows that the solar wind velocity and density can vary greatly over a short time period. **Table 2.1** gives the approximate particle composition of the solar wind.

Table 2.1: Solar Wind Particle Composition

Particle	Abundance
Proton	95% of the Positively Charged Particles
He ⁺⁺	~4% of the Positively Charged Particles
Other Heavy Ions	< 1% of the Positively Charged Particles
Electrons	Number Needed to Make Solar Wind Neutral

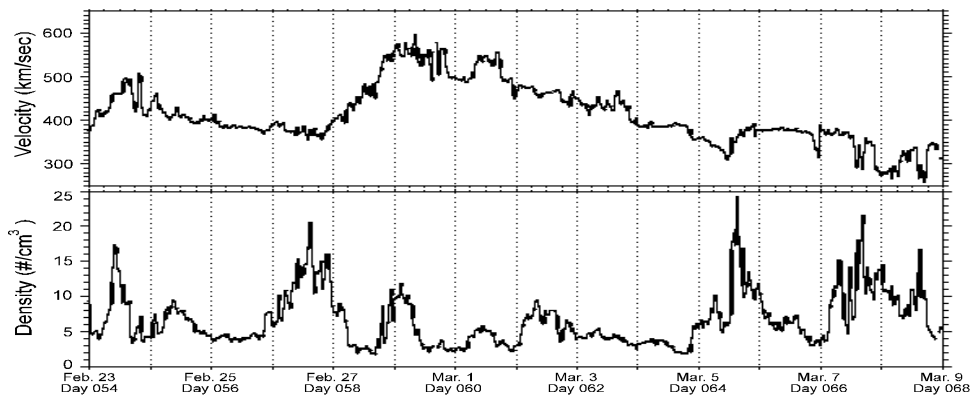


Figure 2.5: The solar wind velocity and density are highly variable and are a function of the activity on the sun.. *SOHO/University of Maryland*

It is well known that the level of activity of the sun varies with time defining “solar cycles”. The solar cycle as a recurrent pattern of solar magnetic activity was first identified in 1843 by the German observer, Schwabe, who found an approximately 11-year cycle in the number of sunspots (see **Figure 2.6**). The 11-year cycle of sunspots corresponds to similar 11-year cycles of other features in the sun’s active regions, including the number of faculae*, the rate of incidence of solar flares and CMEs, and the intensity of coronal x-ray and radio-frequency emissions. The length

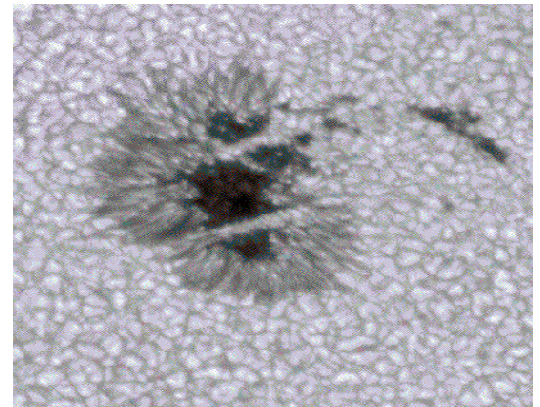


Figure 2.6: Sunspots are regions of highly dense magnetic field. *after Lund Observatory*

*bright regions in the photosphere associated with sunspots

of the solar cycle can be highly variable. From 1645 to 1715, the sunspot activity seemed to disappear. Because temperatures on Earth dropped during that time, those 70 years are known as the little ice age. From 1100-1387, there was an increase in the number of sunspots. Studies of recent solar cycles,[4],[5] Cycles 19 through 22, have determined that the length of the solar cycle over the past 40 years has ranged from 9 to 13 years, with 11.5 being the average (see **Figure 2.7**). For modeling purposes and for defining the environment for spacecraft missions, the solar cycle can be divided into a 7 year maximum phase of high levels of activity and a relatively “quiet” 4 year minimum phase.

The charged particle environment in near-Earth regions is dominated by the activity of the Sun which acts as both a source and a modulator. It is a source of protons and heavier ions via the periodic high energy solar events that accelerate large numbers of particles. The solar wind is also a source of particles trapped in outer regions

of the Earth’s radiation belts. Because galactic cosmic ray heavy ions (GCRs) originate outside of the solar system, they must “fight” against the solar wind to reach interplanetary space. As a result, the GCR levels follow a cyclic pattern reflecting the activity level of the sun. Atmospheric neutrons are secondary products of collisions between GCRs and oxygen or nitrogen atoms in the Earth’s atmosphere, therefore, their levels are also modulated by the solar cycle. Finally, the levels of trapped particles are modulated by both long term variations in solar activity and solar storm events. The impact of the cyclic variation of the sun’s activity will be discussed in more detail in later sections as it applies to specific particle types.

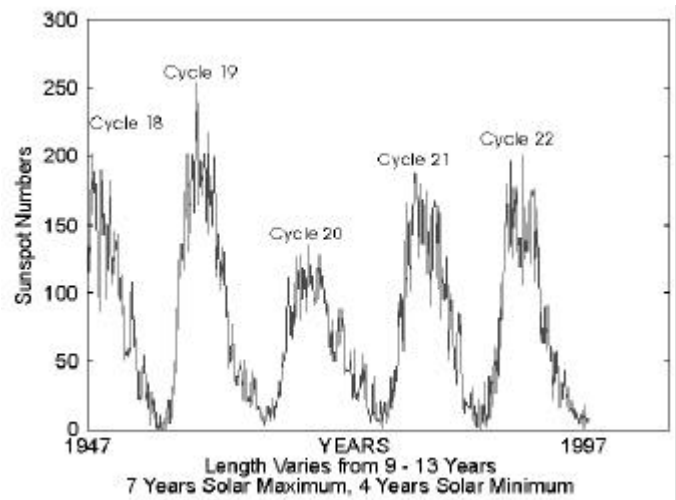


Figure 2.7: Yearly sunspot numbers for the most recent solar cycles. *after Lund Observatory*

3.0 The Earth’s Magnetosphere

The interaction of the solar wind and its associated magnetic field with the Earth’s magnetic field defines the Earth’s magnetosphere (illustrated in **Figure 3.1**). The lower boundary of the magnetosphere is the ionosphere* and the upper boundary is the magnetopause†. In the absence of the solar wind, the Earth’s magnetic field would be shaped like the field of a bar magnet: quiet, nearly symmetric about the magnetic axis, extending outward to long distances, and open at the

* part of the earth’s upper atmosphere (80 to 400 km altitude) where ions and electrons exist in sufficient quantities to propagate radio waves

† the interface between the solar wind plasma and the earth’s magnetic field

poles. The bar magnet representation is accurate up to 4 to 5 Earth radii altitude. The solar wind plasma, with its embedded solar magnetic field, compresses the geomagnetic field until there is balance between the magnetic pressure from the Earth and the momentum pressure from the solar wind forming a “bow shock”. On the dayside, during moderate solar wind conditions, the magnetosphere terminates at the magnetopause at ~10 Earth radii altitude. At the location of this “collisionless” shock, the solar wind plasma cannot penetrate deeply into the geomagnetic field because of its charged particle composition. In fact, 99.9% of the solar wind particles pass around the Earth’s magnetosphere.

The flow of the solar wind around the flanks of the magnetopause stretches the geomagnetic field in the anti-solar direction into a long tail of up to ~300 Earth radii altitude. Some tail field lines are not closed and are connected to the solar magnetic field embedded in the solar wind. The solar wind flow around the Earth’s magnetic field sets up an important contribution to the “external” component of the Earth’s total magnetic field (Section 3.1.2).

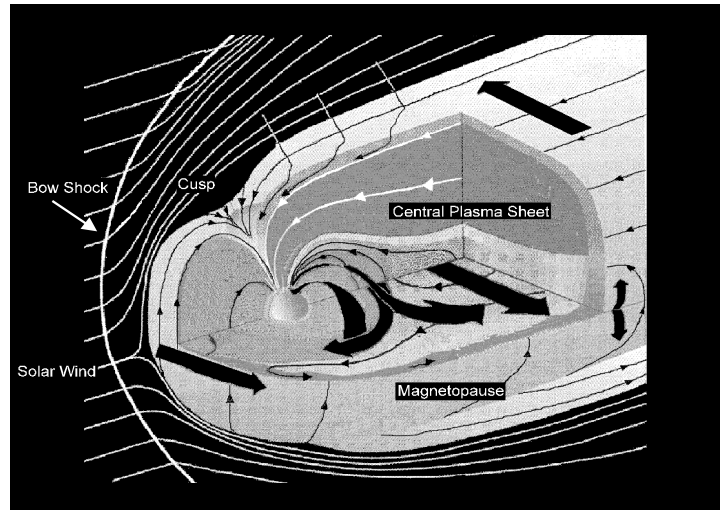


Figure 3.1: The Earth’s magnetosphere is formed by the interaction of the solar wind and the Earth’s magnetic field. *after Heikkila & University of Washington*

As the charged particles in the solar wind move around the Earth, some of the particles cross the Earth’s magnetic field lines and leak into the magnetosphere. Others are trapped by the Earth’s magnetic field and contribute to the formation of the Van Allen belts. Others collect in the magnetotail and create poles of opposite charge, producing a generator which transports particles along magnetic field lines at the poles. The collection of plasma particles in the magnetotail is the neutral plasma sheet seen in Figure 3.1.

3.1 The Earth’s Magnetic Field

The Earth’s magnetic field, B , originates primarily within the Earth’s interior with a small part produced by the ionosphere and the magnetosphere. Approximately 90% of the Earth’s magnetic field can be represented as a dipole, offset slightly from the center of the Earth and inclined 11° from the rotational axis. Hence, the north magnetic pole is located at about 76° north latitude and 100° west longitude, and the south magnetic pole is at approximately 66° south latitude and 139°

east longitude. The magnetic field strength is measured in nanoteslas (nT)^{*} and varies from a few nT at high altitudes to over 50,000 nT at low altitude, high latitude locations.

In reality, the internal component of the geomagnetic field (often referred to as the “main field”) is only quasidipolar due to convection currents in the Earth’s core and varies slowly with time due to changes in the core. Its intensity decreases by about 6% every 100 years and the magnetic dipole moment (~ 30,200 nT) decreases by about 20 nanoteslas per year.

At higher altitudes where the main field is lower, it is important to include the contribution of the external field in the total field strength. The external magnetic field is the sum of the fields transported by the solar wind and those which the solar wind induces in the magnetosphere. The Earth, with its atmosphere and main magnetic field, rotates and moves in its orbit around the sun resulting in periodic variations in the gravitational force, solar illumination, compression, and modifications from solar wind effects. These yield diurnal and seasonal variations in the external field. Also, changes in the interplanetary environment, mostly caused by the sun, result in “disturbance” field variations. The magnitude of the variations depends on the degree of perturbation in the magnetosphere.

The total geomagnetic field value is obtained by a vector addition of the internal and external field components, B_x , B_y , and B_z or B_ρ , B_θ , and B_ϕ , depending on whether a Cartesian or spherical coordinate system is being used. When most of a spacecraft’s orbit is spent in regions where $L < 4$ (see Section 4.1 for a definition of L), it is not necessary to include external field contributions because they are much smaller than the internal field. The external field component with the effects of magnetic storms on the particle environment calculations should be evaluated for spacecraft that spend most of their time in regions in the magnetosphere where $L > 4$.

3.1.1 Internal Field Models

By representing the geomagnetic field as a centered dipole, the internal magnetic field can be calculated to an accuracy of only $\pm 25\%$. The accuracy of models can be greatly improved by using multipole expansions of a potential function based on ground measurements of the field. Starting with the POGO series of satellites, measurements from space further improved the models.

The International Geomagnetic Reference Field (IGRF) is a series of mathematical models of the internal geomagnetic field and its secular variation. Each model consists of a set of spherical harmonic (Gauss) coefficients, g_n^m and h_n^m , in a series expansion of the following geomagnetic potential V :

$$V = a \sum_{n=1}^N \sum_{m=0}^n (a/r)^{n+1} [g_n^m \cos m\mathbf{f} + h_n^m \sin m\mathbf{f}] P_n^m(\cos \mathbf{q}) \quad (3.1)$$

* 1 nanotesla = 1 gamma = 10^{-5} gauss

where $a = 6371.2$ km (the mean radius of the Earth), r is the radial distance from the center of the Earth, f is the east longitude, q is the geocentric colatitude, and $P_n^m(\cos q)$ is the associated Legendre function of degree n and order m , normalized according to the convention of Schmidt.[6] The g_n^m and h_n^m coefficients are in units of nanotesla (nT).

The first IGRF model, IGRF 1965, was adopted by the International Association of Geomagnetism and Aeronomy (IAGA) in 1968. Several revisions or updates have been issued. Newer versions of the IGRF included the Definitive Geomagnetic Reference Fields (DGRFs) issued in 5-year epochs. These are called “definitive” because it is unlikely that the data sets will be improved significantly. The most recent IGRF model, the IGRF95,[7] contains IGRF models at 5-year epochs for 1900 to 1940, DGRF models at 5-year epochs for 1945 to 1990, and the IGRF95 for 1995 including time variation terms for up to the year 2000. To obtain magnetic field values for dates between the 5-year models, linear interpolation between the 5-year DGRF (or IGRF) models is recommended by the authors.

Figures 3.1.1.1 and 3.1.1.2 show magnetic field contours calculated with the IGRF95 model

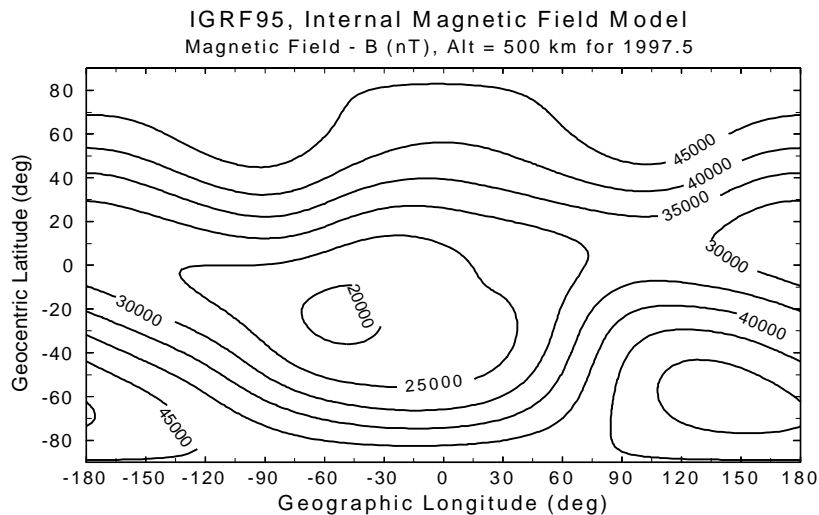


Figure 3.1.1: Magnetic field contours for 500 km altitude. Note the depression in the field strength in the South Atlantic region.

on a world map for altitudes of 500 km and 36,000 km. Figure 3.1.1.1 clearly shows the depression in the magnetic field in the South Atlantic caused by the 11° angle between the magnetic and geographic axes. This magnetic field sink causes charged particles to be trapped at low altitudes (<1000 km) forming the South Atlantic Anomaly (SAA). The figure also shows the multipole nature of the field. Figure 3.1.1.2 shows that, at higher altitudes, the internal magnetic field strength is greatly reduced making the contribution of the external field more important.

The IGRF95 model can be downloaded from NASA/Goddard's National Space Science Data Center (NSSDC). To simplify the use of the models, the NSSDC also distributes computer codes that calculate the field magnitude for latitude, longitude, and altitude positions from the IGRF models. Table 8.1.3 lists the information for obtaining these codes and models.

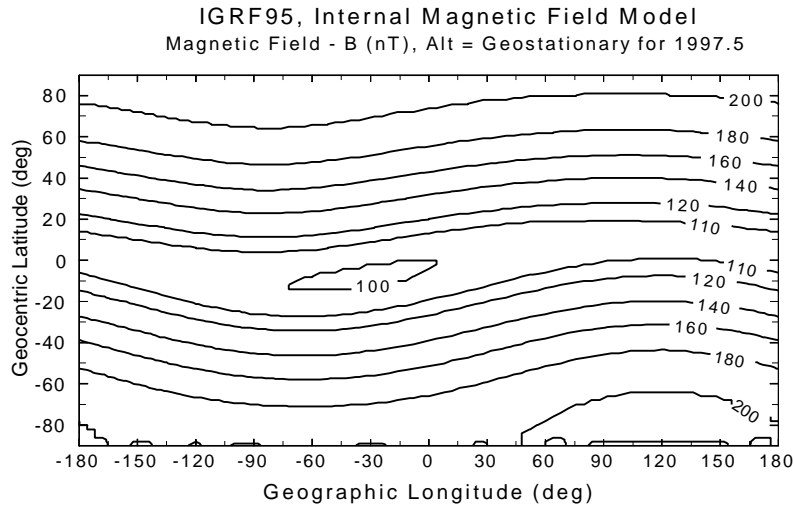


Figure 3.1.2: Magnetic field contours at 36,000 km altitude. The field strength is considerably reduced from the 500 km values.

3.1.2 External Field Models

The spherical harmonic coefficients described in Section 3.1.1 are not adequate to model the Earth's external magnetic field because the field does not lend itself to spherical-harmonic analysis. Separate models of the external field are constructed, and these contributions are added to the components of the main field.

The external field is much less stable than the internal field, and the factors contributing to the external field are not completely understood. The three main components used to construct external field models are the magnetopause current, the neutral sheet current, and the ring current. (See **Figure 3.1.2.1**) The magnetopause current is produced directly by the interaction of the solar wind and the geomagnetic field. It creates the magnetopause in which the current flows, confining the geomagnetic field to the magnetosphere. The neutral sheet current is driven by the dynamo-generated potential across the magnetosphere formed when negatively charged solar wind electrons are deflected to the right side of the Earth (as seen from the sun) and positively charged proton and ions are deflected to the left. (See **Figure 3.1.2.2**) This current causes the polar-cap field lines to be drawn out away from the Earth and into the magnetotail. The ring current consists of trapped ions and electrons in the 20 to 50 keV range flowing longitudinally around the Earth in the region where field lines have a more dipolar shape, i.e., at ~2 to 7 Earth

radii. The net ring current flows westward causing an outward displacement of field lines. The ring current reduces the magnetic field interior to the ring current and increases the field exterior to it.

Unlike the internal field, there is not a standard model for the external field. Two models are currently in use by the radiation effects community. The first is the Olson-Pfitzer tilt dependent model [8] released in 1977. The model is an analytic representation of the three current sources discussed above represented in Cartesian coordinates. It is based on 37,000 measurements points from the OGO-3 and -5 for the inner magnetosphere and the Explorer -33 and -35 for the tail. The major drawback of the Olson-Pfitzer model is that it only models “quiet” conditions in the magnetosphere. Also, it is not rigorously divergence free. In 1988, the authors released the Olson-Pfitzer Dynamic model. With the new model, the user can multiply the quiet models of the fields of the three current systems by variable strength factors. Unfortunately, the model is valid for only zero degree tilt of the Sun-dipole angle.

The second model is the Tsyganenko-Usmonov [9] released in 1982 and later updated by Tsyganenko in 1987 and 1989.[10] This model also represents all three current sources and includes tilt dependence. It is based on measurements from the HEO-1 and -2, the Explorer-33, -34, -41, -43, and the IMP -A, -C, -E, -F, -G, -H, -I, and -J and includes ~37,000 data points. The 1989 model contains 26 input parameters to give the user the ability to simulate specific magnetospheric conditions. However, the flexibility of the input parameters can be confusing to novice users, and the code is more difficult than the Olson-Pfitzer model to integrate into existing packages. **Figure 3.1.2.3** illustrates geomagnetic field lines which include the external field disturbances for average quiet conditions using the Tsyganenko 89 model. Field lines calculated for the internal field only with the IGRF95 model are shown on the inset of that figure. The arrows point to the location of the internal field within the total field model. Note that the external field model reflects the distortions induced in the field by the solar wind.

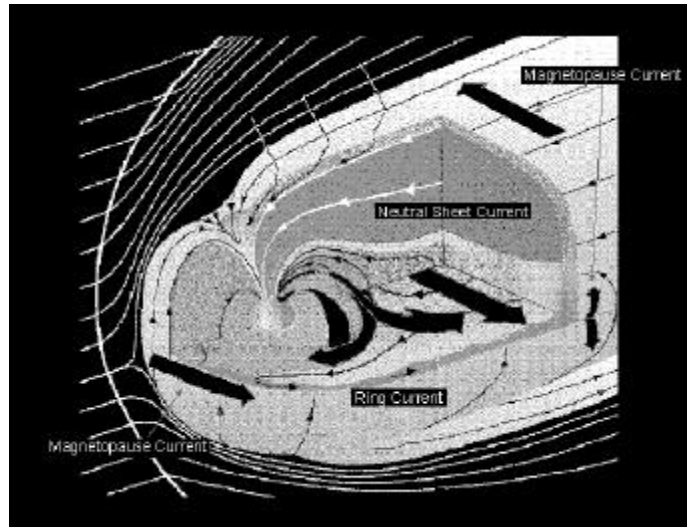


Figure 3.1.2.1: The Earth’s magnetosphere with external field currents indicated. *after Heikkila & University of Washington*

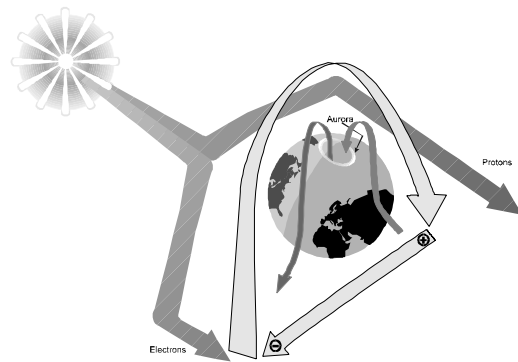


Figure 3.1.2.2: External field current induced in the magnetosphere by the solar wind.

The Olson-Pfitzer model is available from the author and the Tsyganenko model also can be obtained from NASA/Goddard's NSSDC. (Table 8.1.3)

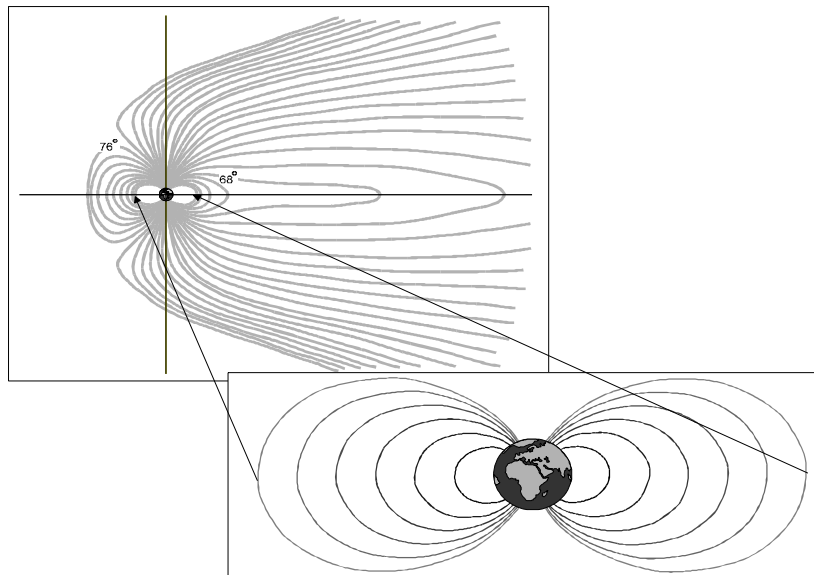


Figure 3.1.2.3: Dipole field lines calculated with internal and external field models.

3.2 Magnetic Storms and Sub-Storms

Major perturbations in the geomagnetic field can occur with changes in the solar wind density (e.g., solar flares), the solar wind velocity (e.g., CMEs), and the orientation of the embedded solar magnetic field. The CMEs and solar flares cause disturbances of the solar wind, and it is the interaction between these disturbances and the Earth's magnetosphere that causes the perturbations called magnetic storms* and substorms. During storms, energy is extracted from the solar wind, is stored, and then dissipated. This process results in a redistribution of particles in the Earth's magnetosphere. [11]

The substorm process begins in the magnetotail. The neutral sheet plasma is heated by the viscous flow of surface currents produced by the solar wind. This heating increases the internal pressure and stretches the tail further. If the tail field lines are disrupted or if the pressure that can be sustained by the tail field lines is exceeded, heated plasma can be ejected Earthward as closed field lines are relaxed to a more dipolar shape carrying charged particles with them. This process is illustrated in **Figure 3.2.1**. Under normal magnetospheric conditions, substorms occur every 2 to 3 hours, however, during magnetic storms, they occur with greater frequency and intensity. [1]

*variations in the Earth's magnetic field which may last from a few hours to 10 days

Major magnetic storms are closely associated with CMEs. A CME can arrive with any magnetic orientation, therefore, not all CMEs affect the Earth. The most violent solar events occur at Earth when the magnetic field lines embedded in the solar wind are directed southward enabling them to connect with those that surround the Earth. The most well known phenomenon associated with magnetic storms is the increase in the intensity and the distribution of the aurora. In fact, the auroras are a good gauge of the intensity of the solar wind. Other phenomena are higher levels of solar protons and heavy ions, redistribution of trapped particles, increased ring current, increased plasma electrons resulting in an increase in spacecraft charging and discharging [12], and power blackouts on Earth. **Figure 3.2.2** shows the mechanism by which increased activity induces the increases in the aurora.

The failure of the ANIK E1 satellite in January 1994 as the result of a CME induced magnetic storm demonstrated the hazard that solar activity can impose on human investment in space. The plot on the left of **Figure 3.2.3** [13] shows the increase in solar wind velocity from the CME. The right plot shows the subsequent build-up of 1 MeV electrons at

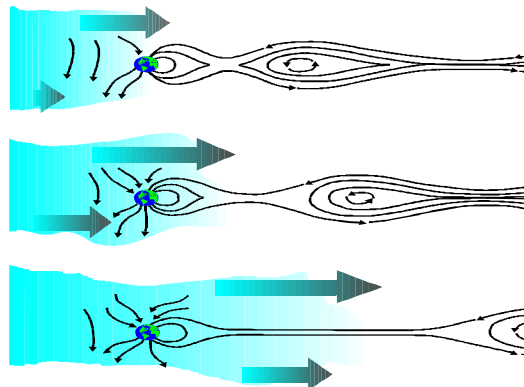


Figure 3.2.1: Plasmoid model of substorms. Particles are injected Earthward.

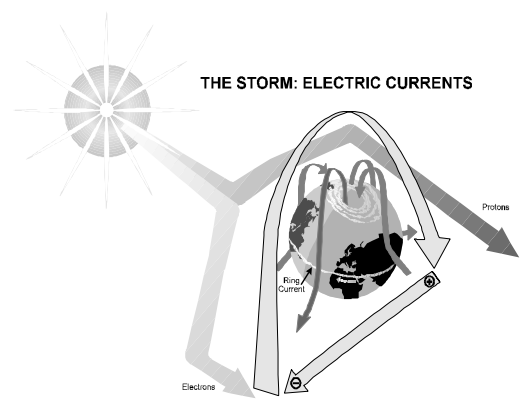


Figure 3.2.2: Induced field currents are increased with a “gusty” solar wind, increasing the aurora.

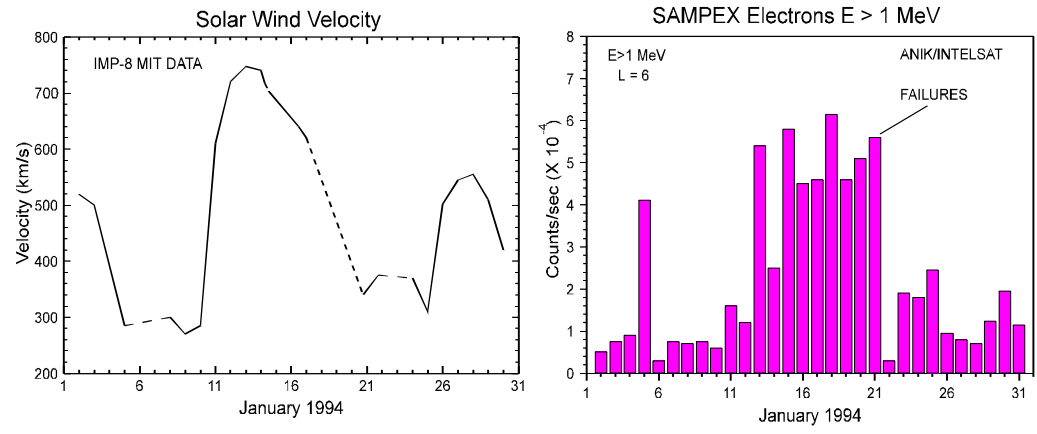


Figure 3.2.3: Solar wind velocity increased due to a solar storm on 10 January 1994 followed by the buildup of electrons at high altitudes. *after Stassinopoulos et al.*

geostationary due to substorm injections. Because the ANIK E1 failure occurred at the end of the build-up, it was concluded that the failure was due to deep dielectric charging.

As with several other phenomena, the number of magnetic storm days shows the same cyclic variation as the solar activity level. **Figure 3.2.4** [14] plots the number of sunspots for a 60-year period, indicating the level of solar activity. Plotted with the sunspot cycle are the number of geomagnetic storm days as measured by the A_p magnetic index. The correlation of the number of storm days with the level of solar activity is clear.

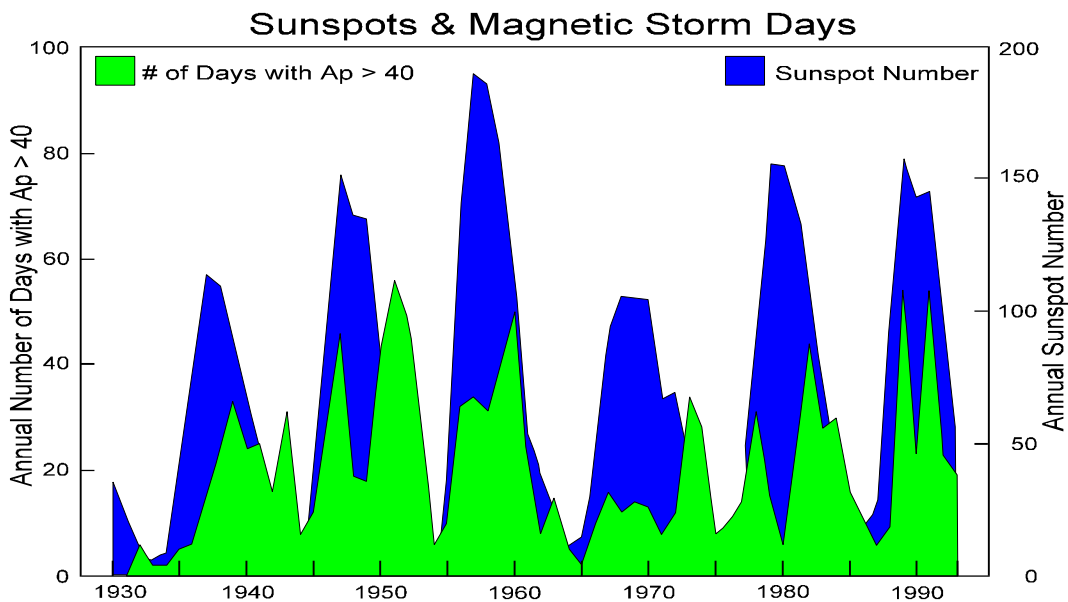


Figure 3.2.4: The number of magnetic storm days correlates closely with the level of solar activity, as measured with sunspot numbers.

4.0 Coordinate Systems for Defining the Radiation Environment

From the processes described in Section 3.0, one can see that the Earth's magnetosphere determines the penetration and distribution of charged particles in the near-Earth regions. The motion of a charged particle is a consequence of the forces acting on it as the particle moves through a non-uniform magnetic field. To understand the distribution of and variations in the particle environment, it is necessary to first have a basic knowledge of the magnetic coordinate systems that best represent particle behavior.

4.1 The B-L Coordinate System

A major contributor to the space radiation hazard is the trapped charged particles. A detailed explanation of their behavior and distribution in space is given in Section 5. A brief description of

their basic motion will be given here to provide background to define the coordinate system that is used to map them in space.

Charged particles become trapped because the Earth's magnetic field constrains their motion. They spiral around the field lines in a helicoidal path while bouncing back and forth between the magnetic poles. Superimposed on these spiral and bounce motions is a longitudinal drift of the particles because of the gradient of the magnetic field. **Figure 4.1.1** illustrates the three motions. When the particle makes a complete azimuthal rotation, it has traced a "drift shell". (See **Figure 4.1.2**)

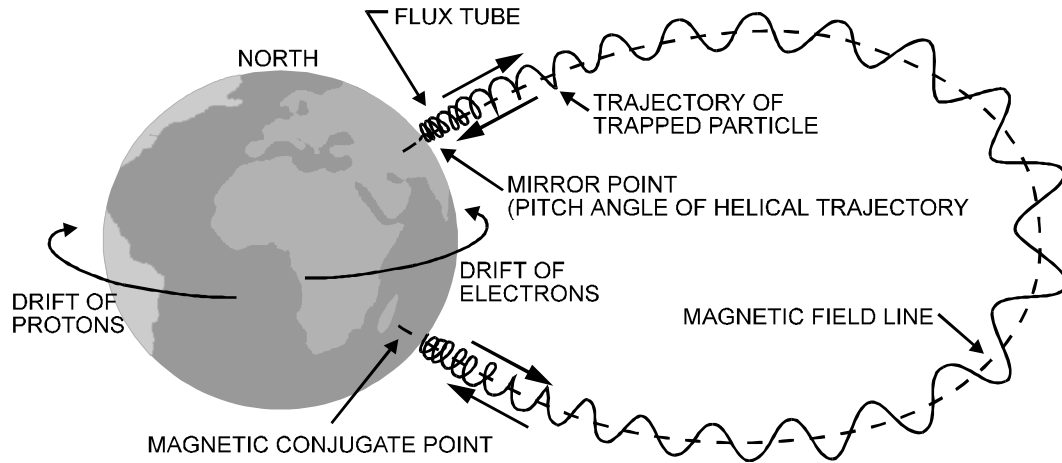


Figure 4.1.1: The three motions of the trapped particles form drift shells. *after Hess*

Mapping trapped charged particles requires consideration of multiple dimensions including species, energy, pitch angle*, altitude, latitude, and longitude. Mapping can be greatly simplified by reducing one or more of the parameters. This was accomplished by McIlwain when he developed the dipole shell parameter, L . In early attempts to map trapped particles in space, it was found that the location of the particle could be reduced from a three dimensional system (latitude, longitude, and altitude) to a two dimensional system. The two coordinates of the McIlwain system are rings of constant magnetic field strength, B , and the dipole shell parameter, L . The L parameter is most simply described as the value that marks the particle drift shells by their magnetic equatorial distance from the center of the Earth.

*The pitch angle α of a particle is the angle between the field vector B and the velocity vector v . When $\alpha = 90^\circ$, all of the motion is perpendicular to the field line and when $\alpha = 0^\circ$, the particle moves in a straight line parallel to the field line.

The B-L coordinate system is defined in terms of geomagnetic coordinates. If the Earth's magnetic field is viewed as a simple dipole, the dipole axis is offset from the rotational axis by 11° . The relationship between geographic coordinates and geomagnetic coordinates is shown in **Figure 4.1.3**. When dipole field lines and particle drift shells are defined in terms of latitude and longitude, it is in the geomagnetic coordinate system.

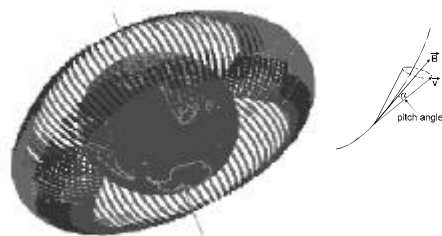


Figure 4.1.2: Drift shell of a trapped particle. *Lamarie et al.*

To gain an understanding of the L parameter, it is useful to define L in terms of a dipole field.

Figure 4.1.4 illustrates a magnetic field line where K_0 is the magnetic dipole moment, I is the geomagnetic latitude, and R is the radial distance to point B on the field line. R_0 is the radial distance to the field line where it crosses the magnetic equator. The field line can be mapped by:

$$R = R_0 \cos^2 I \quad (4.1)$$

The parameter L is defined as:

$$L = \frac{R_0}{R_E} \quad (4.2)$$

where $R_E = 6371$ km, the radius of the Earth. Note that although positions on the field line move closer to the Earth as the latitude increases, the L value remains the same. In other words, high L values are calculated for low-earth polar orbits in the high latitude regions.

In the dipole field, the field magnitude B is:

$$B = \frac{K_0}{R_0^3} \frac{\sqrt{4 - 3 \cos^2 I}}{\cos^6 I} \quad (4.3)$$

In reality, the field is not a dipole and the calculation of B and L for a given position in space is more complicated. The magnetic field strength for any point in space can be calculated using the internal and external field models described in Sections 3.1.1 and 3.1.2 and performing a vector addition on the components to obtain the total field strength. The local L is then calculated from the geomagnetic field strength:

$$L^3 = \frac{M}{B_p} F \left(I^3 \frac{B_p}{M} \right) \quad (4.4)$$

where M is the magnetic dipole of the Earth and B_p is the magnetic field strength at point P . F is a function which is not analytic but can be approximated numerically [15] and

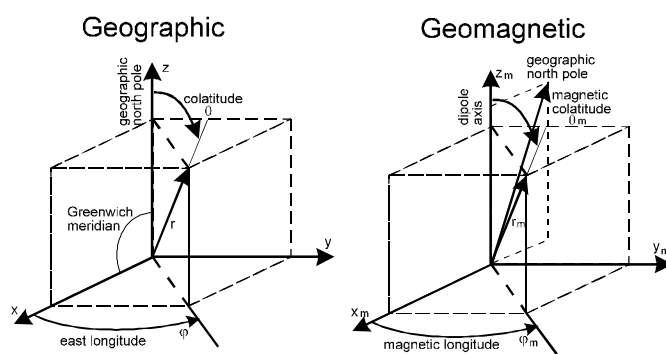


Figure 4.1.3: The geographic and geomagnetic coordinate systems.

$$I = \int_P^{P'} \sqrt{1 - \frac{B}{B_p}} ds \quad (4.5)$$

where B and ds are the magnitude of the field and the arc distance along the line of force. Note that L is independent of geomagnetic longitude. A set of computer codes is available to perform these calculations [16] and can be obtained from NASA/Goddard's NSSDC. (Table 8.1.3)

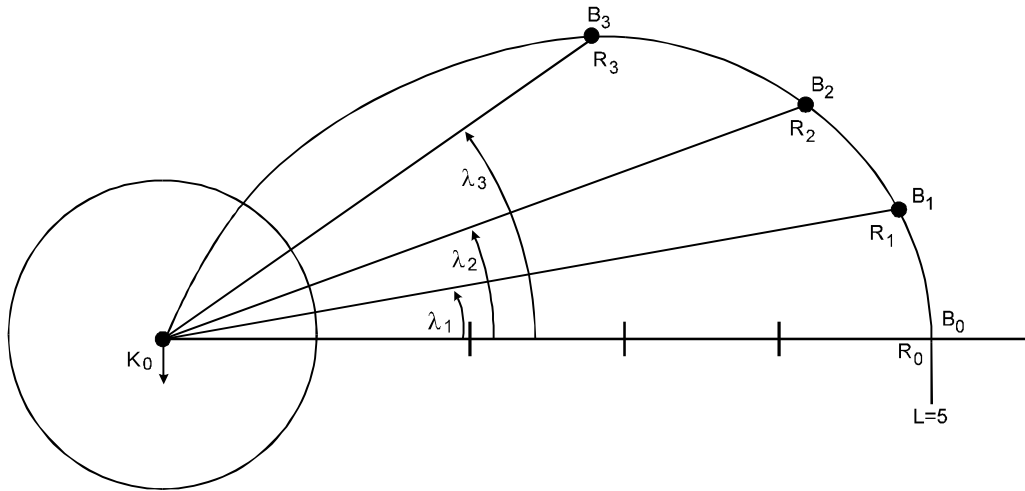


Figure 4.1.4: The B-L magnetic coordinate system is used to map the location of charged particles. *after Stassinopoulos*

4.2 Magnetic Rigidity & Geomagnetic Attenuation

Depending on the orbit of a spacecraft, the Earth's magnetosphere provides varying degrees of protection from transient particles of solar and galactic origin by attenuating the particle fluences. Charged particles that have a low momentum per unit charge are deflected at a certain depth in the magnetosphere and are cut off. The magnetic rigidity of a charged particle is defined as the momentum per unit charge and is measured in units of electron volts/number of charge units, i.e., volts. The gigavolt or GV is a convenient unit for this application. Charged particle cutoffs are a function of geomagnetic latitude, altitude, and the zenith and azimuthal directions and energy of the incident particle.

There is an upper L shell cutoff above which particles are allowed, a lower cutoff below which

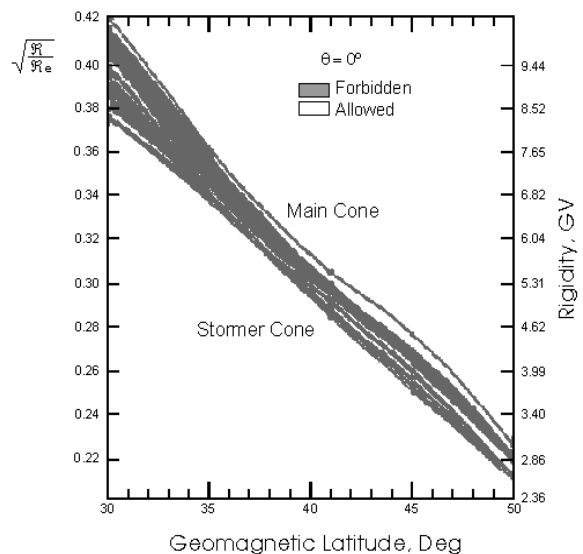


Figure 4.2.1: The cutoff rigidity is strongly dependent on the magnetic latitude. *after Lamarie et al.*

particles cannot penetrate (forbidden regions), and a penumbral region where the transmission of the particles is chaotic.[17] The penumbral region, between the upper and lower cutoffs, complicates the calculations of cutoff values. **Figure 4.2.1** shows the cutoff rigidity as a function of geomagnetic latitude.

Störmer [18] derived the following equation for particle cutoff rigidity, r_s , at the Earth's surface in a dipole field:

$$r_s = \frac{M}{R^2} \left[\frac{\cos^4 I}{\left(1 + \sqrt{1 - \sin e \sin f \cos^3 I}\right)^2} \right] \quad (4.6)$$

where I is the geomagnetic latitude, e is the zenith angle, f is the azimuthal angle measured from the north magnetic axis, M is Earth's dipole moment, and R is the distance from the dipole center of the Earth in units of Earth radii. The Störmer equation shows that, for any direction specified by the zenith and azimuthal angles, the cutoff rigidity decreases with increasing geomagnetic latitude. This means that the high latitude regions are more accessible to transient particles.

The magnetic rigidity is also related to the particle's energy E in MeV by:

$$r = \frac{A}{z} \sqrt{E^2 + 2M_0E} \quad (4.7)$$

where r is the magnetic rigidity in GV, A is the particle's mass in amu, z is the particle's charge, and M_0 is equal to 931 MeV. Because r is a function of the particle's charge, it can be shown that there is an east-west effect on the magnetic cutoff.[19] Positive particles arrive at the top of the atmosphere with greater abundance from the western part of the sky and negative particles from the eastern part of the sky.

While the Störmer theory is useful for theoretical understanding, the dipole approximation is not accurate in the real magnetic field of the Earth. In a real field, the precise values of cutoff rigidity are difficult to obtain because the equation of charged particle motion in a magnetic field does not have a closed form. Shea and Smart [20] have calculated accurate cutoffs in the form of world map isocontours using the IGRF field models and by performing numerical integrations of particle trajectories. Because calculations must be carried out for each point, direction, and magnetic rigidity, this is not a practical method for analyzing particle accessibility to a spacecraft in orbit. In the Cosmic Ray Effects on Microelectronics (CREME) code, Adams *et al.* [21] combined vertical rigidities from Shea and Smart with Störmer theory to calculate transmission histograms as a function of magnetic rigidity. The rigidity for the energies of the particle spectrum is calculated using the rigidity-energy relation given in Equation 4.7. The fluences are then attenuated by the interpolated transmission factor from the rigidity-transmission histogram.

At the time that the CREME model was written, this was the most accurate and computationally practical approach. The shortcoming was that the magnetic fields used for the vertical rigidity calculations only included the contributions of the internal magnetic field with an approximate description of the effects of any large geomagnetic storm. As a result, the important contributions of the external magnetic field and the level of enhanced accessibility caused by

geomagnetic disturbances could not be assessed. Recently, Boberg *et al.* [22] have made modifications to CREME to include the external field contributions as calculated by the Tsyganenko 89 field model for two precalculated orbits (28.5° and 51° inclination at 450 km altitude). The results produced by the updated code agree well with spacecraft measurements. These updates are available in the new version of CREME, CREME96. For other orbits, CREME96 is like old CREME except that it now includes an approximate correction for the external field.

Smart and Shea [17] have also derived useful approximations from Störmer’s equation by normalizing to the Earth’s actual magnetic field. The McIlwain’s B-L coordinate system is used ($\cos^2\lambda = R/L$) with vertical cutoff rigidities (implying that ϵ and $\phi = 0^\circ$) to give:

$$r = \frac{15.96}{L^{-2.001}} \quad (4.8)$$

where r is the cutoff rigidity and L is McIlwain’s dipole shell parameter. With this relation, approximating particle accessibility to orbiting spacecraft becomes a simple matter of calculating L for altitude, latitude, and longitude positions and converting L to rigidity.

By using the rigidity-energy equation given above, histograms are accumulated for the orbit and are used to attenuate the particle energy-fluence spectra of the transient particles. **Figure 4.2.2** illustrates the particle energy-rigidity- L relationship. In the rigidity energy formula, z/A can be approximated with a value of 0.5 for ions $Z > 1$. **Figure 4.2.3** shows

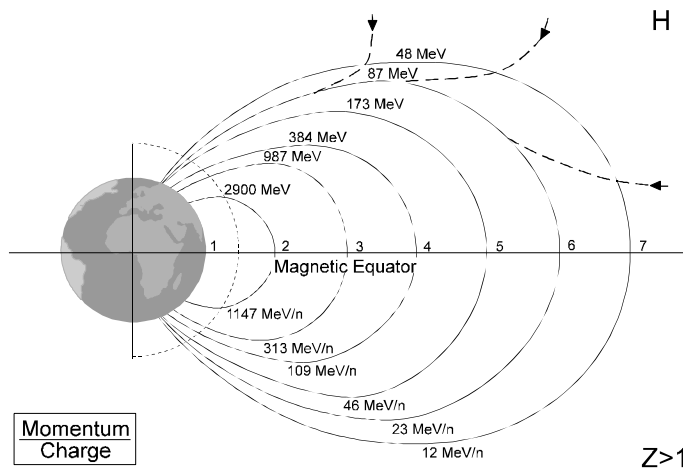


Figure 4.2.2: The relationship between the dipole shell parameter, L , and cutoff rigidity is often used to determine the particle energy required to penetrate the magnetosphere. *after Stassinopoulos*

Calculations of cutoff rigidity are further complicated by the effect of the solid Earth subtending particle paths. By stopping some particles, the Earth produces a “shadow” effect, blocking out some regions that would otherwise be accessible to particles. Adams *et al.* [23] derived a simple correction factor Ω which estimates the portion of the geometry factor occulted by the Earth:

$$\Omega = 2p \frac{1 - \sqrt{(R_E + h)^2 - R_E^2}}{R_E + h} \quad (4.9)$$

where R_E is the Earth’s radius and h is the altitude.

World Map of Geomagnetic Rigidity Contours at 800 km
After Shea & Smart, 1975 and Adams et al, 1981

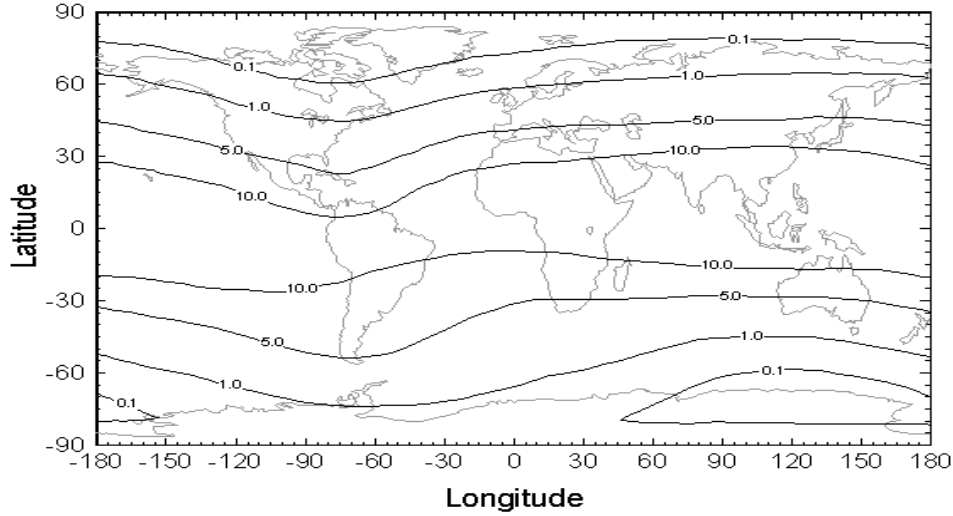


Figure 4.2.3: Magnetic rigidity as calculated by Shea & Smart. Note that rigidity is lower at higher latitudes, allowing increased particle exposure near the poles.

4.3 Atmospheric Depth and Rigidity

The problem of neutron induced single event upsets in avionics [24,25] has resulted in the need for a coordinate system to describe the neutron environment at aircraft altitudes. It is known that the neutron intensities vary with energy, altitude, and latitude. In Reference 25, it is shown that simple models of neutron abundances can be constructed using altitude and latitude coordinates.

A more accurate coordinate system [26,27] replaces altitude with atmospheric depth (mass of air per unit area above the observation point) and latitude with vertical cutoff rigidity.* Vertical cutoff rigidity was discussed in Section 4.2. The rigidity is strongest at the magnetic equator where a particle must have a rigidity of ~15 GV to penetrate and weakest at the poles where particles need a rigidity of < 1 GV to penetrate. The second coordinate, atmospheric depth x in units of g/cm^2 is given as:

$$x = 1033 \exp \left\{ - \left[0.4534 - (1.17 \times 10^{-9}) \times \left| \frac{A - 1.05 \times 10^5}{1 \times 10^3} \right|^{3.58} \right] \left(\frac{A}{1 \times 10^3} \right) \right\} \quad (4.10)$$

where A is the altitude in feet. Atmospheric depth is used because atmospheric conditions have an effect on the measured particle intensity.

*Neutrons are the products of interactions between galactic cosmic ray heavy ions and particles in the atmosphere. Therefore, the transport of the primary cosmic ray particles is important in determining neutron distributions.

5.0 Naturally Occurring Particles

The particles trapped in the near-Earth environment are composed of energetic protons, electrons, and heavy ions. The transient radiation consists of galactic cosmic ray particles and particles from solar events (CMEs and flares). The cosmic rays have low level fluxes with energies up to TeV and include all ions in the periodic table. The solar eruptions produce energetic protons, alpha particles, heavy ions, and electrons. Space also contains a low energy plasma of electrons and protons with fluxes up to 10^{12} cm²/sec. In the trapped particle regions, the plasma is the low energy (< 0.1 MeV) component of the charged particles. In the outer regions of the magnetosphere and in interplanetary space, the plasma is associated with the solar wind. Because of its low energy, the plasma is easily stopped by thin layers of material so it is not a hazard to most spacecraft electronics. However, it is damaging to surface materials and can contribute to spacecraft surface charging and discharging problems.[28,29]

5.1 Trapped Protons and Electrons - Earth

The trapped particles pose a significant radiation threat to electronic systems and humans. There is large variation in the level of hazard depending on the orbit of the spacecraft. Both the protons and electrons contribute to total ionizing dose damage. For some electronic parts, single event effects induced by protons are also a hazard. Protons also contribute to displacement damage. Protons are especially problematic because of their high energies and penetrating power. As mentioned above, low energy electrons are the cause of electrostatic discharging which can be a serious problem for spacecraft in higher altitude orbits (e.g., geostationary) where they are exposed to more intense electron populations. Higher energy electrons can penetrate into the spacecraft, collect in insulator materials, and discharge causing damage to electronics. In fact, an analysis of system anomalies from the CRRES satellite showed that most of the anomalies were related to deep dielectric discharging.[30]

5.1.1 Origin of Trapped Protons and Electrons

The International Geophysical Year (1957-58) was an 18-month period of intense scientific exploration of the physical aspects of the Earth. Thousands of scientists from 67 nations worked together, performing a variety of experiments and observations and sharing their results. The first artificial satellites, SPUTNIK and EXPLORER, were launched as part of this program. It was the EXPLORER 1, launched in 1958, that helped determine that the Earth is surrounded by radiation belts. The belts were named for James Van Allen who designed the on-board instruments and interpreted the collected data. **Figure 5.1.1.1** is an artist's representation of the Van Allen belts. [31] Note that the particles are divided into an "inner" belt centered at about 1.5 earth radii and an "outer" belt at about 5.0 earth radii. In between the belts is the "slot" region which is

often thought of as being devoid of high energy trapped particles. We will see in later sections that this is not true. Another feature shown in the illustration is the high latitude protrusions of the outer zone belt (often referred to as the “horns”) that wrap around the inner zone.

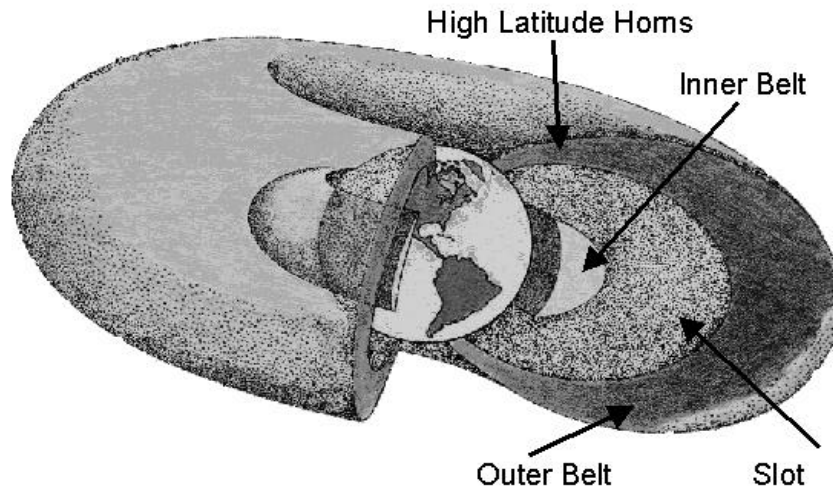


Figure 5.1.1.1: An artist's representation of the Van Allen belts. *from BIRA/IASB*

The energetic charged particles trapped in the Van Allen belts are protons, electrons, and heavier ions. The electrons move at speeds near the speed of light, therefore, they must be analyzed by using relativistic theory. Protons and other heavy ions are much slower. The Earth's atmosphere is the lower boundary of the radiation belts due to a particle loss mechanism that will be discussed later in this section. The upper boundary is determined by the strength of the geomagnetic field. As the distance from the Earth increases, the magnetic field decreases to the point where stable trapping can no longer occur.

While a number of possible sources for the trapped particles have been identified, we do not have a complete understanding of precisely where they come from or how they are accelerated to high energies. The solar wind was discussed as a possible source (Section 2). Some solar wind particles may cross magnetic field lines and leak into the magnetosphere, and others may collect in the magnetotail in the neutral plasma sheet and be ejected Earthward during times of increased geomagnetic activity. Also, ions and electrons from the ionosphere may diffuse out of the polar ionosphere and escape into the magnetotail regions. From the magnetotail, these particles can become energized and be ejected into the trapping regions. The primary source of inner zone particles is referred to as cosmic ray albedo neutron decay (CRAND). The primary cosmic ray particles from interplanetary space collide with atmospheric atoms, producing neutrons that decay into energetic protons and electrons. Also, interplanetary particles that have been accelerated by interplanetary shock waves or in the magnetosphere of other planets, and low energy components of the galactic cosmic rays (See Section 5.2) may find their way into the trapped radiation regions. *In situ* acceleration occurs during magnetic storms when low energy particles that are already trapped are transported to lower L-shells, thereby, increasing their energy.[32]

The plasma sheet (see Figure 3.1) in the Earth's magnetotail is a mixture of particles from several of the sources mentioned above. By the process described in Section 3.2, particles in the plasma sheet convect toward the Earth and become accelerated and trapped in the radiation belts during magnetospheric substorms.

Whatever the source, the protons and electrons become "trapped" because the Earth's magnetic field constrains their motion perpendicular to the magnetic field vector. The electromagnetic Lorentz force is directly responsible for restraining a trapped charged particle and keeping it well within a defined region around the Earth*. It is given by:

$$\frac{d\mathbf{p}}{dt} = q\mathbf{v} \times \mathbf{B} \quad (5.1)$$

where \mathbf{p} is the momentum, q is the charge, \mathbf{v} is the velocity, and \mathbf{B} is the magnetic field. The two components of the instantaneous velocity vector are the component parallel to the magnetic field and the component perpendicular to the field. As a result of the forces acting on the particles, they spiral around magnetic field lines, oscillating back and forth between the northern and southern hemispheres. Because of the non-uniformity of the geomagnetic field, the particles do not mirror back to exactly the same point from which they started. Therefore, superimposed on the spiral and bounce motions is the slow westward drift of protons and the eastward drift of electrons. (see Figure 4.1.1) The opposite direction of the drift is a result of the opposite charges of the particles producing opposite spiral directions. The frequency of the spiral motion (gyration) at 1000 km altitude is about 0.5 Mhz for very low energy electrons and 300 Mhz for low energy protons. As energy increases, the period decreases because of the greater relativistic mass. The bounce period at 1000 km is about 1 second for 1 MeV protons and about 0.1 second for 1 MeV electrons. It takes about 1/2 hour for 1 MeV protons to complete an azimuthal drift cycle at 1000 km and about 1 hour for electrons. Because the frequencies are of different orders of magnitude, the three motions are "uncoupled". These three motions confine the region occupied by the particles to drift shells, designated by the L parameter which was described in Section 4.1.

The best way to characterize and model the trapped radiation environment is to combine theoretical approaches and experimental measurements. To simplify theoretical descriptions, a dipolar magnetic field is assumed. Extensive work was done in the first half of the 20th century to find a general analytic solution to the equation of motion for a charged particle in a dipolar field. It was never found, and particle traces had to be done numerically.[33] In 1963 Alfvén and Fälthammer [34] introduced physical simplifications known as adiabatic theory. The motion of trapped particles in the radiation belts has been described successfully by using three adiabatic

*Electrical fields are important in high-latitude events and auroral phenomena but are not steady, long-lived features of the trapped region. Gravitational forces are weak and are generally ignored. However, mechanical forces in collisions between particles must be accounted for. The high kinetic energies of belt particles means paths are not affected grossly by collisions but cumulative effects will gradually alter the particles motions over extended periods of time.

invariants. They are called adiabatic because, under certain conditions, the invariants remain unchanged with the particle motions.

A short description of the basics of trapped particle morphology with respect to the adiabatic invariants will be given here. If the reader wishes to investigate this topic in more detail, several researchers have provided detailed mathematical derivations of approximations of the motion of trapped particles.[32,35,36] Highly readable descriptions of trapped particle morphology are provided by Vampola [11] and Boscher *et al.*[37]

Associated with each of the three trapped particle motions described above is an adiabatic invariant related to the Hamilton-Jacobi action variable:

$$J_i = \oint_i \left[\mathbf{P} + \frac{q}{c} \mathbf{A} \right] \cdot d\mathbf{l} \quad (5.2)$$

where $d\mathbf{l}$ is a vector line element along the path of integration, \mathbf{P} is the particle momentum, and \mathbf{A} is the magnetic field potential ($\mathbf{B} = \nabla \times \mathbf{A}$). The three invariants of motion are obtained by integrating over the particle's spiral (J_1), bounce (J_2), and drift (J_3) motions. Because of spatial and temporal variations in the magnetic field \mathbf{B} , the action variables are only approximate constants. [32]

The first adiabatic invariant is obtained by integrating over the particle's gyro motion and relates to the conservation of the relativistic magnetic moment M :

$$M = \frac{p_{\perp}^2}{2m_0 \mathbf{B}} \quad (5.3)$$

where p_{\perp} is perpendicular component of the particle momentum and m_0 is the rest mass. The first invariant is called the magnetic moment because a charged particle in cyclotron motion is equivalent to a current loop which has a magnetic moment. A gyrating particle creates its own magnetic field that opposes the external field through its magnetic moment.

It can be shown that conservation of the magnetic moment is also equivalent to:

$$M = \frac{q^2}{2\mathbf{p}m_0} \Phi_c \quad (5.4)$$

where q is the charge, Φ_c is the flux, and m_0 is the particle's rest mass. This means that the magnetic flux through the particle's orbit is conserved. [35] Therefore, the path of a particle gyrating in a magnetic field encloses a fixed amount of flux. The amount of flux depends on the momentum of the particle perpendicular to the field. The radius of gyration \mathbf{r} relates to \mathbf{B} as:

$$\mathbf{r} = \frac{m\mathbf{v}}{\mathbf{B}q} \quad (5.5)$$

therefore, $\mathbf{r} \propto 1/B$. Since the flux (density \times area) $\Phi \propto 1/B^2$, an increase in the $\Delta\mathbf{B}$ results in a decrease in the radius of gyration \mathbf{r} . To maintain a constant M , the momentum perpendicular to \mathbf{B} must increase. The only energy available is from the magnetic field or the particle kinetic energy. In a quiescent field, the perpendicular component to the momentum is obtained from the momentum component parallel to \mathbf{B} . The direct result is the bounce motion of the trapped

particle. [11] When the parallel momentum component becomes zero, the particle is gyrating at its “mirror” B or B_m . This point is named the mirror B because, at this point, the particle reverses direction and bounces back to the other pole, mirroring the motion. In fact, the particle spends most of the time in its bounce period at B_m .

The first adiabatic invariant also explains the acceleration and deceleration of trapped particles due to changes in the magnetic field. These changes are induced by geomagnetic activity which is the result of an increase or decrease in the momentum density of the solar wind. If the magnetic field is increasing, the particle can maintain the magnetic moment, M , by increasing its perpendicular momentum at the expense of the magnetic field. To keep M constant, the gyroradius will decrease, increasing the particle energy. In a decreasing magnetic field, the opposite will occur, i.e., the energy will decrease.

While the first adiabatic invariant relates to the particle motion perpendicular to the magnetic field line, the second adiabatic invariant relates to the motion parallel to the field line. It is obtained by integrating over the particle’s bounce trajectory:

$$J = \int_{-l_m}^{+l_m} P_{\parallel} dl \quad (5.6)$$

where dl is the element of length along the field line segment, l_m is the curvilinear distance of the mirror points from the equator measured along the magnetic field line, and P_{\parallel} is the parallel component of the momentum. If the helicoidal path traced by a trapped particle between the mirror points is bounded by an envelope, the total magnetic field energy contained in the envelope is constant. Again, if the magnetic field increases, the radius of gyration is reduced to compensate (the first invariant). However, the path length must also be reduced to conserve the second invariant which, in turn, raises the mirror points. If the field decreases, the mirror points are lowered, and the particle could be lost into the atmosphere.

The third adiabatic invariant is obtained by integrating over the particle’s drift motion around the Earth:

$$\Phi = \oint \mathbf{A} \cdot d\mathbf{l} = \int_S \mathbf{B} \cdot d\mathbf{S} \quad (5.7)$$

where S is a surface bounded by the azimuthal drift path. In a dipolar magnetic field, [35]

$$\Phi = -\frac{2\mathbf{p}_E R_E^2}{L} \quad (5.8)$$

where L is McIlwain’s L parameter. If the magnetic field is quiescent, the particle will be back at the same location in the field where it started after it completes one drift around the Earth. However, in the approximate 1/2 hour (protons) or 1 hour (electrons) that it takes for the particle to drift around the Earth, a large magnetic storm may have occurred resulting in a substantial change in the particle drift shell. The particle will be in a different field intensity, hence, with a different energy. This violation of the third adiabatic invariant is the primary source of particle acceleration in the magnetosphere.

Over long periods of time, the trapped radiation belts are stable because of four simultaneous processes: the injection of charged particles into the trapping region of the magnetosphere (see Section 3.2), particle acceleration, particle diffusion, and particle loss. The processes occur simultaneously, e.g., some particle loss mechanisms are the result of diffusion, particle acceleration is coupled to diffusion. This makes mathematical treatment of diffusion extremely complicated to solve numerically. A short description of particle diffusion and loss mechanisms will serve our purposes. Discussions of diffusion mechanisms are provided by Roederer in Reference 35 and a detailed description of diffusion processes is given by Schultz and Lanzerotti in Reference 36.

Two diffusion processes important to trapping theory are radial diffusion and pitch angle diffusion. Radial diffusion transports particles across dipolar magnetic field lines and may explain how some solar wind particles reach the magnetosphere. Pitch angle diffusion alters the particle's pitch angle, hence, its mirror point location. In both cases, the Earth's atmosphere causes removal of particles through collisions with atmospheric particles. Radial diffusion transports them to very low L-shells and pitch angle diffusion lowers the mirror points into the atmosphere. Besides particle loss due to collisions with the atmosphere, collisions of trapped particles with atomic hydrogen in the exosphere and particles in the plasmasphere are important loss mechanisms.

When viewed on shorter time scale, trapped particle population levels and distribution in the magnetosphere are not static. The inner zone is a fairly stable population. In contrast, the outer zone flux levels are dynamic to the degree that any variations due to solar cycle are masked by other dynamics. The variability can be over 6 orders of magnitude in the regions of L approximately 2.5 to 5.

One variation is the cyclic rise and fall of the fluence levels in response to the cyclic variation of the sun's activity. The solar cycle has opposite effects on electron and proton levels. The electron and proton flux levels are lowered during the maximum phase of the solar cycle because the increased solar activity increases the atmospheric scale height. This, in turn, results in increased removal rates of trapped particles due to collisions. Hence, the proton population decreases during solar maximum. At the same time that particles are being lost into the atmosphere, electrons are injected into the magnetosphere at greater rates during solar maximum increasing the electron levels above the atmospheric loss rates. Therefore, the net effect on the electrons during solar maximum is an increase in particle populations. Obviously, the magnitude of this variation is not the same for all regions in the magnetosphere.

Several other variations are superimposed on the changes caused by the cyclic nature of solar activity. These include changes in the fluence levels and distribution caused by disturbances in the magnetosphere during storms, local time variations caused by the lack of azimuthal symmetry of the geomagnetic field for $L > 5$, and fluctuations caused by the rotation of the Sun.

Daily variations due to the magnetic field distortion are called diurnal or local time (LT) variations. As **Figure 5.1.1.2** shows, the LT variation becomes more marked with increasing L. A 27-day cyclic variation due to the rotation of the Sun is superimposed on the LT variations. This 27-day variation, as measured by the GOES spacecraft, can be seen in **Figure 5.1.1.3**.

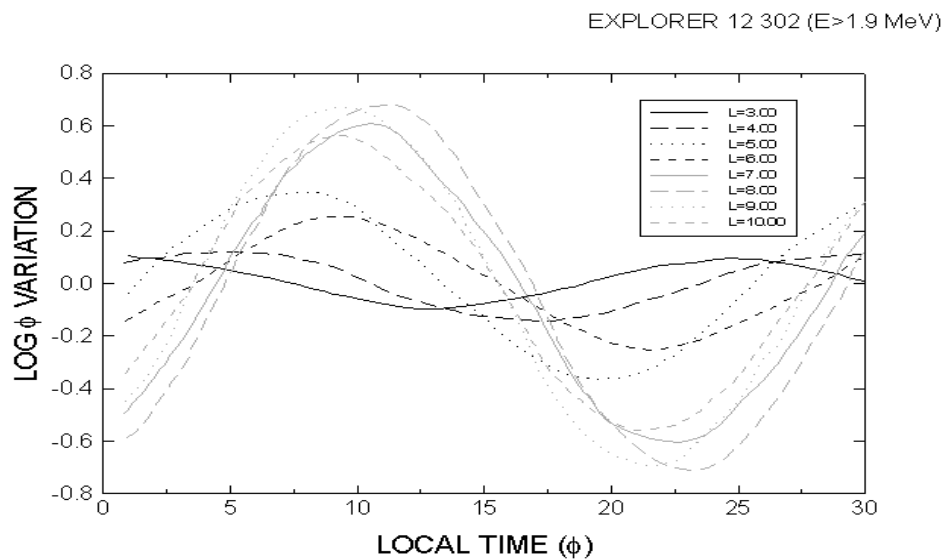


Figure 5.1.1.2: Local time variations of outer zone electrons become more pronounced with increasing L. *after Stassinopoulos*

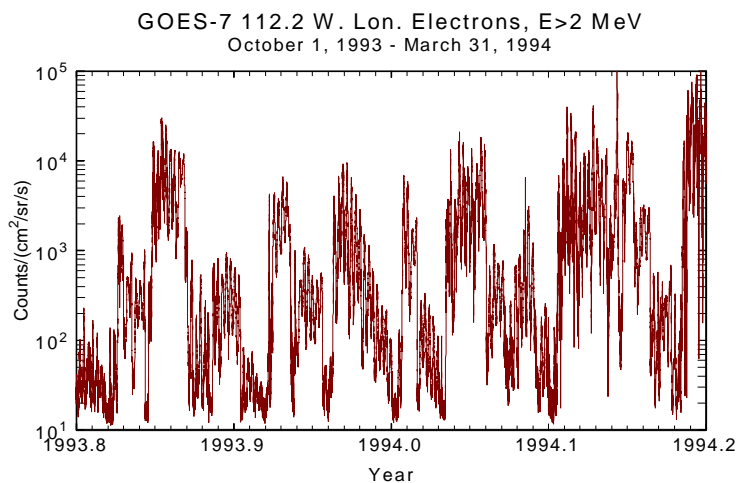


Figure 5.1.1.3: Cyclic variation in electrons in the outer zone due to 27-day solar rotation. *after Nakamura*

The data from the CRRES satellite have given us the first comprehensive look at the near-Earth environment since the late 1960s and early 1970s.[38] Two of the most important discoveries of CRRES were 1) the creation of additional belts of protons and electrons caused by a severe magnetic storm and 2) the existence of high energy electrons (possibly up to 30 MeV) in the near-Earth environment. **Figure 5.1.1.4** shows the output from the CRRES proton monitor (PROTEL) after the magnetic storm on 24 March 1991.[39] The additional belt of high energy trapped protons between L of 2 and 3 is clearly distinguishable.

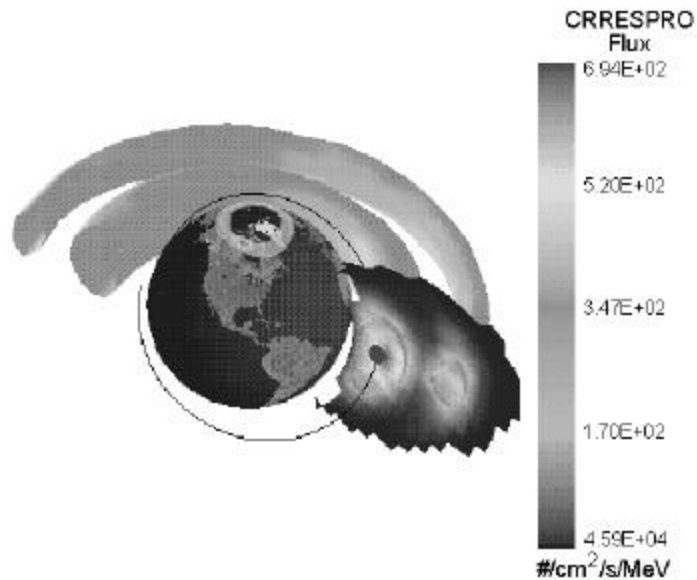


Figure 5.1.1.4: The CRRES satellite measured an additional belt of high energy protons created as a result of the March 1991 magnetic storm. *AF/PL GEOSPACE*

The belt was also measured by Dyer *et al.* with the CREDO instrument on the Shuttle (STS-52) and the UoSAT.[40] **Figure 5.1.1.5** shows a UoSAT orbital pass plotted on a world map with the SAA as predicted by the AP-8 model. The proton counts are given for several positions along the orbit. Note the high counts even though the satellite is well out of the SAA. The authors note that these protons were detected in L regions of approximately 2.6.

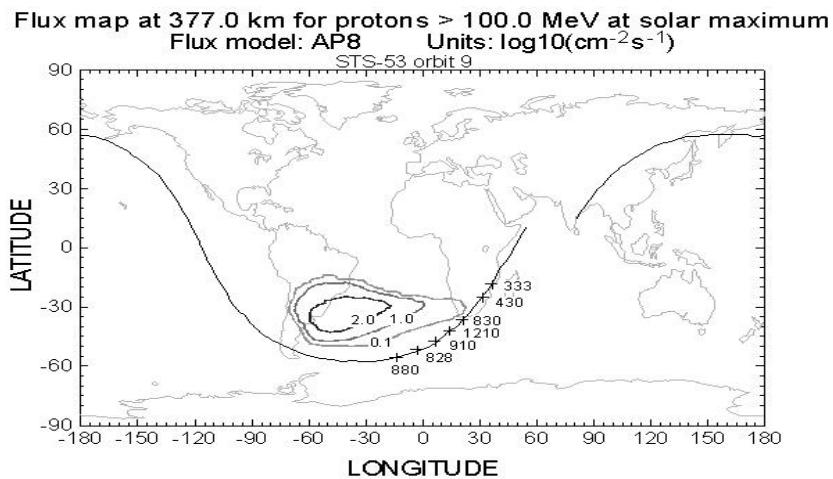


Figure 5.1.1.5: The CREDO instrument on UoSAT-3 measured high levels of protons outside of the SAA. *Dyer et al.*

The lifetime of the additional proton belt is long term but we are not sure of the exact duration. Measurements of the protons by the CREDO instrument on UoSAT-3 and STS-53 show that the belts began decaying immediately but levels were still elevated 22 months after the storm. The Russian METOSAT was also still measuring the additional belt after 2 years.[41]

The CRRES team now believes that the second proton belt was formed when solar protons penetrated down to L values as low as 2 at the magnetic equator during the storm. Measurements from the DMSP satellite also showed proton belt formation during solar minimum.[42]

The CRRES electron monitor (HEEF) measured a new electron belt of high energy electrons (possibly up to 30 MeV) as a result of the March 1991 storm. As with the protons, the additional electron belt appeared in the slot region. The Hipparcos satellite also measured the storm belts. **Figure 5.1.1.6** [43] shows the star-mapper count rate from the Hipparcos satellite as a function of L on a gray scale. The constant bright band at $L \approx 1.5$ is from energetic inner belt protons. At higher altitudes ($L \approx 4$), the counts are due to 4 MeV electrons. Note that the outer zone counts are much more variable in both intensity and distribution than the inner zone. The effect of the March 1991 storm and solar event is striking. Huge numbers of protons and electrons were immediately injected down to $L \approx 2.5$ and the outer zone electrons were enhanced. The figure also shows the slow decay of the new belt.

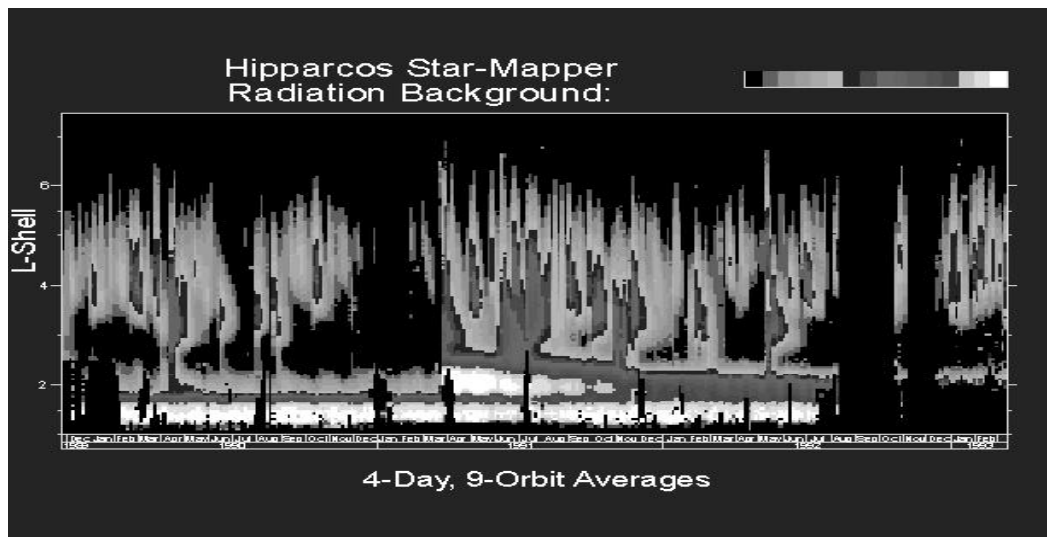


Figure 5.1.1.6: The response of the star-mapper instrument on the Hipparcos satellite clearly shows the injection of particles into low L regions immediately after the March 1991 storm. *Daly et al.*

In addition to the long term storm belts, analysis of data from the CRRES electron monitor showed that high fluxes of electrons can be injected into and removed from the belts in a matter of minutes or less. Electron data from the SAMPEX spacecraft also show that the slot region is periodically filled with electrons that decay or diffuse rapidly. **Figure 5.1.1.7** [44] plots SAMPEX electrons at $E > 0.4$ MeV for 1992. The figure shows the slot region being filled intermittently with large number of electrons. The high degree of variability in the outer zone in terms of intensity and distribution can also be seen in the SAMPEX data. Plots for electron energies greater than 1.0 MeV indicate similar variability in terms of distribution and intensity in the outer zone and filling of the slot region.

To the first order, the trapped particle fluxes can be considered isotropic and omnidirectional. One exception is in the low altitude (300-500 km) region of the South Atlantic Anomaly (SAA). Here the trapped radiation is highly anisotropic due to the east-west effect caused by the azimuthal drift of the protons. Protons arriving from the west must gyrate from above a point in space and those from the east from below the point. The particles from below are more likely to be lost in the atmosphere because they encounter greater atmospheric density. The result is that the proton flux from the west is greater than flux from the east. Also contributing to the anisotropy is the concentration of the particles in the SAA that are near their mirror points meaning they are near 90° equatorial pitch angles. This implies that more particles will be lost into the atmosphere. Anisotropy is higher at low altitudes because of the greater atmospheric density. The net effect is a directional difference of about a factor of 2 to 7.[45] It is important to take the anisotropy into account if a spacecraft maintains a fixed axis throughout the mission.

We also know that the changes in the Earth's internal magnetic field have an effect on the trapped particle distribution in space. Vette [46] stated that the variations in intensity due to the changing field may be 10% over a 20 year period. As early as 1968, scientists observed that the position of the SAA shifts as the field changes.[47]

5.1.2 NASA's Trapped Particle Models [46]

Most of the scientific instruments flown in space in the late 1950s and early 1960s were designed to detect energetic protons and electrons. With the results, scientists gained a general understanding of the near-Earth radiation environment but found differences up to a factor of 10 when making quantitative comparisons between measurements. As spacecraft designers became aware of the influence of radiation effects on spacecraft, the need for a uniform, quantitative description of the trapped particle environment became critical to the success of space programs. The production of enhanced radiation levels by the Starfish explosion and others (see Section 6.0) and the ensuing problem of shortened spacecraft lifetimes emphasized the need for trapped radiation models.

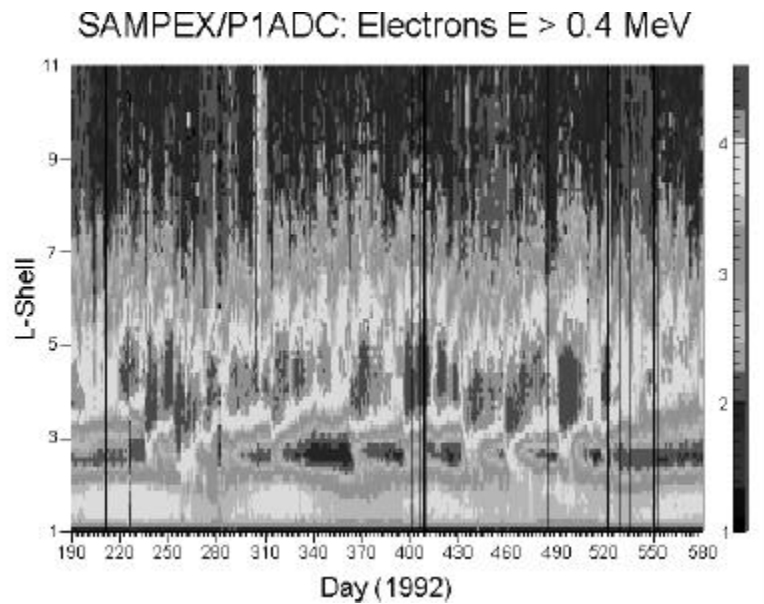


Figure 5.1.1.7: The trapped electrons as a function of L as measured by the SAMPEX spacecraft. Note the variability at $L > 3$ and the filling of the slot region. NASA/GSFC

The first empirical models were developed by Wilmont Hess of NASA/GSFC. Using data from several satellites, he began constructing quantitative radiation models for inner zone protons and electrons. These models were designated as P1, P2, etc. and E1, E2, etc. Starting in 1962 and continuing through the late 1960s, several series of satellites were launched with instruments designed to measure the effects of Starfish, providing a large volume of particle data. In late 1963, James Vette of Aerospace Corporation and later of NASA/GSFC was appointed to lead a trapped radiation environment modeling program jointly funded by NASA and the United States Air Force (USAF). At that time, there were several groups actively involved in trapped particle measurements, including Aerospace Corporation, Air Force Cambridge Research Laboratory (now Phillips Laboratory), Applied Physics Laboratory, Bell Telephone Laboratories, GSFC, Lawrence Livermore Laboratory, Lockheed Missile and Space Corporation, the University of California at San Diego, and the University of Iowa. Each agreed to make their measurements available to the modeling program.

In the 27 years that the program was operative, eight trapped proton models, eight trapped electron models, and one Starfish decay model were released. It is beyond the scope of the Short Course to give all of the details of the models but they are summarized in **Table 5.1.2.1** and Vette gives an overview of them in Reference 46.

Table 5.1.2.1: Summary of Trapped Particle Models

Model Name	Epoch of Data Coverage (mm/yy - mm/yy)	L range	Energy Range (MeV)	Solar Cycle Phase
AE-1	9/62 - 9/63	1.2 - 3.0	0.3 - 7.0	Minimum
AP-1	7/58 - 9/63	1.17 - 3.15	15 - 30	Minimum
AP-2	5/63 - 9/63	1.17 - 3.5	30 - 50	Minimum
AP-3	4/62 - 2/63	1.17 - 2.9	> 50	Minimum
AP-4	9/62 - 9/63	1.17 - 4.6	4 - 15	Minimum
AE-2	10/62 - 6/65	1.1 - 6.3	0.04 - 7.0	Minimum
AE-3	8/59 - 11/65	6.6 (GEO)	0.01-5.0	Minimum
AP-5	7/61 - 4/65	1.2 - 6.6	0.1 - 4.0	Minimum
AP-6	9/62 - 12/65	1.2 - 4.0	4 - 30	Minimum
AP-7	7/61 - 7/66	1.15 - 3.0	50 - 500	Minimum
AE-4	7/59 - 2/68	3.0 - 11.0	0.04 - 4.85	Both
AE-5	12/64 - 12/67	1.2 - 2.8	0.04 - 4.0	Minimum
STD	7/58 - 1/69	1.3 - 2.2	0.04 - 4.0	N/A
AE-5 Projected	7/58 - 2/68	1.2 - 11.00	0.04 - 5.0	Minimum
AE-6	7/58 - 2/68	1.2 - 11.0	0.04 - 5.0	Maximum
AP-8	7/58 - 6/70	1.2 - 6.6	.04 - 500	Both
AEI-7	AE-6 + OV19 Data	1.2 - 11.0	0.04 - 5.0	Both
AE-8	7/59 - 4/78	1.2 - 11.0	0.04 - 7.0	Both

The trapped particle models in current use are the AP-8 for protons and the AE-8 for electrons (The “A” is for Aerospace Corporation.). The AP-8 model [48], released in 1976, was the culmination of a long term effort to include all of the previous models under one common approach and to include all of the data after 1970. After 1977, the modeling budget was significantly reduced so a similar effort to consolidate the electron models into the AE-8 model [49] was not completed until 1983. The formal documentation of that model was released in 1991.

The AP-8 and AE-8 models include data from 43 satellites, 55 sets of data from principal investigator instruments, and 1,630 channel-months of data. By the 1970s, scientific interest had shifted from trapped particles to the plasma regime to determine the physical mechanisms of particle energization and transport, and the focus is likely to remain there. As a result, the number of data sets available for trapped radiation environment modeling has been drastically reduced.

These models are empirical data sets for static conditions. The energy range of the protons included in the AP-8 is 0.04 to 500 MeV. The energy range in the AE-8 electron model is 0.04 to 7.0 MeV. The log of the fluxes at the geomagnetic equator are stored for given energies and L values. Scaled increments of B/B_0 (ratio of the geomagnetic field strength to the strength on the field line at the geomagnetic equator, i.e., the location of the minimum magnetic field value on a field line) are stored with the fluxes. The subroutine TRARA interpolates the AP-8 and AE-8 values in B/B_0 -L space. The models were arranged this way because it provided the best resolution close to the atmospheric cutoff where the fluxes drop off rapidly while not exceeding the limited capacities of the computers available at the time of the model development.

The AP-8 and AE-8 models are available in two versions, one for the minimum phase of the solar cycle and one for the maximum phase.* The fluxes from the models represent averages that one would expect over the solar cycle phase for missions of 6 months duration or greater. Other than reflecting variations in the particle fluence levels due to the solar cycle phases, the models are static and do not reflect variations caused by the slowly changing geomagnetic field or due to magnetic storms and substorms.

Uncertainty factors of 2 have been defined for the AP-8 and AE-8 [48,49]. These represent the statistical uncertainty from combining data from several datasets and do not reflect either long or short term variations in the environment. For limited durations, short term excursions from the model averages can reach orders of magnitude above or below. (see Section 5.1.1)

Because the data came from several satellites and experiments, they had to be normalized to one set of magnetic field values. The field model used for most of the data was the Jenson and Cain 1960 (JC-60) static field model. The exception was the AZUR data used in the AP-8-MAX model. In this case, the GSFC-12/66 field model extrapolated to 1970 was used. Because the models are static and do not reflect changes in the geomagnetic field, they must be accessed with

*The AP-8 models are also distributed in a “compact” form, AP-8-MAC and AP-8-MIC, to facilitate use on small computers.

B and L values calculated with the models that normalized the datasets, i.e., JC-60 (unextrapolated) for AP-8-MIN, AE-8-MIN, and AE-8-MAX and the GSFC-12/66 extrapolated to 1970 for the AP-8-MAX. Calculating fluxes from the models using any other field values may result in large errors in the fluxes. Even though the differences in the calculated B and L are small, there are large gradients in the models in terms of B/B_0 .

The AP-8 and AE-8 models can be obtained from NASA/Goddard's NSSDC. (Table 8.1.3)

5.1.3 Trapped Proton Distribution

Protons are the most important component of the "inner" Van Allen belt. The energies range from tens of keV to hundreds of MeV with intensities up to 10^5 protons/(cm^2 -sec) for energies greater than 30 MeV. The location of the peak flux intensities varies with particle energy. In the equatorial plane, the high energy protons (> 30 MeV) extend only to about 3.5 Earth radii. Using the AP-8-MAX model, **Figure 5.1.3.1** shows the particles fluxes for several proton energies as a function of L along the geomagnetic equator ($B/B_0=1$). Note that, due to the trapping dynamics, the peak fluxes shift to higher L values as the energy decreases. Therefore, even though there is a sharp cutoff of high energy protons at $L > 2.4$, the "slot" region is filled with lower energy protons and is not devoid of particles as is often portrayed in illustrations. **Figure 5.1.3.2** shows fluxes for $E > 30$ MeV as a function of B/B_0 for several L values. Increasing B/B_0 represents moving from the magnetic equator down the field line to the mirror point. Notice the sharp cutoff at low L values where particles are close to their mirror points.

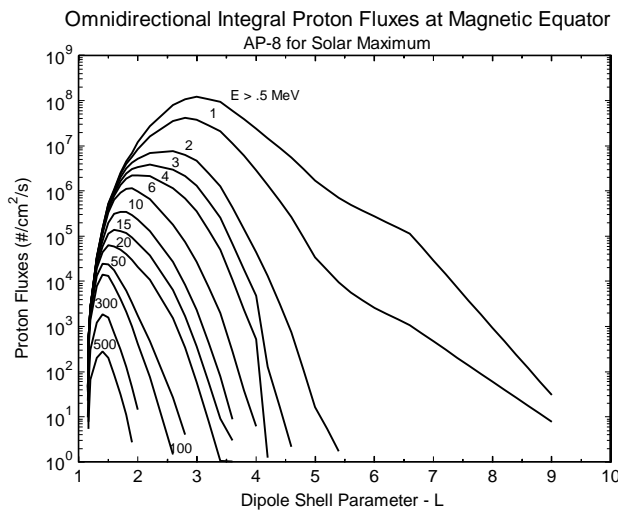


Figure 5.1.3.1: Variation of proton flux levels with radial distance.

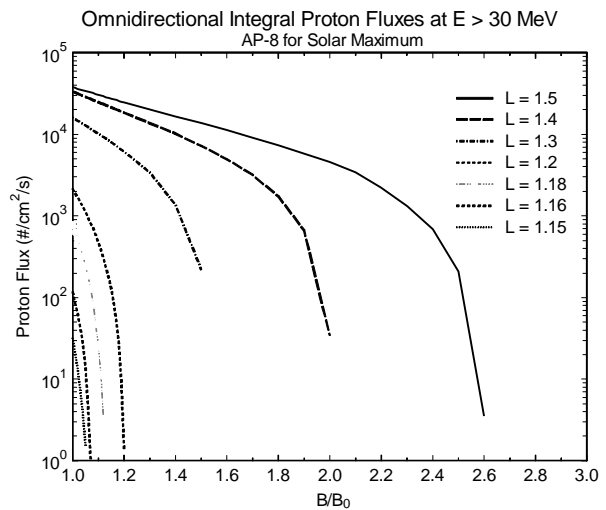


Figure 5.1.3.2: Sharp cutoff at low L values in the AP-8 model. *after Daly et al.*

To get a perspective on how the proton fluxes vary with altitude, **Figures 5.1.3.3** through **5.1.3.5** show proton flux contours for $E > 30$ MeV on world maps for increasing altitudes. At the

500 km altitude cross-section, the SAA is seen clearly as an oval shape, at 1000 km, the size of the oval increases, and at higher altitudes, the fluxes contours show the Van Allen “belt” structure of the trapped particles in these regions.

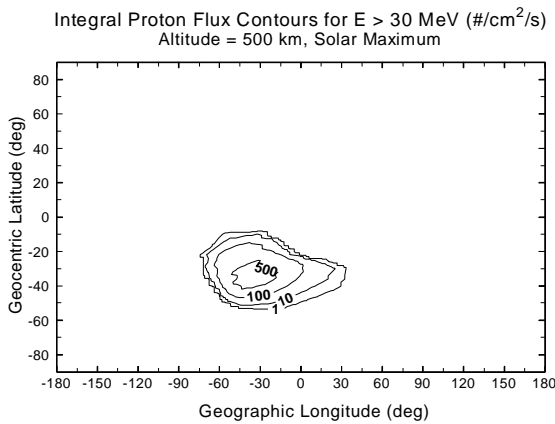


Figure 5.1.3.3: Proton flux contours at 500 km.

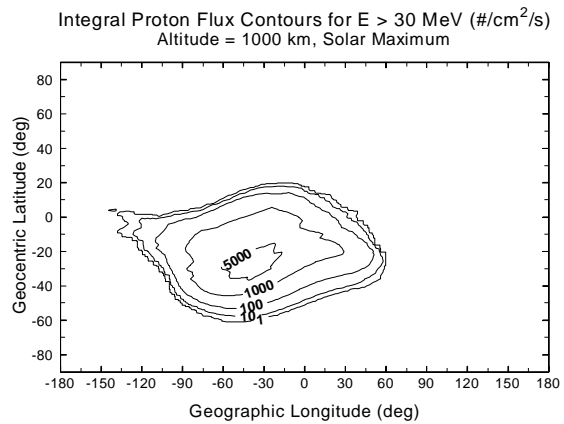


Figure 5.1.3.4: Proton flux contours at 1000 km show the increased SAA region at higher altitudes.

It is easy to see from the maps that the fluxes encountered by a spacecraft will vary depending on the altitude and inclination of the orbit. **Figure 5.1.3.6** plots surface incident proton fluxes versus energy obtained when calculating fluence levels with the AP-8-MAX model for a low earth orbit (LEO) at 29° inclination and 600 km perigee and apogee, a middle earth orbit (MEO) at 51° and 10,000 km perigee and apogee, a geostationary orbit (GEO) at 0° inclination and 36,000 km perigee and apogee, a geostationary transfer orbit (GTO) at 18° inclination and 360 km perigee and 36,000 km apogee, and the orbit for the Earth Observatory Satellite (EOS) at 98° inclination

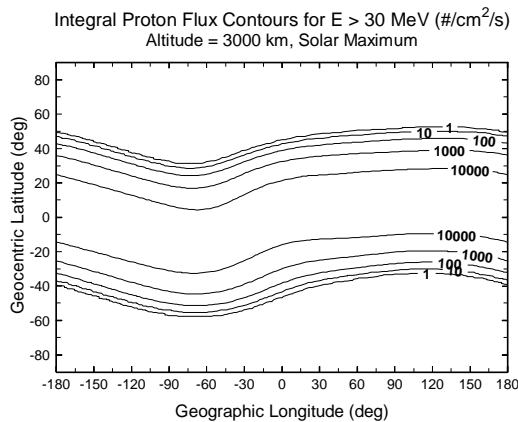


Figure 5.1.3.5: Proton flux contours at 3000 km altitude showing the “belt” structure at higher altitudes.

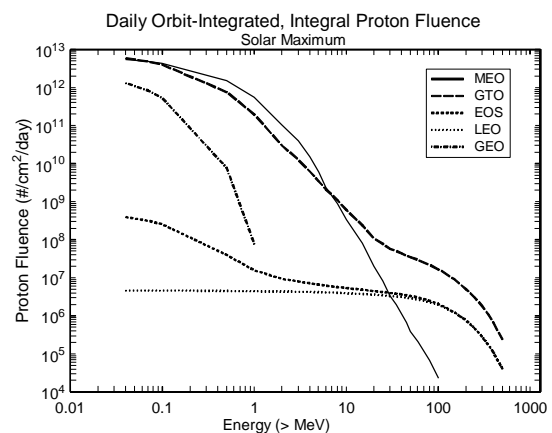


Figure 5.1.3.6: Proton fluence levels have large orbit-dependent variations. Note that, for the GEO orbit, the protons cut off at low energies.

and 705 km perigee and apogee. The figure shows that the variations in fluence level due to spacecraft orbit reach orders of magnitude. In general, the greatest inclination dependencies occur in the range of $0^\circ < i < 30^\circ$. For inclinations over 30° , the fluxes rise more gradually until

about 60°. Over 60°, increasing inclination has little effect on the proton flux levels. The largest altitude variations occur between 200 to 600 km where large increases in flux levels are seen as altitude rises. For altitudes over 600 km, the flux increase with increasing altitude is more gradual. As with the L parameter, the altitude where the peak proton fluxes occurs varies with particle energy. This implies that the location of peak of a device response to the environment will depend on the type of effect and on the sensitivity of the device.

To be a hazard to most spacecraft electronics, particles must penetrate through the spacecraft structure to reach the sensitive component. Protons in the trapped environment are extremely penetrating because of their high energy. **Figure 5.1.3.7** gives the spectra of protons emerging from behind various thicknesses of aluminum for the EOS orbit. Notice that, although there is considerable attenuation of the protons in the low energy ranges, the high energy protons are hardly affected by even the heaviest shield.

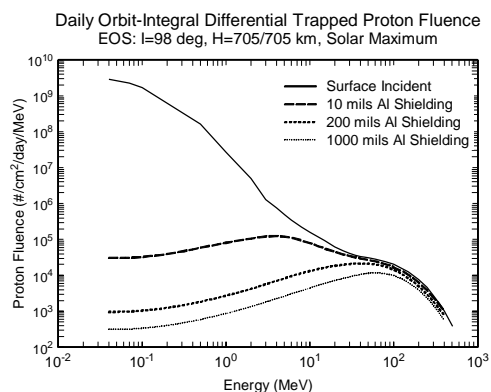


Figure 5.1.3.7: Surface incident protons and those emerging behind aluminum shields. Note the penetration at high energies.

The rate of energy deposition in a sensitive region of a device per unit path length, i.e., the particle’s linear energy transfer (LET), is a measure of the particle’s ability to induce single event effects in devices (see Section III of the Short Course). **Figure 5.1.3.8** shows the LET for protons in the EOS orbit. Note that the LET of the trapped protons is very low, <1 (MeV-cm²)/mg. For most devices, the LET of trapped protons is not sufficient to cause single event effects. It is the secondary spallation and fractionation particles produced by protons which have LETs high enough to cause SEEs. Therefore, instead of proton LET, it is necessary to evaluate the ability of the primary proton to produce the secondary particles. This is determined by the energy of the proton, therefore, energy-flux spectra are used to define the proton single event upset hazard. There are some devices that do upset by direct ionization by the primary protons (e.g. the 1773 fiber optic data bus [50]). In these cases, the upset rates will be very high because the intensity of the primary proton spectrum is orders of magnitude higher than the spectra of the secondary particles.

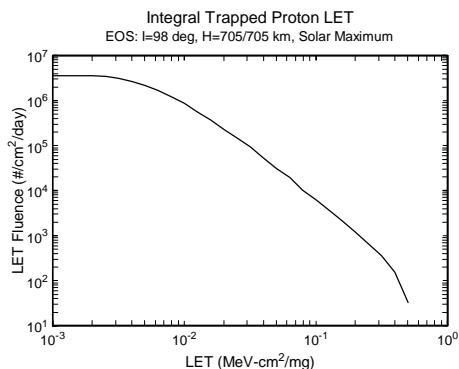


Figure 5.1.3.8: Proton LET values are insufficient to cause single event events in devices with high LET thresholds.

The difference between solar minimum and solar maximum fluxes depends on the energy of the particle and the location in the magnetosphere. Analyses of data from the DMSP satellite showed that the proton fluxes change at a rate of about 6% per year in response to the cyclic variation of solar activity.[42] The AP-8-MIN and AP-8-MAX model the average levels over the solar cycle phase. **Figure 5.1.3.9** plots the orbit averaged energy spectra for average solar minimum and maximum conditions as predicted by the models for a low earth orbit. The difference is about a factor of 2. The variations due to geomagnetic field changes, magnetic storms and substorms, etc. are not reflected in the models and will be discussed in more detail in Section 5.1.5.

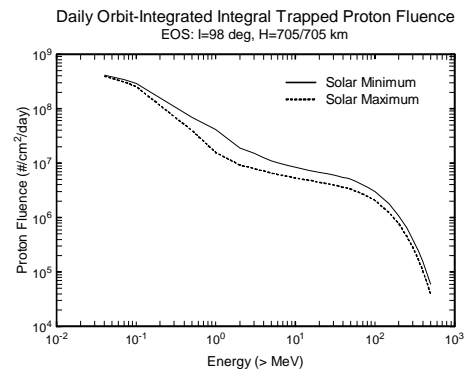


Figure 5.1.3.9: Proton fluences are higher during solar minimum.

5.1.4 Trapped Electron Distribution

Under normal conditions of the magnetosphere, the electron distribution can be separated into two zones, the inner ($1.0 < L < 2.8$) and outer ($2.8 < L < 12.0$). The energies modeled in the inner zone are 0.04 to approximately 4.5 MeV. The modeled outer zone energy spectra extend to energies up to 7 MeV. The intensities reach about 10^7 electrons/($\text{cm}^2\text{-sec}$) for energies greater than 0.5 MeV. Using the AE-8-MAX model, **Figure 5.1.4.1** gives the electron fluxes for several energies as a function of L along the geomagnetic equator. Notice the double peaks which distinguish the inner and outer zones. As with the protons, the location of the peak flux varies with energy. Also, although the slot region has reduced numbers of electrons, it is not devoid of particles. **Figure 5.1.4.2** shows the fluxes for $E > 0.5$ MeV as a function of B/B_0 for several L values. As with the protons, the fluxes cut off sharply at low L values.

Figures 5.1.4.3 through **5.1.4.5** are electron flux isocontours for $E > 0.5$ MeV on world maps for increasing altitudes. Like the protons, the low altitudes show the SAA and, as the altitude increases, the belt structure of the trapped electrons becomes apparent. The electrons in the high latitude regions in Figure 5.1.4.3 and 5.1.4.4 are the high latitude protrusions of the outer belt or the “horns”. **Figure 5.1.4.6** plots electron energy spectra for LEO, MEO, GTO, GEO, and the EOS orbit. Notice that, for higher altitudes, the spectra become more energetic and increase in intensity due to increasing exposure to the more intense outer zone electrons. The altitude and inclination dependencies are similar to those of the protons but, as seen in the GEO spectra, the electrons extend out to higher altitudes. As with the L parameter, the altitude where the peak fluxes occur varies with energy.

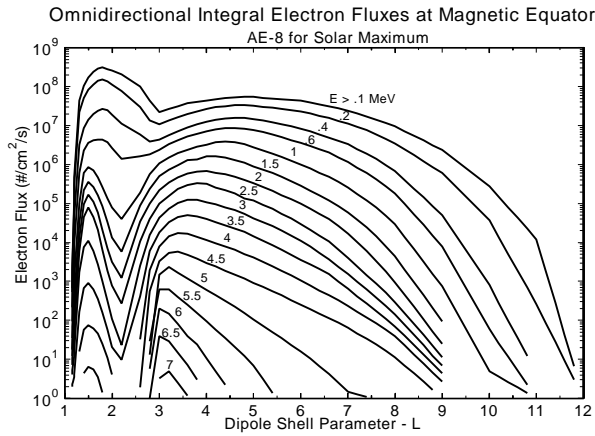


Figure 5.1.4.1: Variation of electron flux levels with radial distance. Note the double peak showing the inner and outer zones

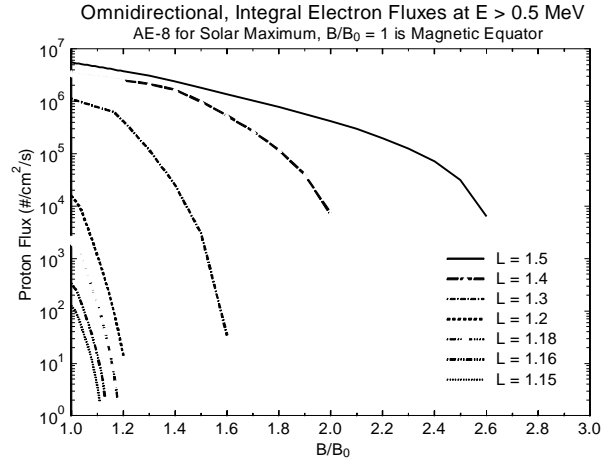


Figure 5.1.4.2: Sharp cutoff at low L values in the AE-8 model. *after Daly et al.*

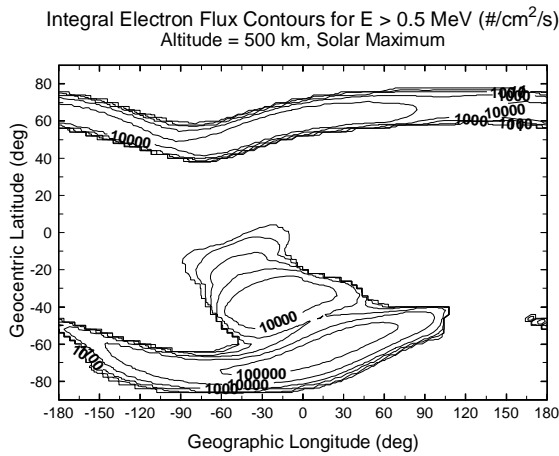


Figure 5.1.4.3: Electron fluxes at 500 km altitude showing the SAA. The bands at the top and bottom of the plot are the high latitude “horns” of the outer zone.

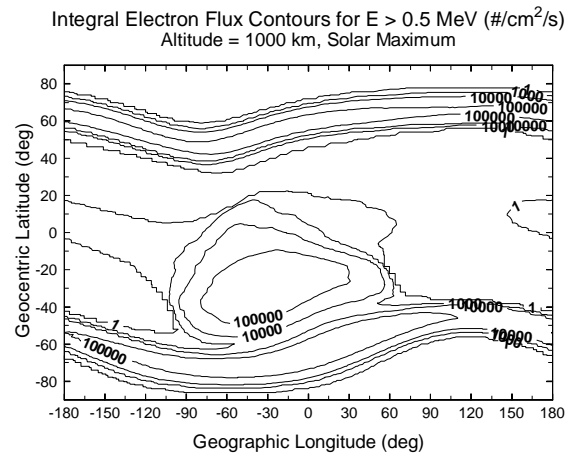


Figure 5.1.4.4: At 1000 km, the SAA begins to spread out, covering a larger region.

Electrons are not as penetrating as protons because they are lighter and less energetic.

Figure 5.1.4.7 plots the energy spectra for electrons emerging behind various aluminum shield thicknesses for the GEO case. Unlike the protons, the shielding is much more effective at attenuating electrons.

An important factor to consider is that secondary photon radiation, called braking or bremsstrahlung radiation, is produced when electrons are slowed down by the orbital electrons of the shielding material (see **Figure 5.1.4.8**). Because photons are so penetrating, they are very difficult to attenuate once they are produced. The dose deposited by the photons is usually 1 to 2 orders of magnitude lower than the dose due to the primary particles. However, in orbits exposed to high levels of electrons (e.g., GEO and GTO), photon background may interfere with instrument performance, especially if there are large amounts of high atomic weight material

around the sensitive location. In these cases, it may be necessary to resort to layered shielding to avoid photon production.[51,52] For further discussion of shielding issues, see Section II of this Short Course. Finally, electrons have very low LET relative to protons and heavier ions and are not known to induce SEEs.

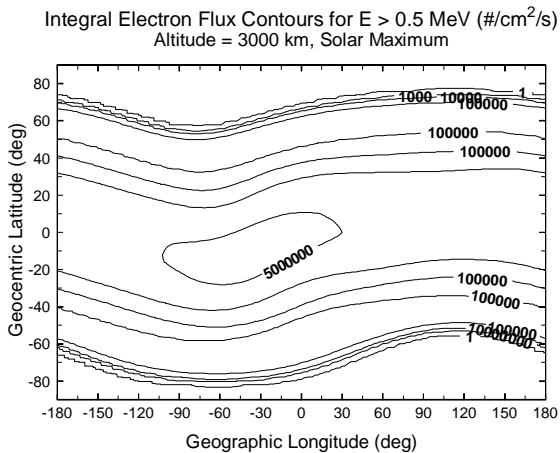


Figure 5.1.4.5: Electron fluxes at 3000 km showing the “belt” structure at higher altitudes.

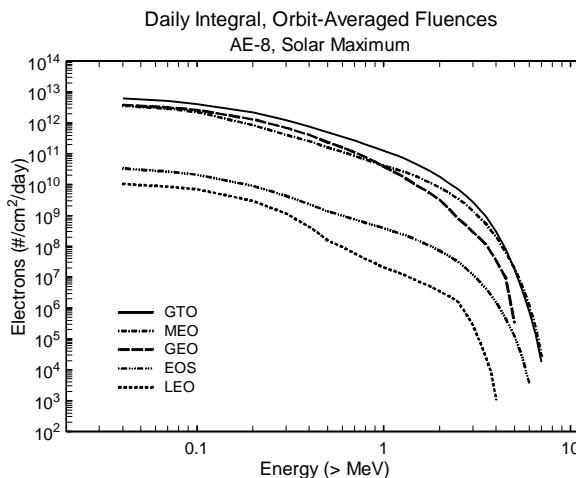


Figure 5.1.4.6: High altitude orbits (GEO, GTO, MEO) spend large amounts of time in the intense outer zone resulting in higher daily fluences.

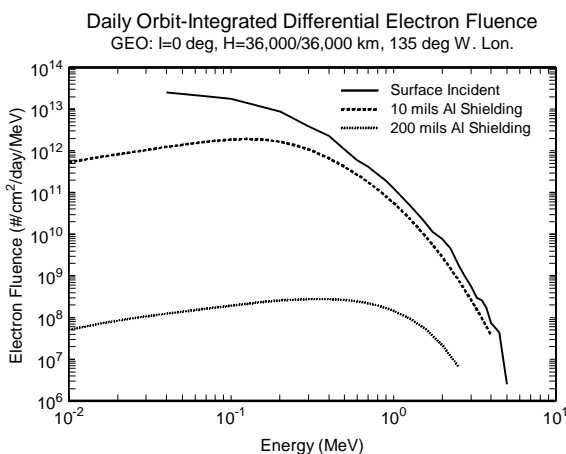


Figure 5.1.4.7: Unlike protons, shielding is effective in attenuating electrons.

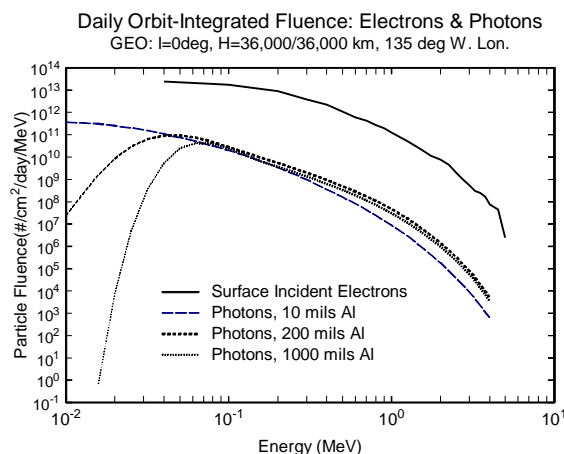


Figure 5.1.4.8: As electrons are slowed down by materials, a secondary bremsstrahlung radiation consisting of photons is produced.

As with the protons, the inner zone electrons are a fairly stable population. They show modulation due to the solar cycle as described in Section 5.1.1. **Figure 5.1.4.9** shows a comparison of the solar minimum and solar maximum electron fluences for a low earth orbit as predicted by the AE-8 model. As with the protons, the difference is approximately a factor of two.

In contrast, the outer zone flux levels are dynamic to the degree that any variations due to solar cycle are masked by other dynamics. This is reflected in the AE-8 models which at high altitude orbit (e.g., geostationary) predict the same flux levels of electrons for solar minimum and maximum.

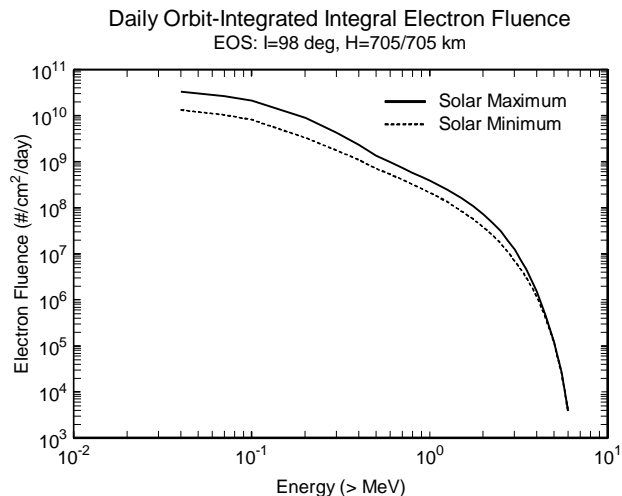


Figure 5.1.4.9: Inner zone electron levels are higher during solar maximum.

5.1.5 Problems with the AE-8 and AP-8 Models

The previous section which described the distribution of the trapped protons and electrons using the NASA models referred to some of the shortcomings of these models. Several authors [38,53,54] have provided excellent observations concerning the accuracy of the AE-8 and AP-8 models.

As stated in Section 5.1.2, the spacecraft data used to construct the AP-8 and AE-8 models were normalized to 1960 or 1970 dates with two field models. However, we know that the magnetic field changes shift the location of the SAA (see Section 5.1.1). When calculating orbit integrated fluences, any errors produced by the SAA shift are averaged out. However, for applications requiring knowledge of the location of SAA fluxes, such as, instrument operation or flight data analyses, the SAA shift can be important. When evaluating data from the CREAM instrument on the STS-43, Dyer *et al.* [55] discovered that there were some cases when the instrument detected particles but the spacecraft was out of the SAA. They found that it was possible to place the spacecraft in the SAA if the models were accessed with B/B_0 and L coordinates for the actual time of the mission. However, Daly *et al.* [53] and Konradi *et al.* [56] have found that this method generates incorrect flux levels. At low altitudes, the fluxes calculated with updated field epochs can be orders of magnitude too high and, at higher altitudes, the method produces fluxes that are too low. To minimize the error, Daly *et al.* [53] demonstrated that it is necessary to calculate fluxes from the models with the field values used to normalize the data (see Section 5.1.2), and if the absolute position of the flux is important for one's application,

it is necessary to perform a latitude and longitude transformation reflecting the shift of the magnetic field to place the fluxes in the correct latitude and longitude positions.

As discussed in Section 5.1.1, the protons at 300 to 500 km are highly anisotropic. This lack of east-west symmetry is not reflected in the AE-8 models. For Space Station orbits, Watts *et al.* [57] have developed a model that corrects this problem.

Daly *et al.* [53] have pointed out some errors in the models and documentation, including a source code error in AP-8-MIN and the fact that the AZUR dataset on which the AP-8-MAX is based covered a time span of 3 months, not 6 months. They also note that the Space Shuttle and the LDEF satellite measured environments in low altitudes (300 to 500 km) from 60 to 100% higher than those predicted by the AP-8 models. Daly *et al.* [53] determined that a large source of this error is due to the method used to interpolate between the B/B_0 values in the regions near the atmospheric cutoff. (See Figures 5.1.3.2 and 5.1.4.2). They have developed an alternate interpolation method that increases the fluxes by 10 to 40% bringing them closer to the measured levels. They also recommend that an additional L increment at the low L values be included in the models to give better resolution at the steep gradients. This increases the fluxes by about 40%. When these two refinements to the interpolation scheme are combined, the revised flux levels are much closer to the measured values. The increased capacity of modern computers make these improvements feasible.

The need for work on trapped proton models has been addressed by the European Space Agency's TREND program. A progress report [58] on the program points out that the AZUR dataset used to implement the solar cycle dependence in the AP-8 model for solar minimum (resulting in the AP-8-MAX model) has not been fully analyzed and should be reexamined. One problem with the AZUR dataset is that it does not contain data for low energy protons at low altitudes. Extrapolations led to inaccurate predictions for low energy protons in the low altitude regions as evidenced by the flat low energy curve for the "LEO" orbit spectrum in Figure 5.1.3.6.

Recent measurements from LEO microsattellites (UoSAT-3, KITSAT-1, PoSAT-1) suggest that the long term dynamics of the trapped proton environment are out of phase with the solar cycle.[59] It has been recommended that the trapped proton cycle could be better modeled on the basis of other parameters (see Section 5.1.6).

The biggest problem with the models is that they do not reflect the dynamic nature of the environment. Section 3.2 presented the process by which particles are injected into the magnetosphere as a result of magnetic storms, and Section 5.1.1 described the spacecraft measurements of storm effects. These particle injections cause several changes in the trapped particle environment that are not included in the models. The storm belts are not represented in the NASA models. Also, the inner zone electrons are modeled up to approximately 5 MeV and the outer zone up to about 7 MeV but the CRRES satellite measured electrons up to 30 MeV. The CRRES satellite showed that the environment is extremely dynamic and that electronic parts respond to the changes. Gussenhoven *et al.* review the findings of CRRES in Reference 38.

For some applications, the AP-8 and AE-8 models do not provide adequate information to assess the level of hazard posed by the radiation environment. For electron induced electrostatic charging and discharging evaluations, long term averages provided by the AE-8 models do not give sufficient information about the environment because worst case conditions cannot be evaluated accurately. Because of instrument interference or the possibility of system malfunctions caused by proton induced single event effects, mission operations are usually planned outside of the SAA. Encountering protons outside of the SAA in the storm belts could jeopardize those operations. Analysis of data from the CRRES dosimeter indicate that doses are increased significantly for some orbits as a result the high energy electrons in the electron storm belt.

Even when taking the electron injections into account, the NASA electron models still predict fluxes that are higher than measured in the high L regions. Several experimenters have shown that the AE-8 model overestimates electron flux levels in the high L regions, including Gussenhoven *et al.* [38] and Dyer *et al.* [60] By comparing data from six satellites, experimenters recently found evidence that the overprediction may be the result of the contamination of the instrument data used to construct that portion of the model by Starfish electrons [61] (see Section 6.0).

5.1.6 Dynamic Models - A Beginning

For most radiation belt source mechanisms (Section 5.1.1), accurate information is lacking. To create dynamic models of the Earth's radiation belts, it is necessary to know the source strength for different particle species as a function of their energy and pitch angle, the effective source location within and on the boundaries of the trapping regions, and the source strength as a function of the different geophysical conditions during both quiet and disturbed times. Unfortunately, that information is lacking, especially for recent solar cycles. Generally, it is valid to assume that, for quiet conditions, the source is capable of supplying particles to the outer radiation zone at a rate sufficient to offset particle losses within the trapping regions. However, this assumption is not valid for storms and other magnetic disturbances. As a result, most of the radiation modeling, including the NASA AP-8 and AE-8 models, has been done for quiet, steady state conditions.

Several researchers have recognized the need for trapped particle models that represent storm and substorm conditions. Pfitzer [62] plots predicted flux values for low inclination orbits as a function of the average atmospheric density. From this index, he can interpolate and extrapolate fluxes for solar activity conditions from the AP-8 and AE-8 models. Huston *et al.* [63] have continued this effort under NASA's Space Environment and Effects program. They are analyzing environment data for the TIROS/NOAA satellite with the goal of including proton variations due to solar activity indices. Their goal is to produce a low altitude proton model (<1000 km) based on coordinates more applicable to this region in space and one that is a more accurate representation of the effect of solar cycle modulation.

Heynderickx and Lamaire⁶⁴ have also plotted model fluxes as a function of the average weighted density of the atmosphere (n_s) that is encountered by a particle on its drift shell. They found that the relationship between n_s and the AP-8 and AE-8 models fluxes is well ordered, especially at low L values. If a practical form for the n_s calculation is developed, this method could lead to replacing B_0 with $B_0(n_s)$ when accessing the models, thereby reflecting solar activity effects.

The CRRES team developed three empirical models designed to model short term dynamic changes in the particle population, the CRRESPRO [65], CRRESELE [66], and CRRESRAD 67. While the models are based on data collected over a short 14 month period and during solar maximum conditions only, they give the most comprehensive picture available of the environment resulting from a geomagnetic storm. The models include a warning that the spatial coverage is limited to regions of the magnetosphere covered by the 14-month CRRES mission.

The CRRESPRO model maps trapped protons for L values of 1.15 to 5.5 based on analysis of the CRRES proton telescope data.[68] This model calculates orbit averaged protons fluences for a quiet or an active environment. The active environment models the second proton belt formed in the region of $2 < L < 3$ when solar protons penetrated down to 3 earth radii. **Figure 5.1.6.1** compares environments for the quiet and active CRRESPRO with the AP-8-MAX model. Note that the CRRESPRO active model reflects the second belt and that the AP-8-MAX falls between the high and the low values at $L > 1.8$. Also, at $L < 1.7$ the figure shows that the AP-8 underpredicts at low altitudes as measured by the Shuttle and LDEF (see Section 5.1.5). **Figure 5.1.6.2** compares predictions using the AP-8-MAX model and the quiet and active CRRESPRO models for the MEO orbit. One shortcoming of this model is that it only provides orbit integrated values and does not give the user the ability to calculate fluxes for each position of an orbit. The ability to know where protons are encountered during an orbit is very important for single event effects analyses or instrument operations which require avoiding high level of fluxes.

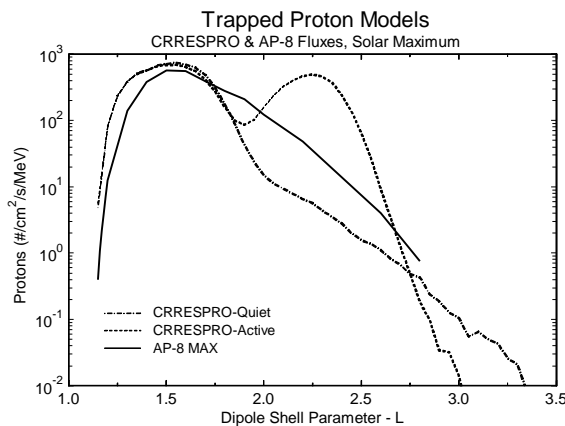


Figure 5.1.6.1: Comparison of AP-8 and CRRESPRO quiet and active models. *Gussenhoven et al.*

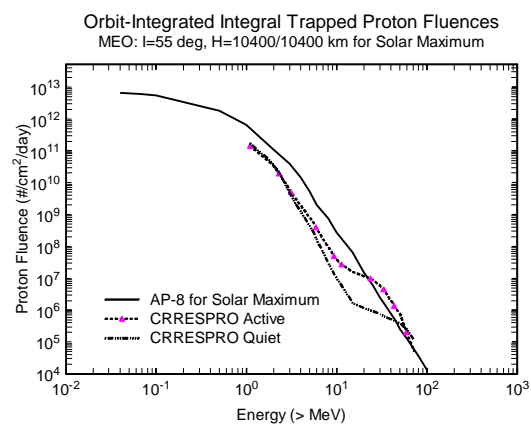


Figure 5.1.6.2: Proton fluences for the MEO case calculated with the CRRESPRO and AP-8 models.

Bratigam *et al.* [69] developed a model with 8 submodels which give the radial flux variation for different states of magnetospheric activity. The CRRESELE is a code based on this work that maps trapped electrons for L values of 2.5 to 6.5. It gives the user electron levels for six ranges of magnetic activity, the average for the CRRES mission, and the worst case encountered during the mission. The CRRESELE models the third electron belt. The model also predicts the 27-day recurring, intense outer zone electron “episodes” which provides an improvement over the average values provided by AE-8. Calculations from the CRRESELE model agree with the measurements of the DMSP satellite. **Figure 5.1.6.3** compares the CRRESELE worst case, average, and the AE-8 models for two energy levels (for high altitudes, AE-8 solar minimum and maximum versions predict the same levels). The left plot for .95 MeV energy shows that the fluxes predicted by the AE-8 and measured by CRRES peak at different L values. The plot on the right shows that the AE-8 model does overpredict electron fluxes at higher L energies and higher L values.

Vampola [70], under the sponsorship of ESA’s TREND program, has used data from CRRES’s MEA instrument to extend the

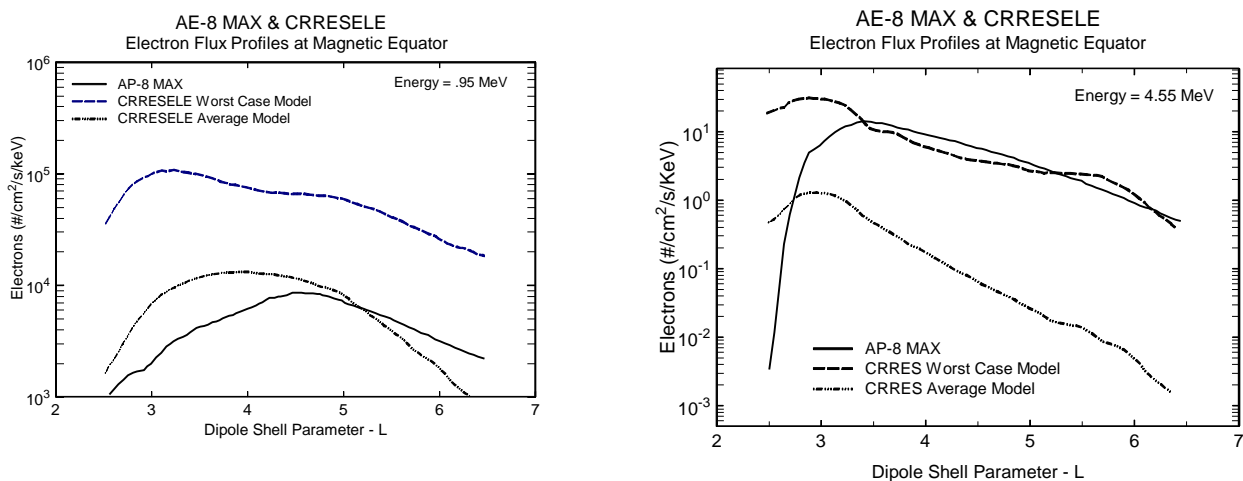


Figure 5.1.6.3: Comparison of the AE-8 model and CRRES electron measurements show that the AE-8 model overpredicts at higher energies for high altitudes. *Gussenhoven et al.*

CRRES solar maximum electron measurements to predict electron levels for solar minimum. Magnetic indices for a sixty year period were used to train a neural net for projection of activity into the present solar minimum period. The neural net was used to predict fluxes for the CRRES mission (solar maximum) and good agreement was found between the predictions and measurements. The result of this effort is the SEE1 model of electrons for solar minimum. **Figure 5.1.6.4** compares AE-8 flux levels to the average CRRESELE model and the ESA SEE1 model for a 0° inclination and 30,000 km altitude orbit showing that the AE-8 flux levels are higher. Because the fluxes at energies greater than 4 MeV in the ESA SEE1 model are extrapolated, the author warns that the flux levels at higher energies are likely to be excessive.

The CRRESRAD model maps the dosimeter data from CRRES.[71] Dose values are given for low LET and high LET detectors and for both low and high LET detectors for the 4 dome thicknesses on the instrument. This model is useful for defining the range of dose between quiet and storm environments. Its major drawback is its limited spatial range. It is not valid for orbits with apogee less than 800 km. Data from the US Air Force dosimeter on board the APEX

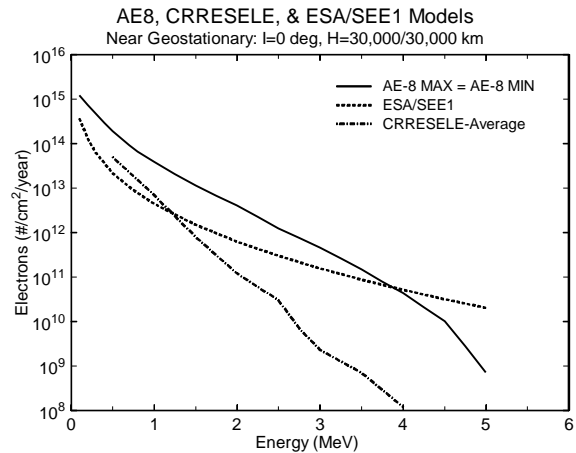


Figure 5.1.6.4: Comparison of the three electron models for a high altitude orbit.

satellite are being used to improve the low altitude predictions of the CRRESRAD

model.[72] **Figure 5.1.6.5** shows the difference in predicted dose for one year missions for a satellite in a GTO for the CRRESRAD quiet, active, and average models.

One the most important conclusions that resulted from the CRRES program is that existing theory cannot explain particle penetrations deep into the magnetosphere. Hudson *et al.* [73] have attempted to model the rapid creation of high energy radiation belts by the March 1991 event with some success. Unfortunately, the frequency of occurrence of this atypical event is unknown, therefore, applying the model to setting rad-hard requirements creates uncertainties that are impossible to quantify.

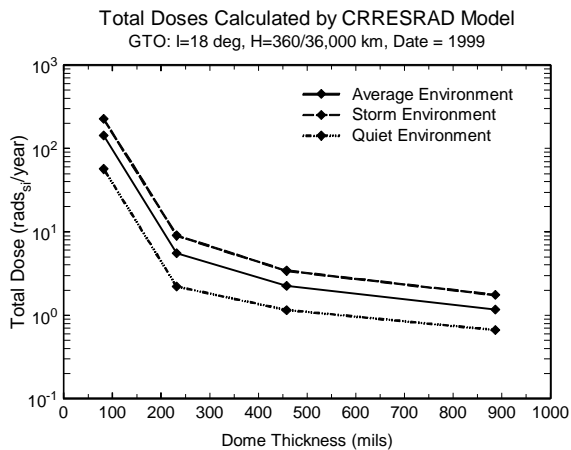


Figure 5.1.6.5: Total doses for missions encountering storm belts are significantly higher than the doses accumulated during quiet times.

Boucher *et al.* [74] provide a review of modeling techniques that show promise of providing computer generated models of trapped particle transport during storms. The first phase is the growth phase, that is, the effect that the stretching of the magnetic field lines has on particle distribution along the field line (see Section 3.2 and Figure 3.2.1). Thus far, this phase has only been modeled using full trajectory codes.

The second phase begins with disruption of the field line and a “dipolarization” [75] that results in particles being injected in the Earth’s direction and possibly a plasmoid being propagated tailward. The injected particles are transported inward and are energized giving rise to the ring current population. The codes most successful at simulating this process are the center guiding codes or 3-D diffusion codes, enabling us to understand the displacement of old and new

populations. Boucher *et al.* [76] applied such a code to study the dynamics of the trapped electron population near geostationary regions. They simulated the ejection of low energy electrons at $L \sim 7$ and calculated their diffusion over one month.

Finally, Bourdairé *et al.* [77] have begun development on a 4-D diffusion code to calculate the transport of particles throughout the internal magnetosphere. They plan to apply the code to several problems, including calculation of the transport of existing and injected particles during storms, determination of the ring current growth using calculations for both protons and electrons, and discovery of the process by which high energy particles are totally removed from the internal magnetosphere. Initial application of their code is promising. A typical problem addressed by the code is to transport particles injected near midnight while the electric field increases instantaneously by a factor of 10.

Despite these promising developments, we have yet to model or even understand the processes involved in producing the effects of events like the March 1991 storm. Dynamic modeling of the trapped particle population is greatly hampered by lack of measurements to verify modeling techniques.

5.2 Trapped Heavy Ions - Earth

In addition to protons and electrons, heavier ions are trapped in the magnetosphere. Blake and Friesen [78] reported on the results of a heavy ion experiment on board the OV1-19 experiment which measured He ions in the energy range of 0.85 to 9.0 MeV. They were able to show that these particles are a result of radial diffusion and that the distribution is strongly dependent on L . Using data from the COSMOS spacecraft, Grigorov *et al.* [79] first reported in 1991 that the heavy ions in the magnetosphere are anomalous cosmic rays (ACRs) that become trapped. The energy spectra of galactic He, C, N, O, Ne, Ar, and H ions below energies of 50 MeV/nucleon have shown anomalous increases above quiet time galactic cosmic ray levels during solar minimum. The ACRs are thought to be neutral interstellar particles that drift into the heliosphere, become ionized by the solar wind or UV radiation and are accelerated to energies up to 10s of MeV/nucleon. They are singly ionized and sensitive to solar modulation. As they penetrate deeply into the Earth's magnetosphere, their remaining electrons are stripped in the upper atmosphere. The resulting magnetic rigidity is below the trapping limit so they become trapped. In 1993 the SAMPEX spacecraft, with its Mass Spectrometer Telescope (MAST), was launched into a low Earth orbit. The MAST measurements of heavy ions with $Z \geq 2$ have confirmed that the trapped He, N, O, and Ne are trapped from the anomalous cosmic rays (ACRs). [80] The origin of the trapped He flux is still uncertain.

Figure 5.2.1 shows the distribution of the particle counts on a world map grid and **Figure 5.2.2** shows the location of the trapped heavy ions in the Van Allen belts. Tylka's Monte Carlo models show excellent agreement.[81] N, Ne, and O have similar L distributions and peak near $L = 2$. Helium peaks at $L = 1.8$ and has a smaller peak at $L = 1.2$. Variations of the trapped heavy ions correlate with variations in the interplanetary ACR, therefore, the levels are expected to peak during solar minimum. Because of their low energies, hence, their inability to penetrate spacecraft shielding, trapped heavy ions do not constitute a significant hazard to spacecraft in terms of single

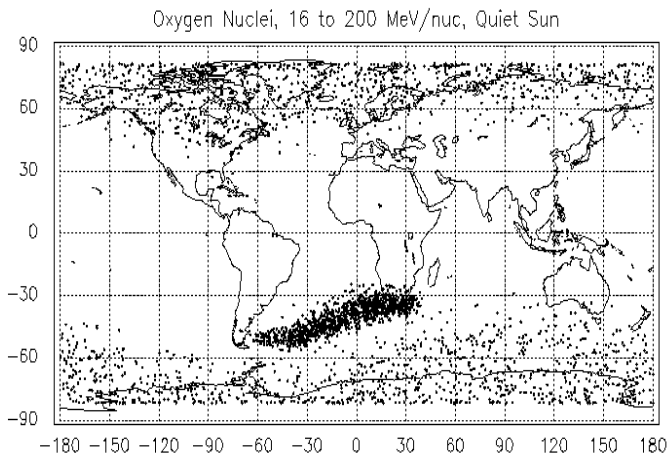


Figure 5.2.1: The location of trapped oxygen ions.
NASA/GSFC SAMPEX

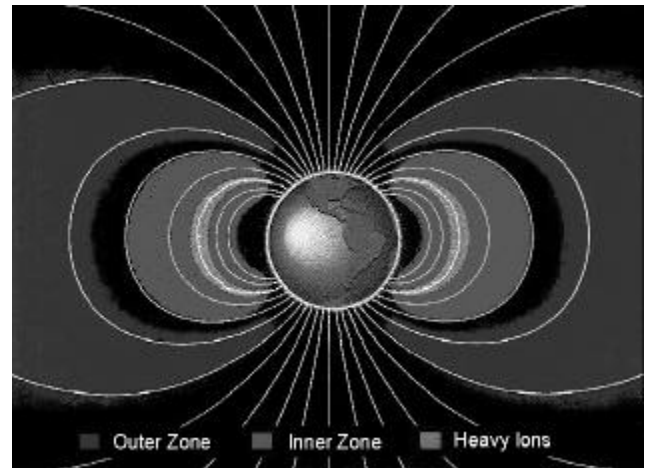


Figure 5.2.2: A cross-section of the Van Allen belts showing the location of the trapped heavy ions.
NASA/GSFC SAMPEX

event effects. However, because heavy ions have high quality factors in tissue, they could be a hazard for astronauts in terms of dose levels.

5.3 Trapped Particles - Other Planets

The minimum requirement for the existence of a planetary radiation belt is that the planet's dipole magnetic moment must be sufficiently great such that the flow of the solar wind is arrested before the particles reach the top of the planet's atmosphere where the particle will lose its energy due to collisions. Jupiter, Saturn, and Uranus are known to have energetic radiation environments that researchers believe are similar to the Earth's trapped radiation belts. The Phobos probe showed that Mars also has a radiation environment. Measurements indicate that the intensities of the radiation environment of Mars, Saturn, and Uranus are much lower than the Earth's and do not pose a threat to electronics. Jupiter's environment is considerably more intense than the Earth's and is more extensive, therefore, mission planning for spacecraft that will spend time in trapping regions of Jupiter must include careful definitions of the radiation environment. For example, electrons with energies > 100 MeV must be modeled for accurate dose calculations, and volcanic activity on Io injects oxygen and sulfur ions that pose significant single event effects hazards.

5.4 Galactic Cosmic Ray Heavy Ions

The flux levels of the Galactic cosmic rays (GCRs) are low compared to the trapped particles, but they are hazardous to spacecraft electronics because their high energies make them extremely penetrating. Also, they have a high rate of energy deposition as measured by their LET rate. A particle's LET is primarily dependent on the density of the target material and, to a lesser degree, the density and thickness of the shielding material. It is their high LET that makes cosmic rays an important contributor to single event effects problems for spacecraft, especially in orbits where the magnetosphere offers little protection.

The total dose deposition in silicon is only 10 rads/year when the GCR environment is at its peak. [17] However, when the GCR dose is converted to dose equivalent in units of rem for biological systems, it can reach dangerous levels for humans. This can be true even for low earth orbits where the effect of the magnetospheric attenuation on the fluence levels of cosmic ray particles is significant.

5.4.1 Origin of Galactic Cosmic Ray Heavy Ions

In the early 1900s, scientists found that instruments used for studying x-rays and radioactivity measured a background source of unidentified radiation. Victor Hess, an Austrian physicist, measured gamma rays by designing ionization chambers and flying them on balloons. With his balloon experiments, he discovered an extremely penetrating radiation that increased in density as altitude increased. From his experiments, he concluded that this radiation was from an extraterrestrial source. Later, Jacob Clay was able to show that cosmic rays were the source of the on-ground radiation and that measured by Hess higher in the atmosphere. In 1936, Hess received the Noble Prize for the discovery of galactic cosmic rays. Although we now know that these "rays" are really particles, they are still referred to as cosmic rays.

The GCRs originate outside of the solar system. Although there are plausible models of how they are produced, their origin is still a matter of debate.[82] Scientists believe that they propagate through all space that is unoccupied by dense matter. They are essentially isotropic outside of regions of space that are dominated by particles and fields of the sun. Galactic radiation consists of ions of all elements of the periodic table and are composed of about 83% protons, 13% alphas (^4He ions), 3% electrons, and about 1% heavier nuclei. Unlike the charged particles that originate at the Sun, the GCRs do not have a characteristic energy limit. Their energies range from 10s of MeV/n to 100s of GeV/nuc. Because they must pass through about 7 g/cm^2 of interstellar gas, the GCRs of even the heaviest ions are probably fully ionized. [23]

A second source of galactic particles is the so called "anomalous component". It is composed of helium and heavier ions with energies greater than 50 MeV/nucleon. It is believed that the anomalous component originates in the neutral interstellar gas that diffuses into the heliosphere,

becomes singly ionized by solar radiation or charge exchange, and is then connected by the solar wind to the outer heliosphere. The ions are then accelerated and propagate to Earth. The anomalous component is seen only during solar minimum and the details vary from solar minimum to solar minimum. There is growing evidence that the anomalous component is singly ionized, therefore, the ions have greater ability to penetrate the magnetosphere. As discussed in Section 5.2, the anomalous component is thought to be the source of the trapped heavy ions.

Our knowledge of the abundances of galactic cosmic rays comes from spacecraft and balloon experiments that have been conducted over a forty year period. **Figure 5.4.1.1** from Medwaldt [83] gives the abundances of the heavy ions at an energy of 2 GeV/nuc as a function of particle nuclear charge z . The values are normalized to silicon = 10^6 . Note that the relative flux intensities vary by several orders of magnitude. The relative abundances are roughly proportional to the distribution in solar system material. Significant differences are discussed in Medwaldt [83] who also gives a table of relative abundances.

The galactic particles are always present, however, their intensities rise and fall with the solar cycle variations.

The sun modulates a set of local interstellar spectra at the outer

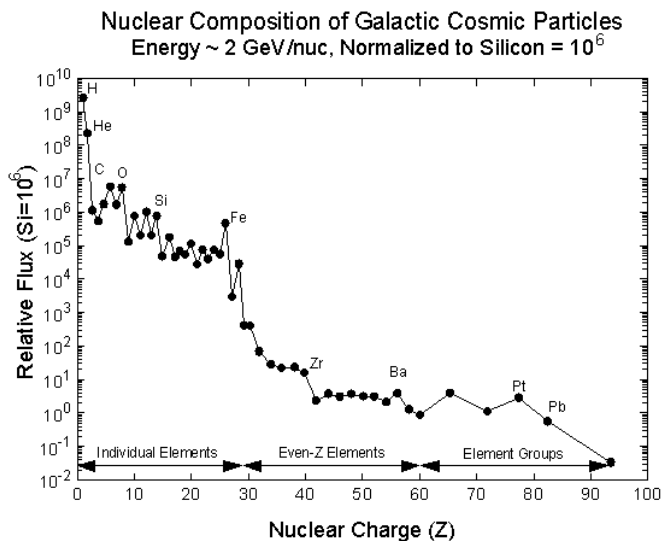


Figure 5.4.1.1: Relative abundances of galactic cosmic ray ions in interplanetary space. *after Medwaldt*

boundary of the heliosphere.[84] The modulation can be defined by a single parameter which is a function of distance from the sun, the speed of the radial solar wind, and a radial transport particle diffusion coefficient. As with the trapped proton population, GCRs are at their peak level during solar minimum and at their lowest level during solar maximum and we now know that the length of the GCR modulation cycle is 22 years and not 11 years as previously thought. The difference between the extremes of the solar minimum and maximum fluence levels is approximately a factor of 2 to 10 depending on the ion energy. **Figure 5.4.1.2** shows the slow, long term cyclic variation of the cosmic ray (C, N, O) fluences for a 20-year period as measured by the IMP-8 spacecraft. The sharp spikes superimposed on the cosmic ray background are caused by solar events.

The interplanetary energy spectra for H, He, and Fe are given in **Figure 5.4.1.3**. [17] The H values are multiplied by five for better resolution on the graph. The measurements were taken for various times throughout the solar cycle as shown by the variation of the spectra below energies of 1 to 3 GeV.

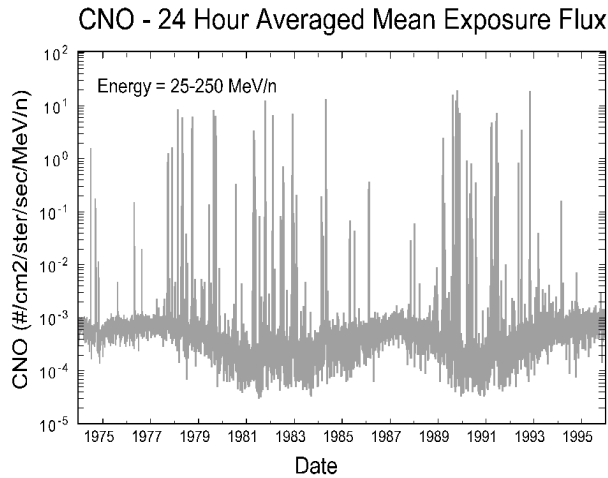


Figure 5.4.1.2: IMP-8 measurements of interplanetary ions from the C-N-O group. Note the solar particle event spikes superimposed on the lower level, slowly varying galactic cosmic rays. *after Nakamura*

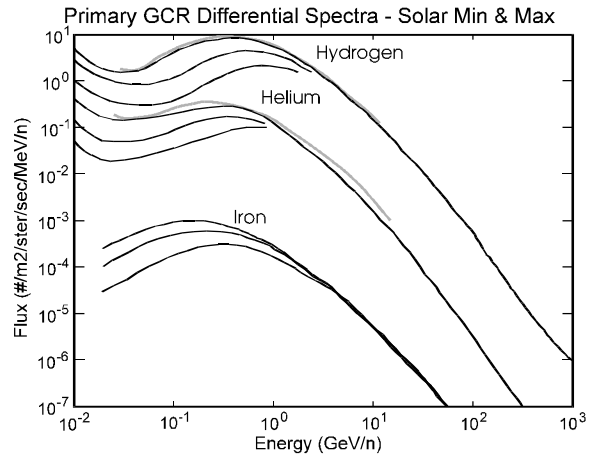


Figure 5.4.1.3: Energy spectra of interplanetary galactic cosmic rays. Hydrogen values are multiplied by 5 to distinguish them from the helium spectra. *after Smart and Shea*

Measurements from Pioneer and Voyager show that the composition of cosmic rays is weakly dependent on the distance from the Sun. The radial gradient from 0.3 to 40 AU is < 10% per AU. For the anomalous component, the gradient increases to 15% per AU. During solar maximum there is 0% gradient out to 30 AU. Latitude gradients have also been studied and found to be 0.5% per degree and 3-6% per degree for the anomalous component.[85]

The galactic cosmic ray population also contains electrons. However, unlike the solar wind (see Section 2), the GCRs do not contain electrons in sufficient number to make the population electrically neutral. The GCR electron density is orders of magnitude lower than the density of the solar wind, therefore, it does not have to be taken into account when evaluating radiation damage levels.

As discussed in Section 4.2, the Earth's magnetic field provides some protection from the galactic particles by deflecting the particles as they impinge upon the magnetosphere. The penetration power of these particles is a function of the particle's energy and ionization state. The exposure of a spacecraft primarily depends on the inclination and, secondarily, the altitude of the trajectory. Cosmic rays have free access over the polar regions where field lines are open to interplanetary space. The exposure of a given orbit is determined by rigidity functions calculated with geomagnetic field models (Section 4.2). The coefficients in the field models include a time variation so that the rigidity functions can be calculated for the date of a mission.

5.4.2 Galactic Cosmic Ray Models

Recognizing the need for a comprehensive software package that integrated environment predictions with single event upset models, Jim Adams and his colleagues developed the CREME code⁸⁶ which was first released in 1984. Recently Tylka *et al.* [87] with the sponsorship of the NASA Space Environments and Effects program released an update to the CREME package, CREME96. CREME96 offers several improvements over the old CREME code. The galactic cosmic ray heavy ion models will be reviewed here, and the solar heavy ion models will be reviewed in Section 5.6.

The GCR heavy ion environment calculated by CREME was based on data from several researchers collected through 1980. (see Adams [23]). Because of the dissimilar shape of their energy spectra, the hydrogen, helium, and iron ion distributions were treated as separate cases, and the other elements were scaled to one of the three spectra, as appropriate, using the relative abundances of the elements.

CREME offered four different models of the GCR environment, specified in the code by the “M” input parameter. In 1992, it was recommended that only two of the four GCR models the old CREME code be used.[88] Because of mounting evidence that the anomalous component is singly ionized, the “M=2” environment option was considered inaccurate because it calculates a fully ionized anomalous component. Also, the “M=3” option or the so called “90% worst case environment” was no longer recommended as a standard environment for device comparisons. This environment calculates GCR spectra for peak solar minimum conditions and adds in particles from medium sized solar events with energies less than 100 MeV/n. The additional fluence levels were determined such that instantaneous fluxes will occur with a 10% probability. (Larger events were modeled in the solar particle models of CREME.) These conditions only occur for very short time periods during a mission. Therefore, Petersen *et al.* [88] recommended that the “M=1” option for the peak of the solar minimum (YEAR = 1975.144) be used to provide fluxes for normal conditions and that the “M=4” option be used to calculate the solar minimum spectrum with the singly ionized component to predict worst case GCR levels. An uncertainty factor of 2 was defined for the models.

These authors also pointed out that the solar cycle modulation function is not correct because it is based on an 11 year modulation cycle and not the correct 22 year cycle. Other models of the GCR environment, including the CHIME model, [84] a model by Badhwar and O'Neill [89], and Boeing's MACREE [90], were developed with the goal of improving the solar cycle modulation of the GCRs.

The CHIME model is based on measurements taken on the CRRES satellite. Besides the solar cycle modulation, the major difference between CHIME and the old CREME model is the particle flux database. The low energy enhancements resulting from medium solar events are not part of the CHIME GCR database. Instead, they are included in the solar particle event data. The GCR environment of the MACREE model is the same as that used in the old CREME

package. The authors of the Badhwar and O'Neill model added measurements taken after 1980 to the GCR database.

Tylka *et al.* [87] have implemented the improved understanding of the GCR environment [91] in the CREME96 code to simplify model selection. In the new code, the models choices are the highest level of GCRs (peak during solar minimum including the anomalous component) and the lowest levels of GCRs (during solar maximum). These two model choices define the upper and lower limits of the GCR environment in which a system must perform for a long mission. Also, users have the option of calculating GCR levels for a specific date. An improved solar cycle modulation function has been added to the CREME96.

As discussed in Section 4.2, the geomagnetic attenuation of cosmic ray particles is calculated using Störmer theory. CREME96 improves these calculations as discussed in Section 4.2. Even with the improvements, users should keep in mind that data from CRRES showed penetration of galactic particles down to very low L values during the March 1991 storm. [38] The CRRES team has concluded that Störmer theory is not adequate to describe the geomagnetic attenuation of GCRs during extreme geomagnetic storms.

5.4.3 Distribution of GCR Heavy Ions in Space

The ability of the GCR heavy ions to penetrate the Earth's magnetosphere was discussed in Sections 4.2 and 5.4.2. It is the degree of geomagnetic attenuation of the GCRs that determines their distribution in space, therefore, the level of exposure to galactic cosmic rays varies with the spacecraft orbit. Roughly, spacecraft with higher inclinations and altitudes have higher exposures to transient particles. Figure 4.2.3 illustrates the latitude dependence showing magnetic rigidity contours on a world map. The rigidity determines the energy needed by a particle to penetrate the magnetosphere.

To illustrate the exposure level of spacecraft to GCRs, GCR iron spectra predicted for solar minimum were calculated with the CREME96 model and are plotted in **Figure 5.4.3.1** for the LEO, HEO, MEO, GEO, GTO, and the EOS orbit. In general, increasing the inclination of the spacecraft orbit has a much greater effect in increasing the GCR exposure level than increasing the altitude. That is why the polar EOS orbit has high exposure to the GCRs even though the altitude is only 705 km. The figure also shows that particles with energies above

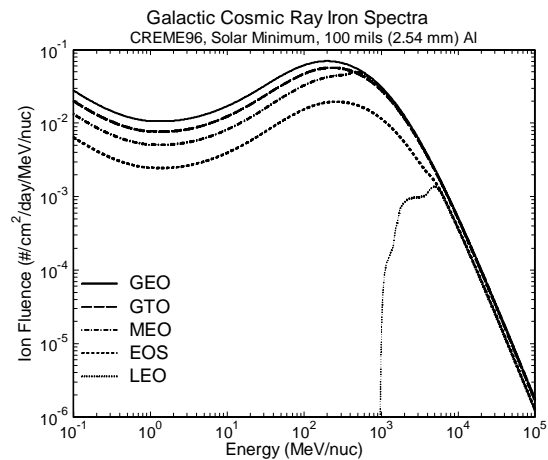


Figure 5.4.3.1: Galactic cosmic ray iron spectra for 5 orbit configurations. For even the LEO orbit, the magnetosphere cannot protect spacecraft from ions with energies greater than 6000 MeV/nuc.

6000 MeV/nuc penetrate through the magnetosphere and reach even low inclination, low altitude orbits.

As with the trapped protons, the GCRs are highly penetrating in terms of spacecraft shielding. **Figure 5.4.3.2** shows the effect of passing the interplanetary GCR iron spectrum for solar minimum through aluminum shielding. The figure shows that there is little difference between the spectra behind 100 mils (~2.5 mm) and 500 mils (~13 mm) and that shielding is only effective for ions below energies of approximately 1000 MeV/nuc. **Figure 5.4.3.3** gives the total integral LET spectra for interplanetary space for the same aluminum thicknesses, again showing the ineffectiveness of the shielding.

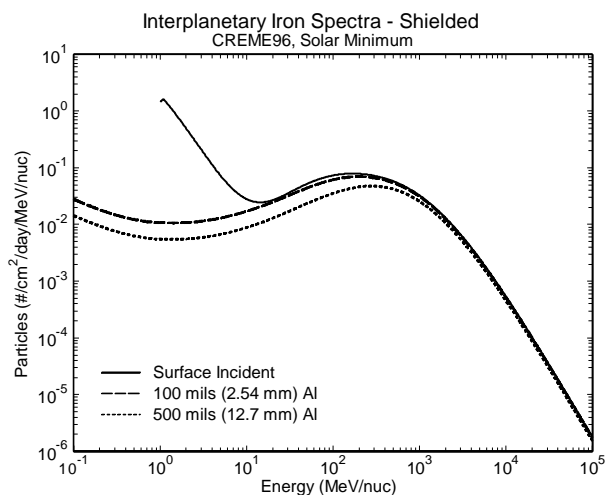


Figure 5.4.3.2: Surface incident and shielded iron spectra showing that shielding is ineffective for high energy ions.

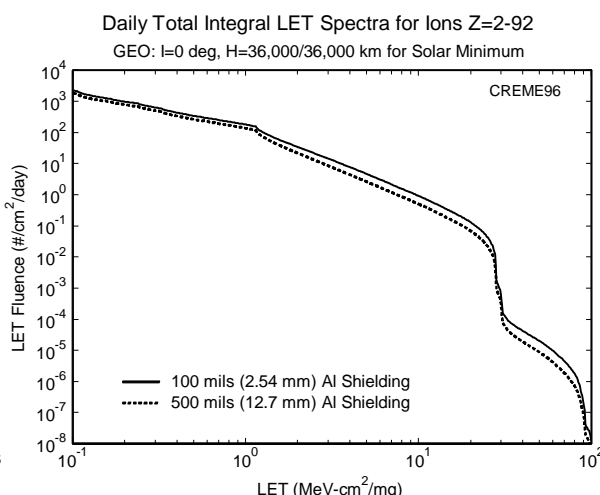


Figure 5.4.3.3: Total integral LET spectra for a geostationary orbit. Note the small decrease in LET fluence even though the shielding was increased by a factor of 5.

Figure 5.4.3.4 compares integral LET spectra calculated with CREME96 for solar minimum for the orbits specified in Section 5.1.3. Again, note the dependence on the inclination of the orbit by comparing the low altitude, polar orbit (EOS) with the low inclination orbit (LEO).

Finally, **Figure 5.4.3.5** compares total integral LETs calculated with the old CREME model for “M=1” and “M=3” and CREME96. The LET spectra are for the peak of solar minimum. The figure shows that the “M=3” model (Adam’s worst case) does overpredict and that CREME96 predicts levels even lower than the “M=1”, normal background model. The authors of CREME96 estimate that the new GCR model is accurate to 25%.

Section III of the short course will elaborate on the effect of LET on single event effects rates.

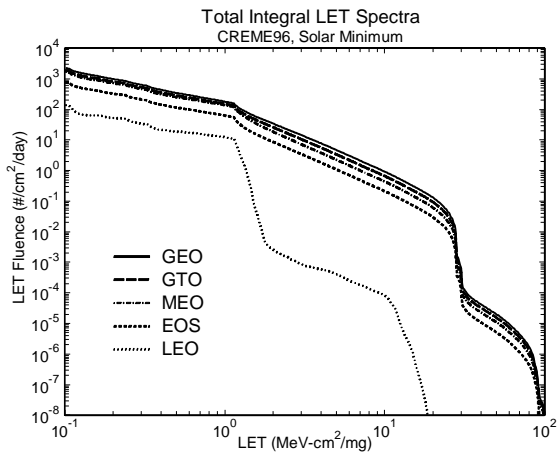


Figure 5.4.3.4: Total integral LET spectra for 5 orbits. As with the GCR fluence in Figure 5.4.3.1, attenuation by the magnetosphere is only effective for low inclination, low altitude orbits.

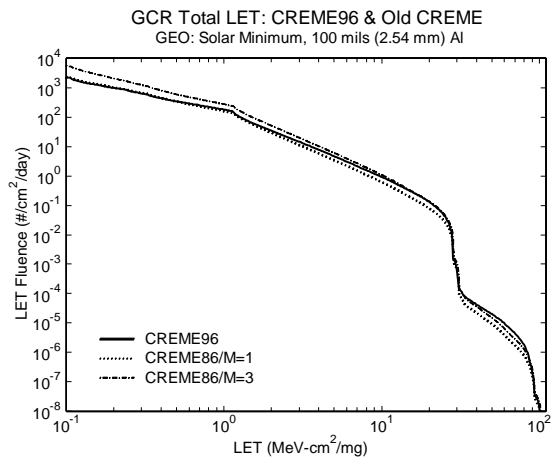


Figure 5.4.3.5: Total integral LET spectra are used to compare the old CREME with the new CREME96.

5.4.4 Problems with the Models

The most serious problem with the old CREME model was the outdated solar modulation function which has now been corrected in CREME96. The GCR model offered by the CREME96 model provides lower estimates, and it has a lower uncertainty factor than the old CREME. The only question remaining for GCR analysis in terms of radiation levels is the problem of the greatly increased accessibility of interplanetary particles during large magnetic storms. Results from CRRES indicate that present theory does not account for the level of penetration that was observed. The increased level of penetration translates into increased exposure for lower altitude, low inclination orbits increasing the risk of single event effects induced by GCRs.

5.5 Solar Wind

The composition of the solar wind was discussed in Section 2. In terms of radiation damage, the electrons are the most important constituent. The energies of the electrons are in the eV to keV range, therefore, they are stopped by very thin shields. However, they do contribute to surface erosion and must be taken into account when evaluating spacecraft deep dielectric discharging and surface charging.

5.6 Solar Particles

The particles from solar events are a concern for spacecraft designers. In fact, for spacecraft in orbits exposed to these particles, they are often the driver for setting single event effects

requirements. Experimenters have measured single event upsets on several satellites. Harboe-Sørensen *et al.* [92] measured daily SEU rates in regions of space where $L > 2$ and found that, during the October 1989 solar particle event, the rates increased by factors of 3 to 30 depending on the SRAM or DRAM memory type. Adams *et al.* [93] measured a similar response to the October 1989 event in memories on board the Meteosat-3 which was in a geostationary orbit. Mullen and Ray [94] also observed increased SEU rates during the March 1991 event in GaAs 1K RAMs on board the CRRES satellite.

For systems that must operate during a solar particle event, the effect that both the solar protons and the solar heavy-ions has on single effects rates must be evaluated. The heavier ions make only a very small contribution to the dose levels. However, single event effects induced by solar heavy ions pose a serious problem for spacecraft systems that must operate during a solar event, because the particle levels are orders of magnitude higher than the background galactic cosmic rays (see Figure 5.4.1.2). For the systems that must operate during a solar particle event, the effect that both the solar protons and the heavy-ions has on single effects rates needs to be evaluated. It is especially important to take the peak flux levels into consideration. When setting part requirements and operational guidelines, one must remember that peak solar particle conditions exist for only a small part the total mission time.

Until recently, the solar heavy ion models have not been as accurate or accessible as the models for the solar protons. Because of differences in the modeling process and the differences in particle distribution in the magnetosphere, the solar protons and solar heavy ions will be discussed separately.

Protons from solar particle events also contribute to total dose and solar cell damage especially for interplanetary missions and those at geostationary and in geostationary transfer orbits. Adams *et al.* [93] measured doses with RADFETs on the Meteosat-3 and found that doses jumped by a factor of 20 with the onset of the October 1989 event.

5.6.1 Origin of Solar Particles

In Section 2, CMEs and solar flares were discussed as they relate the to solar wind and its interaction with the Earth's magnetic field. In this section, CMEs and solar flares will be presented with respect to their particle composition.

The study of solar-terrestrial physics began with two observations. In 1859, Carrington [95] observed a brightening on the surface of the sun now known as a solar flare. He noted that a large geomagnetic storm began within a day of the flare. Another scientist, Sabine [96], published work that reported on the observation that geomagnetic activity appeared to track the 11-year sunspot cycle (see Figure 3.2.4).

Despite some troubling uncertainties, scientists have long sought to identify large solar flares as the prime cause of large, non-recurrent geomagnetic storms, transient shock wave disturbances in the solar wind, and major energetic particle events. This is what Gosling calls the “solar flare

myth”.[97] Gosling and others show that the major disturbance events observed in interplanetary space are strongly correlated to coronal mass ejections (CMEs) that have no fundamental association with flares. Although particles are often accelerated to high energies during flares, they are not directly associated with the major events observed near the Earth.

To support his theory, Gosling cites the work of Reames [2] who categorizes solar particle events into two types corresponding to two types of solar x-ray flares. In “gradual” events, the decay of the x-ray intensity takes place over many hours. In “impulsive” events, a sharp peak in x-ray emission occurs. In **Figure 5.6.1.1**, the time profiles of protons for the two types of events are plotted showing why they were labeled gradual and impulsive.

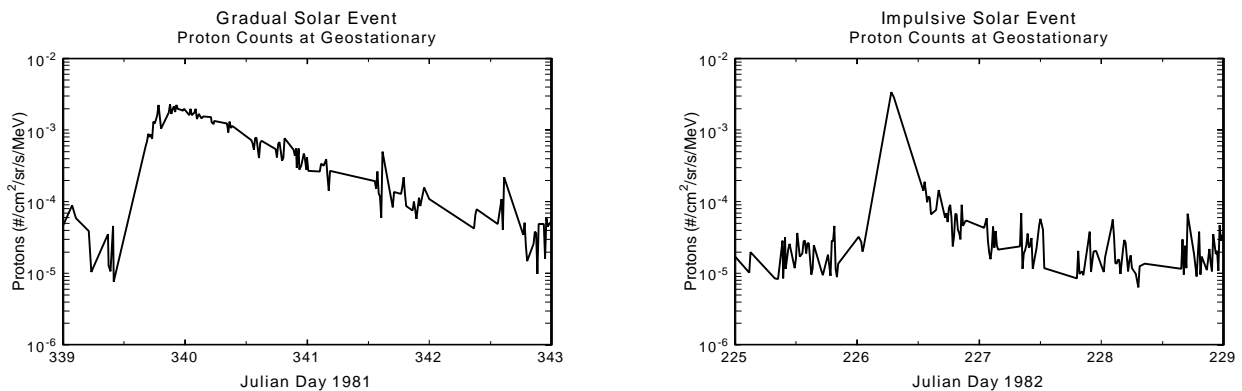


Figure 5.6.1.1: The difference in the proton counts at geostationary is a fundamental characteristic of gradual and impulsive solar events. *after Reames*

Gradual events or long duration events (LDEs) are strongly associated with CMEs. Reames has shown that particles from these events have the same elemental abundances and ionization states as the sun’s corona and the solar wind plasma. Approximately 10 gradual events per year are observed at 1 AU during solar maximum. [98] CMEs tend to be the events with the largest proton fluences.

Impulsive events are characterized by marked enhancements of heavy ions. The Fe/O ratio is approximately 1.0 in comparison to 0.1 or less in gradual events. Also, the $^3\text{He}/^4\text{He}$ ratio is 2 to 4 orders of magnitude larger than in the solar atmosphere or in the solar wind. Impulsive events originate deeper within the sun, and the particles may be directly accelerated by solar flares. Low energy electrons dominate the impulsive events, and these events have smaller proton fluxes than the gradual events. Reames has shown that the elemental abundances of particles from these events are characteristic of interactions in the flare plasma. Approximately 1000 impulsive events per year are observed a 1 AU during solar maximum. [2] Impulsive events represent the majority of the small solar particle events observed at Earth.

The solar longitude of the flare or CME largely determines the rise time of the particle fluence and the severity of the event. The solar longitude most effective for producing fluxes in the GeV/n range is close to 60° west and the solar longitude most effective in producing large solar

enhancements with energies greater than 10 MeV/n is 30° west. **Figure 5.6.1.2** compares the

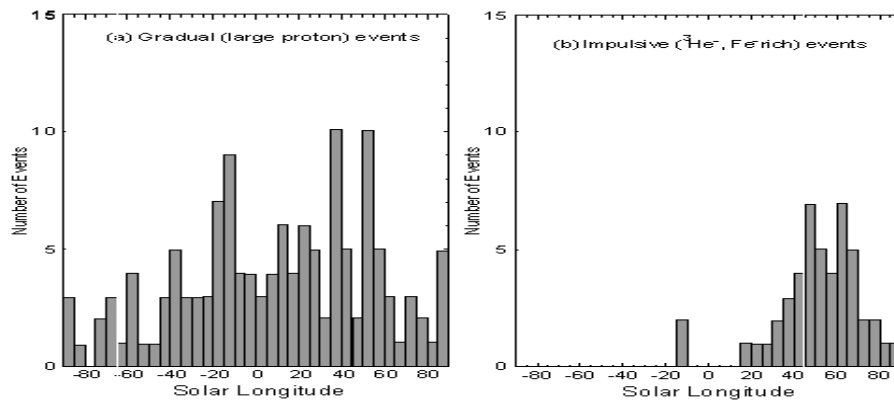


Figure 5.4.6.2: Longitudinal distribution of gradual and impulsive solar events. *after Reames*

longitudinal distributions of gradual and impulsive events. Note that the impulsive events are heavily concentrated in eastern longitudes of the sun. **Table 5.6.1.1** summarizes the properties of impulsive and gradual events.

Table 5.6.1.1: Properties of Impulsive and Gradual Events [2]

Property	Impulsive	Gradual
Particles	Electron rich	Proton rich
$^3\text{He}/^4\text{He}$	~ 1	~ 0.0005
Fe/O	~ 1	~ 0.1
H/He	~ 10	~ 100
Charge _{Fe}	~ 20	~ 14
Duration	Hours	Days
Longitude Cone	< 30 degrees	~ 180 degrees
Radio Type [2]	III, V (II)	II, IV
X-rays	Impulsive	Gradual
% of Events Producing Large Proton Events	-	CME (96%)
Solar Wind	-	Interplanetary Shock
Events/year During Solar Max	~ 1000	~ 10

The sun is never really quiet but it has been observed that there is a definite periodicity to the level of activity. Thus, the solar cycle is divided into minimum and maximum phases. **Figure 5.6.1.3** shows the solar proton events measured by the GOES spacecraft for the past three solar cycles. Superimposed on the solar event data are the number of sunspots. Note that although the number of proton events are greatly reduced during solar minimum, they still can and do occur. Also, the figure shows that the peak of proton event activity for each solar cycle usually does not correspond to the peak sunspot number.

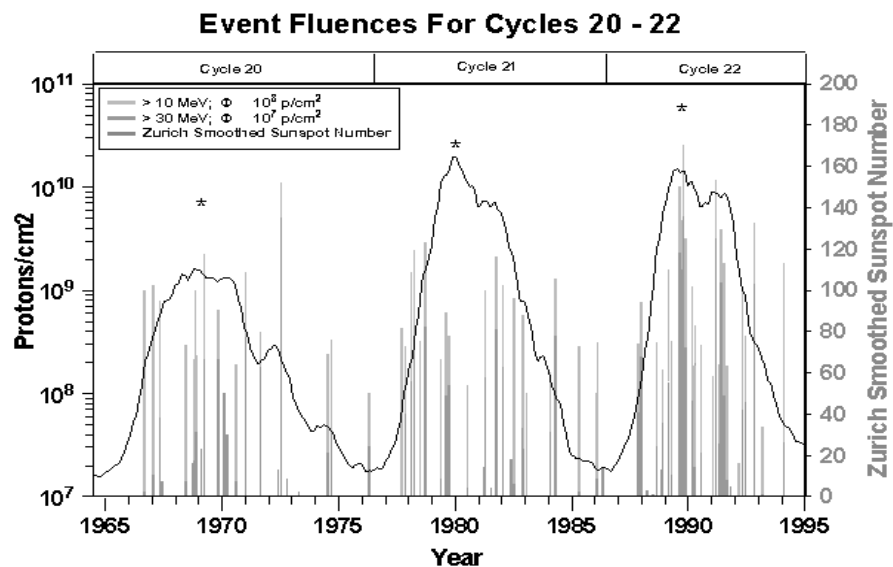
As mentioned in Section 2, it has been shown that an average 11.5 year solar cycle can be divided into four inactive years with a small number of events (solar minimum) and seven active years with a large number of events (solar maximum). During the solar minimum phase, few significant solar particle events occur; therefore, only the seven active years of the solar cycle are usually considered for spacecraft mission evaluations. Solar cycles vary in severity. For example, in cycle 21 there were no proton events as large as the August 1972 event of cycle 20; whereas, there were at least eight events in cycle 22 where the intensity exceeded 10^9 protons/cm² for energies greater than 30 MeV. The cycles also vary in total accumulated fluence as shown in **Table 5.6.1.2**.

Table 5.6.1.2: Proton Event Variation within Solar Cycles

Cycle	Start*	End	# of Months	# of Discrete Proton Events	# of Discrete Proton Producing Regions	Integrated Solar Proton Fluence	
						E > 10 MeV	E > 30 MeV
19	May 1954	Oct 1964	126	65	47	7.2×10^{10}	1.8×10^{10}
20	Nov 1964	Jun 1976	140	72	56	2.2×10^{10}	6.9×10^9
21	Jul 1976	Sep 1986	123	81	57	1.8×10^{10}	2.8×10^9
22 [4]	Oct 1986	199(?)**	**	**	**	1.0×10^{11} **	2.7×10^{10} **

*The start of each solar cycle was selected as the month after the minimum in the smoothed sunspot number. from Shea and Smart [99]

** Cycle 22 is not complete.



*Sunspot Maximum: Cycle 20: 11/1968, Cycle 21: 11/1979, Cycle 22: 11/1989 (Ref. Feynman et al. 1993) NASA/GSFC-1996

Figure 5.6.1.3: Large solar proton events for the last three solar cycles. The number of sunspots is superimposed on the graph.

The energies of the solar event protons may reach a few hundred MeV. The events last from several hours to a few days. **Figure 5.6.1.4** from Smart and Shea [100] shows a typical time profile for a solar proton event. The largest proton events often occur in association with series of major gradual flares from a single active region as it is carried across the face of the sun. For example, **Figure 5.6.1.5** shows measurements at geostationary altitude from the GOES-7 environment monitor from 19-29 October 1989. Notice that before the proton fluxes from one event have a chance to decay to background levels, the fluxes from the next event arrive.

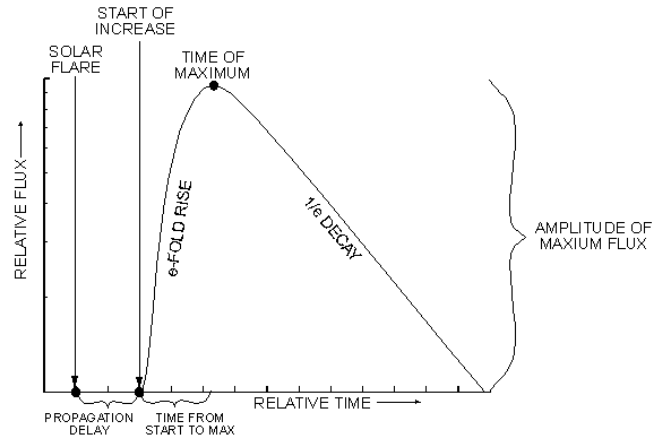


Figure 5.1.6.4: Characteristic solar particle intensity/time scale profile. *Smart and Shea*

decay to background levels, the fluxes from the next event arrive. We now know that the famous extremely large event of August 1972 was actually a series of 4 events. The spikes in Figure 5.1.4.2 indicate the sudden increase in the transient particle environment that occurs with the onset of solar particle events.

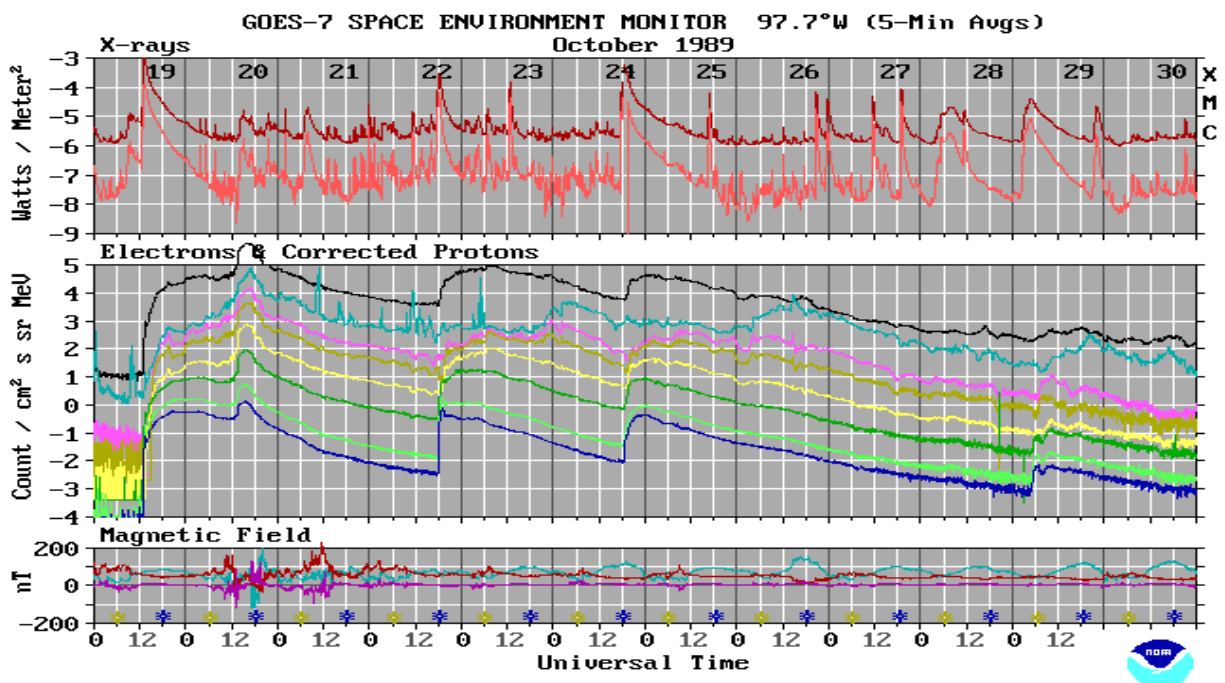


Figure 5.1.6.5: Proton counts from the GOES environment monitor during the October 1989 solar event. *NOAA/GOES*

Analysis of proton data from the 20th solar cycle by King [101] led to the conclusion that solar proton events could be classified into “ordinary” and “anomalously large”. This was based

on the fact that only one anomalously large event occurred in the 20th solar cycle - the August 1972 event. That event alone accounted for 84% of the total proton fluence at energies $E > 30$ MeV in the 20th solar cycle. However, when Feynman *et al.* [5] added cycle 19 and 21 data to the solar proton event database, they were able to conclude that individual solar proton events actually form a continuum of event severity from the smallest to the largest, blurring the distinction between ordinary and anomalously large events. Many large events similar to the August 1972 event occurred in cycle 22. Xapsos *et al.* [102] added the events of solar cycle 22 to the database and discovered that, although cycle 22 was very active, it resulted in very little deviation from the picture presented by the Feynman team.

With the increased database for solar proton events, we have learned that a “typical event” cannot be defined. The energy spectra and particle composition of both gradual and impulsive events show large variation from event to event. **Figure 5.6.1.6** shows the energy spectra for several of the largest solar cycle 22 proton events, showing the variation in both the magnitude and energy distribution of the events.

The impulsive events are heavy ion rich with energies ranging from 10s of MeV/n to 100s of GeV/n. For the 26 events observed on CRRES [84], the peak fluxes for the helium ions with energies $E > 40$ MeV/n were three times higher than the galactic cosmic ray heavy ion levels. Above energies of a few hundred MeV/n to approximately 1000 MeV/n (depending on the element), the solar particle levels merge with those of the galactic cosmic ray background.

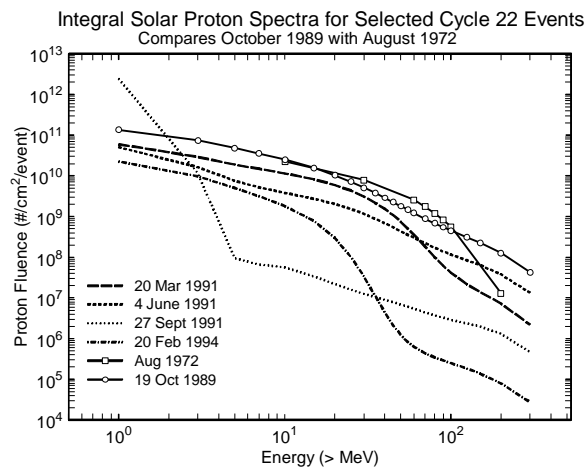


Figure 5.1.6.6: Solar proton fluence spectra for some of the largest Cycle 22 events compared to the August 1972 event. *Stassinopoulos et al.*

Previous attempts to characterize the solar heavy ions were restricted by a limited dataset at higher energies. Recently, more space data has become available. Tylka *et al.* [103], and Dietrich *et al.* [104] and used data from the University of Chicago’s Cosmic Ray Telescope on the IMP-8 and GOES satellites to study the heavy ion events. They analyzed energy spectra for C, O, and Fe using direct measurements and determined fluences in one or two energy bins for N, Ne, Mg, Si, S, Ar, and Ca. Also, alpha fluences were studied using carbon indices. This dataset provides the most comprehensive picture of high energy solar heavy ions to date. **Figure 5.6.1.7** plots energy spectra for Fe and O ions measured during the 24 October 1989 events [103]. The dashed curves at the bottom of the plot show the GCR spectrum. With their analyses, the Tylka team showed that the contribution of heavy ions to single event effect rates must not be discounted.

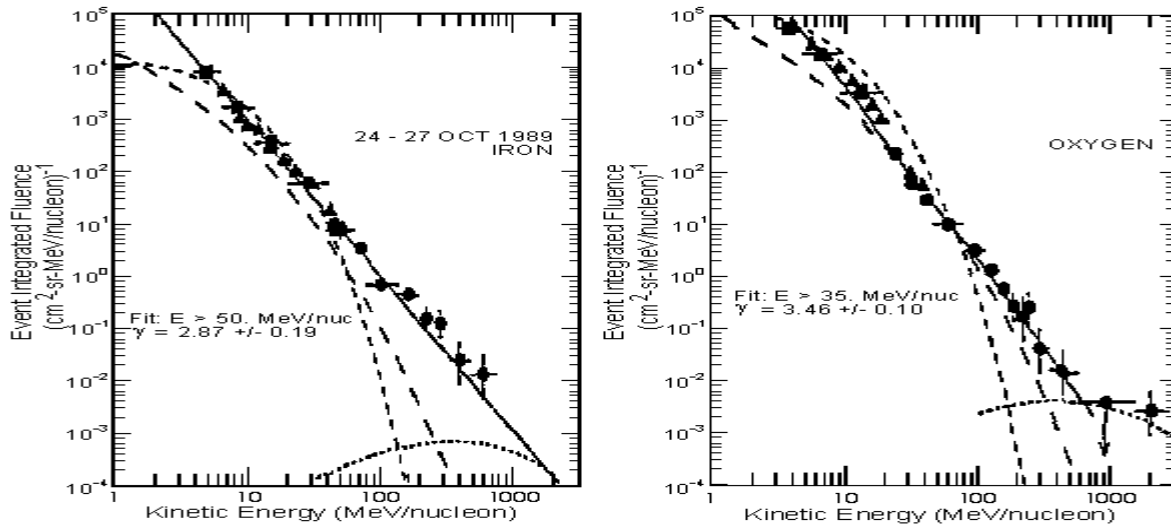


Figure 5.1.6.7: Energy spectra for FE and O ions as measured during the 24 October 1989 events. They are compared to GCR spectra (dashed curves at the bottom). *Tylka et al.*

As with the GCRs, spacecraft receive some protection from solar particles by the Earth's magnetosphere depending on their orbit. Analysis of the spacecraft exposure as a function of the geomagnetic disturbances that are often associated with solar events is especially critical. For example, CRRES data showed that solar protons reached L shell values as low as 2. [38] Also, unlike galactic heavy ions which are, for the most part, fully ionized, solar heavy ions are more often singly ionized because they pass through less matter before reaching the Earth. This must be taken into account when determining the level of penetration of the solar particles into the magnetosphere.

5.6.2 Solar Proton Models

Solar protons are a problem with respect to both dose and degradation effects and single event effects. Dose and degradation are accumulation phenomena that occur over the length of a mission, therefore, models that provide average fluence values for a mission are required for this application. Single event effects require different models that predict the peak or worst case conditions of the environment over the mission, therefore, these models must provide estimates that model the extremes of the environment.

An empirical model of the solar flare proton environment based on solar cycle 20 has existed since 1974. [105] In 1974 King introduced a probabilistic model of the solar cycle 20 events. [101] This model divides events into "ordinary" (OR) and "anomalously large" (AL) and predicts the number of AL events for a given confidence level and mission duration. Stassinopoulos developed the SOLPRO model [106] based on King's analysis. King's analysis showed that the single August 1972 solar proton event accounted for most of the proton fluence accumulated for solar cycle 20. Therefore, for a given mission duration (up to 72 months) and confidence level,

SOLPRO predicts the number of anomalously large events. The SOLPRO model only predicts proton fluence levels.

A team at JPL combined the results of several of their analyses into the JPL Solar Energetic Particle Event Environment Model (JPL92) which includes data from solar cycles 19 through 21. [107] This model consists of three parts: a statistically based model of the proton flux and fluence, a statistically based model of the helium flux and fluence, and a heavy ion composition model. The JPL work shows that, with additional event data, the distinction between anomalously large and ordinary events disappears. Hence, the JPL92 model uses the approach of predicting total solar proton fluence levels for a given confidence level and mission

duration rather than the number of events. **Figure 5.6.2.1** shows a graph of the model for proton energy greater than 30 MeV. **Figure 5.6.2.2** gives model energy spectra for a one year mission at a 95% confidence level as calculated with the SOLPRO and JPL92 models. For comparison, fluences from the August 1972 and October 1989 event are included on the plot. The JPL92 model also includes an estimate of average daily solar proton event fluences.

For single event effects analyses, the peak solar flare proton flux is required. Neither the SOLPRO nor JPL92 model contains this information. Because the CREME model was designed for single event effects applications, it provides more suitable estimates of the solar proton environment.

The solar event protons from the old CREME package were modeled on King's analysis of solar cycle 20 and estimates of worst case spectra. One of the problems of the old CREME model for solar particles was that the plethora of environment options offered (choice of 8 models) was confusing to users who were not knowledgeable about the intricacies of the environment. Fortunately, increased understanding of solar particle events and better spacecraft

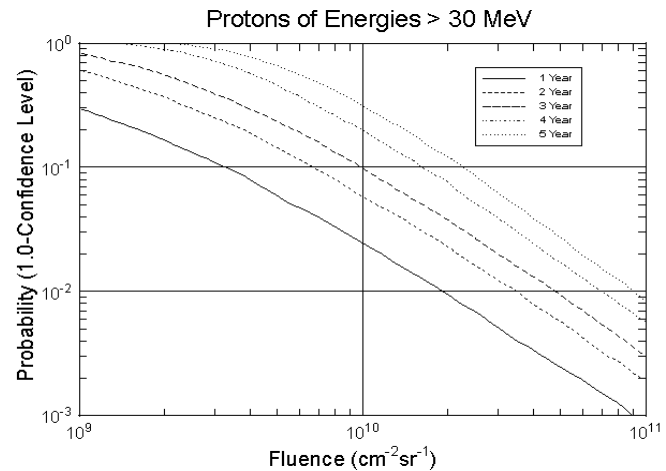


Figure 5.6.2.1: The JPL92 model gives solar proton fluences as a function of mission duration and confidence level. This plot is for $E > 30$ MeV. *Feynman et al.*

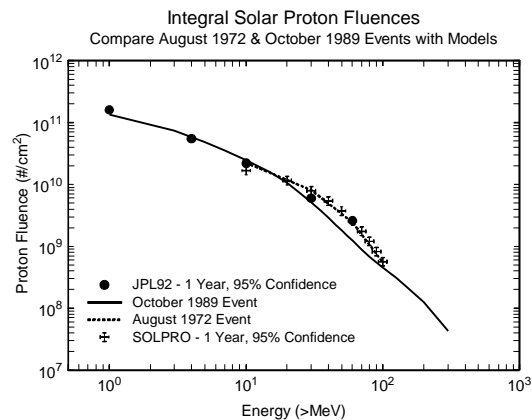


Figure 5.6.2.2: Solar proton fluences calculated with the SOLPRO and JPL92 models compared with actual event fluences.

data has greatly simplified the environment model options in the CREME96 code. This will be discussed in more detail in the next section as it relates to solar heavy ions.

Reasonable estimates of the peak flux of the protons (from the August 1972 event) can be obtained from the old CREME model by specifying the “M=9” environment and requesting element number 1 (requesting protons only). Using proton data from the IMP-8 and GOES satellites, the new CREME96 package offers three solar particle models, the average over the worst day of the solar cycle, based on the observed fluences for 20 October 1989; the average over the worst week of the solar cycle, based on 19-27 October 1989 measurements; and the average over the peak of a solar event. **Figure 5.6.2.3** compares the old CREME and CREME96 solar proton models. The figure shows that the old and new CREME models predict similar fluxes in spite of some differences in the spectral shape. The figure also shows the difference in the flux predictions as a function of the severity level that the user selects.

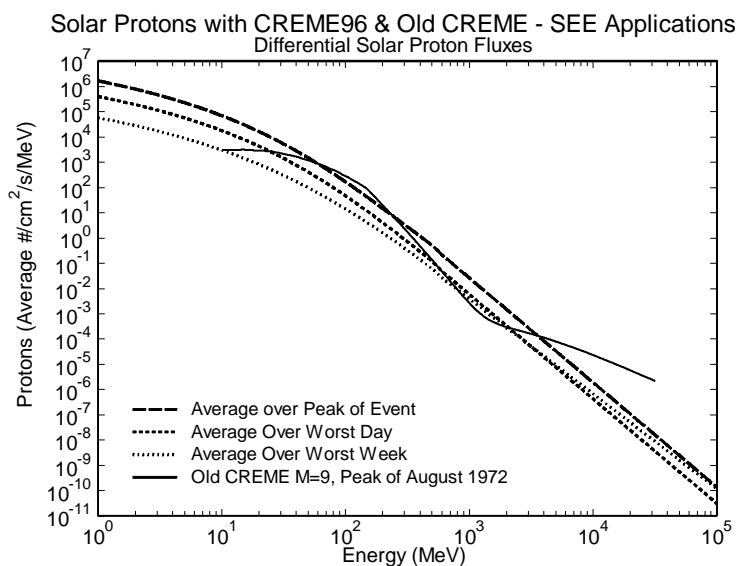


Figure 5.6.2.3: Peak solar proton spectra for single event effects applications. The spectra calculated by the old CREME and CREME96 models are similar.

Tylka *et al.* determined that the fluences measured for the October events are 99% worst case for all of the energies. [103] In future versions of the CREME96 code, the authors plan to make all of the major solar particle events in the IMP-8 dataset available.

5.6.3 Models for Heavier Solar Ions

In the past, the unavailability of an adequate dataset for the heavier solar ions has resulted in inaccurate models of the solar heavy ion environment. This has discouraged users from even attempting estimates of solar heavy ion induced single event effect rates.

Based on the assumption that the solar particle events with the highest proton fluxes are always heavy ion rich, the old CREME model calculated fluence levels for the higher energy solar heavy ions (>1 MeV) by scaling the abundances to protons. However, Reames *et al.* [108] contradict this assumption in their study of the ISEE 3 data. They found an inverse correlation between proton intensity and the iron/carbon heavy ion abundance ratio and that the composition of the event was a result of the location of the event on the sun. This would imply that any model that scales heavy ion fluences to protons is not accurate and overestimates, including the old CREME model and the CHIME model. For example, Dyer *et al.* [54] compare measured LET

from the CREDO instrument on UoSAT-3 with LET calculated with CREME for three of its solar particle models (M=5, peak ordinary flare with mean composition of an event, M=7, 10% worst case event with mean composition, and M=9, peak of the August 1972 event with mean composition). They show that, in the LET range important for single event effects analyses, all of the CREME models severely overpredict the LET levels measured during the March 1991 event.

The JPL92 model includes a definition of the solar flare heavy ion component based on the data from the IMP series of satellites. Rather than scaling the heavy ions to the proton event spectra, they use a solar event helium model combined with a heavy ion composition model. McKerracher *et al.* [109] show that the JPL92 model calculates more realistic and lower solar heavy ion induced SEE rates than the old CREME model.

Section 5.6.1 discussed the analysis of the solar heavy ion data from the IMP 8 satellite by Tylka *et al.* [103]. Their work has provided the most comprehensive set of solar heavy ion space data available. The dataset is especially important for modeling the fluences at higher energies. The Tylka team has used their results to model the solar heavy ions in the CREME96 package. As stated in Section 5.6.2, three models are offered, the average over the worst week of a solar cycle, the average over the worst day of the solar cycle, and the average over the peak of an event.

Figure 5.6.3.1 compares the old CREME and CREME96 models by plotting total integral interplanetary LET spectra for solar heavy ions of all elements $Z=2-92$. The old CREME models used in the figure are the “M=9” model, peak of the August 1972 event with a “mean composition” and the most severe model, “M=12”, the peak worst case event with “worst case” composition (see reference 86). One is immediately struck with the huge reduction in the LET predicted by the CREME96 models. The solar heavy ion model in CREME96 will provide spacecraft designers with much more reasonable predictions with which to set system design requirements.

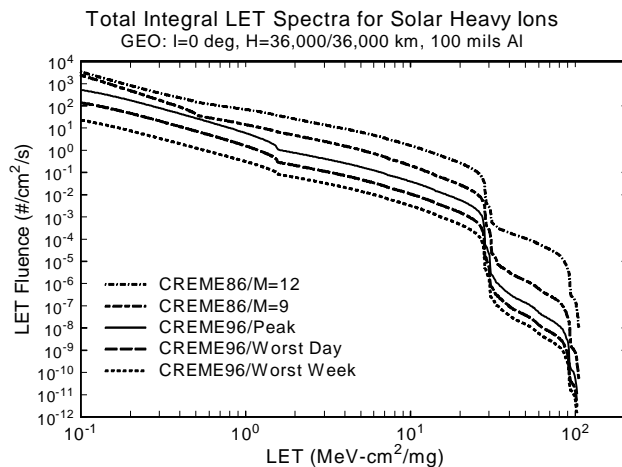


Figure 5.6.3.1: Total LET spectra for solar heavy ions as calculated with the old CREME and the CREME96 models.

5.6.4 Solar Particle Distribution in Space

As with the galactic cosmic rays, it is the degree of geomagnetic attenuation of the solar particles that determines their distribution in space, therefore, the exposure level varies with the spacecraft orbit. This section will use the CREME96 model to describe the distribution of solar

protons. Surface incident solar heavy ion levels are given in **Figure 5.6.4.1** for the LEO, GEO, and the EOS orbit. For the protons a 60°, 800 km circular orbit was added to show the inclination effect. In general, increasing the inclination of the spacecraft orbit has a much greater effect in increasing the solar proton exposure level than increasing the altitude. That is why the polar EOS orbit has high exposure to the protons even though the altitude is only 705 km. A satellite in LEO must reach approximately 50° inclination before it is exposed to solar protons under normal environment conditions. The penetration of the heavier solar ions is similar to the GCRs as shown in Section 5.4.3. As with the trapped protons and the GCRs, the solar particles are highly penetrating in terms of spacecraft shielding.

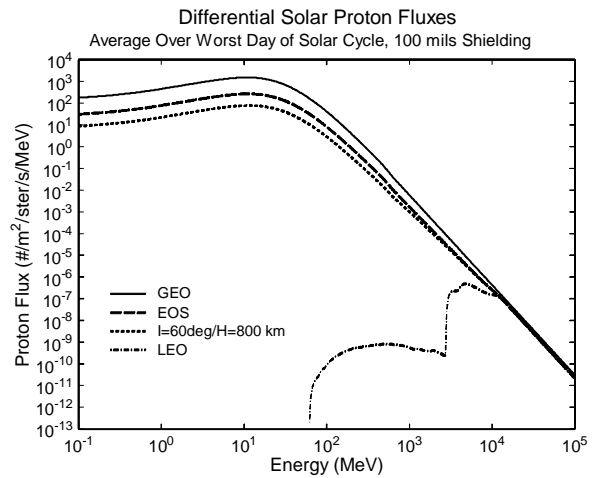


Figure 5.6.4.1: Solar proton exposure as a function of orbit. As with the GCRs, only low inclination, low altitude orbits are protected from solar event protons.

Figure 5.6.4.2 compares the average GCR and average solar heavy ion environments for a geostationary orbit in terms of total integral LET (ions Z = 2-92) as calculated with CREME96. The plot shows that, for short periods of time during a solar event, the single event effect hazard induced by the solar heavy ions greatly exceeds the GCR hazard.

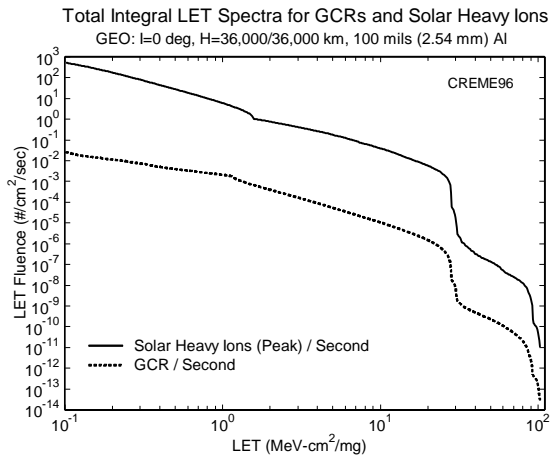


Figure 5.6.4.2: Comparison of LET fluence for GCR and solar heavy ion backgrounds.

5.6.5 Problems with the Solar Particle Models

With the release of the CREME96 code, the ability to predict solar proton and solar heavy levels for single event effects applications has greatly improved. Most of the problems with the solar particle models are in the area of providing predictions for total dose and degradation due to solar protons.

The JPL92 model was designed for interplanetary missions so it does not include the ability to take into account the attenuation of the Earth's magnetosphere. The magnetospheric attenuation used in the SOLPRO model is outdated and inaccurate. There are also problems related to the energy spectra of both of the models. The SOLPRO model is based on the August 1972 event that did not have measurements below 10 MeV. The JPL92 model is based on only three energy points, the maximum of which is 60 MeV.

The predictions for the SOLPRO and JPL92 models are in close agreement for 1-year mission durations but, as the length of the mission increases, the SOLPRO model begins to overestimate. For mission durations between approximately 18 months and 3 years, comparisons between fluence levels predicted by the JPL92 model and actual fluence accumulations show that the JPL92 model underestimates the fluence levels.

6.0 Man-made Particles [110]

While commercial, research, and some DOD satellites are not designed to survive the nuclear blast environment, it is an important consideration for strategic and tactical military applications. Several countries have the capability to test or deploy nuclear weapons introducing levels of radiation that can be lethal to spacecraft.

Man-made particles can come from atmospheric or exo-atmospheric explosions. The nuclear environment is composed of materials created by the detonation of nuclear (fission) or thermonuclear (fission-fusion) weapons. The products of the primary weapons environment are neutrons, electrons, alpha particles, fission fragments, gamma, and x-rays. The secondary environment is the blast wave, thermal radiation, and electromagnetic pulse. For atmospheric bursts, interaction with the air and ground produce more gamma radiation.

The environment from the initial nuclear radiation is transient but the effects can be transient or permanent. The transient radiation can affect both electronics and optical materials. The primary and secondary gammas and x-rays are responsible for the total ionizing dose effect on the electronic components and the gammas cause dose-rate reactions. The neutrons cause parameter degradation of electronics by disrupting atomic lattice structures and can induce single event effects. Synergistic or combined effects are also important so it is necessary to know which environments precede and which one coexist. While shielding can be of some help in mitigating

the effect of the x-ray radiation, it cannot attenuate the gamma and neutron radiation as they are extremely penetrating.

During the late 1950s and early 1960s, the US and USSR detonated nuclear devices at altitudes above 200 kilometers. The most dramatic of these tests was the US Starfish detonation on July 9, 1962. Ten known satellites were lost because of radiation damage, some immediately after the explosion. [46] The Starfish explosion injected enough fission spectrum electrons with energies up to 7 MeV to increase the fluxes in the inner Van Allen belt by at least a factor of 100. Effects were observed out to 5 Earth radii. The Starfish electrons that became trapped (modeled by Teague and Stassinopoulos [111]) dominated the inner zone environment (~ 2.8 Earth radii at the equator) for five years and were detectable for up to eight years in some regions. The regions where particles were trapped depended on the latitude of the explosion. At greater than 50 degrees latitude, the particles appeared at geostationary orbits and at less than 50 degrees latitude, in low Earth orbit domains.

7.0 The Secondary Environment

In addition to the primary radiation environment, large numbers of secondary particles are produced via collisions with other charged particles and by passing through matter. Secondary particle generation is especially important when charged particles pass through spacecraft materials and when they interact with the atmosphere at altitudes below about 75,000 feet. Section II of the Short Course will address the effect of spacecraft shielding on secondary particle generation in more detail.

7.1 Interactions with Spacecraft Materials

The dose level and background noise inside spacecraft in orbits exposed to high electron fluxes can be increased by the large number secondary photons (bremsstrahlung) produced as the electrons are slowed down and interact with the material. The secondary photons are extremely penetrating, hence, once they are produced, they are difficult to stop. The photon production is more pronounced with materials with high atomic weight.

As protons pass through a spacecraft and interact with the structure and components, they can produce neutrons, secondary protons, and spallation and fractionation products through collisions with atoms in the material. The secondary products from the nuclear collisions are especially important to consider in single event effects analyses because the secondary particles have higher linear energy transfer rates than the primary particles. Galactic cosmic rays also produce neutrons and spallation products that could, with very heavy shielding, contribute to single event effects rates.

7.2 Atmospheric Neutrons

The adverse effects of atmospheric neutrons on electronics systems at aircraft altitudes [24] have been observed. Analyses have also shown that a significant number of single event upsets on the Space Shuttle are neutron induced. Normand reviewed the existing database for large memory banks and showed that the upset rates on the ground correspond to neutron flux levels. [112] As with the protons, it is the recoil and secondary products resulting from collisions between neutrons in the environment and atoms in the material near the sensitive region of the device that are responsible for neutrons single event upsets. This implies that it is the energy of the incoming neutron that is critical in determining the ability of the neutron to cause an SEU. Therefore, models of the neutron SEU environment are in the form of neutron energy spectra.

7.2.1 Origin of Atmospheric Neutrons

As cosmic ray particles enter the top of the atmosphere, they are attenuated by interaction with nitrogen and oxygen atoms. The result is a “shower” of secondary particles and interactions created through the attenuation process. **Figure 7.2.1.1** shows the complex chain of interactions. [17] Products of the cosmic ray shower are protons, electrons, neutrons, heavy ions, muons, and pions.

Our knowledge of neutron levels comes from balloon, aircraft, and ground based measurements. **Figure 7.2.1.2** from Tabor and Normand [113] gives an overview of the radiation environment in the atmosphere as a function of altitude. Ground-based studies have shown that the variation in the neutron flux level is measurable when the altitude ranges from sea-level to mountainous regions. **Figure 7.2.1.3** shows the measured neutron flux normalized to the peak versus altitude for two energy ranges, $E = 1 - 10 \text{ MeV}$ and $10 - 100 \text{ MeV}$.

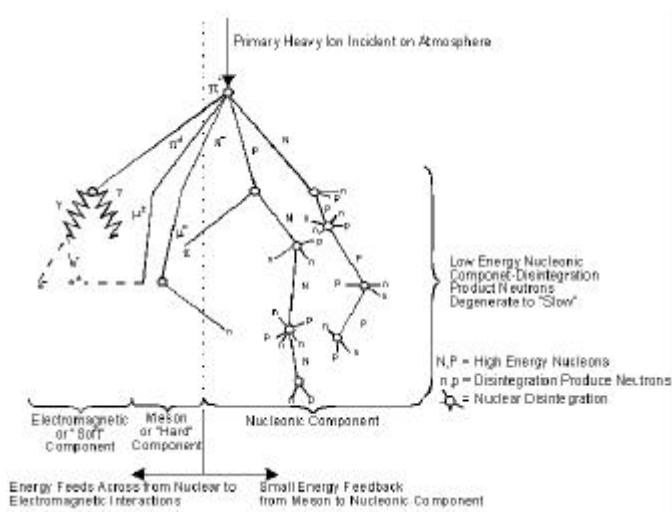


Figure 7.2.1.1: Cosmic rays hit the top of the atmosphere and disintegrate into neutrons. *Smart and Shea*

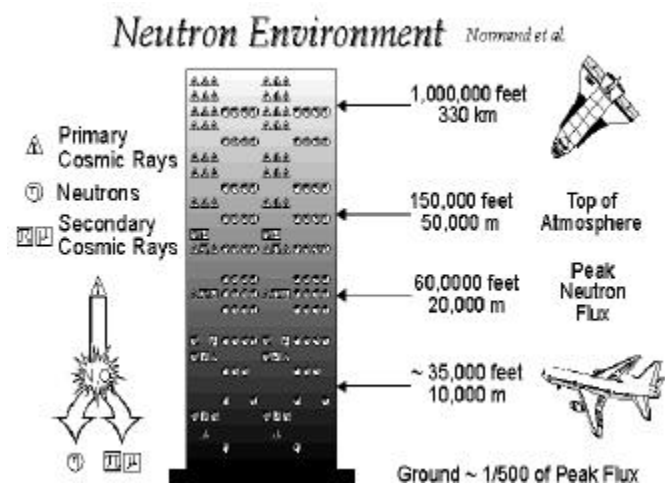


Figure 7.2.1.2: A representation of the neutron environment as a function of altitude. *Normand et al.*

Two papers published in 1984 pointed out the hazard of single event upsets at avionics altitudes. Tsao *et al.* [114] showed that, below altitudes of about 60,000 feet, secondary neutrons from cosmic ray heavy ion fragmentation are the most important contributor to SEUs. Silberberg *et al.* [115] give a method for calculating the neutron SEU rate. They also predict that SEU rates increase with enhanced solar particle backgrounds. Since that time, several flight experiments [25] have demonstrated that

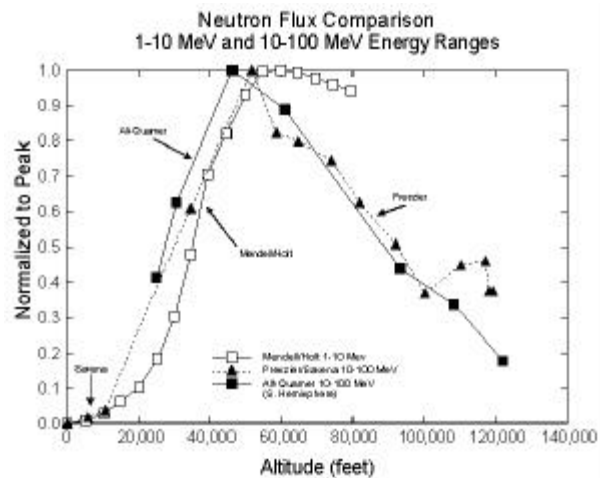


Figure 7.2.1.3: Measurements of atmospheric neutrons show the variation as a function of altitude. Normand *et al.* effects in electronics at avionics altitudes. In a study completed in 1992, [24] SEU rates measured in flight were shown to correspond with atmospheric neutron flux levels, and rates calculated using laboratory SEU data agreed with the measurements. In 1990, Dyer *et al.* demonstrated that the neutron levels were increased by 5-fold during the October 1989 solar events using measurements from the CREAM monitor on the Concorde.[116]

Because galactic cosmic rays are the primary particles that produce the secondary neutrons and protons in the atmosphere, it is the variations in the GCRs intensities that cause most of the variations observed in the secondary neutron and proton levels. For example, neutron levels rise and fall in the same 11-year solar cycle that modulates the GCRs. Also, the ability of a heavy ion to penetrate the magnetosphere is determined by its magnetic rigidity (see Section 4.2) which, in turn, is dependent on geomagnetic latitude. Magnetic disturbances occur more frequently during the active phase of the solar cycle increasing the ability of GCRs to penetrate the magnetosphere. Atmospheric conditions, especially barometric pressure, also affect the neutron levels.

7.2.2 Atmospheric Neutron Models

Studies have shown that, at altitudes less than 60,000 feet, neutrons are the dominant factor in producing SEUs. Over 70,000 feet, cosmic ray heavy ions begin to dominate the rates. [114] For avionics and on the ground, the neutrons are considered the important component, therefore, the available environment models at avionics altitudes concentrate on these particles.

As discussed in Section 4.3, two coordinate systems are used to define the neutron distribution in the atmosphere, energy-altitude-latitude and energy-atmospheric depth-magnetic rigidity. The later, the Wilson-Nealy model, [26] is more recent and more comprehensive, but it is not as easy to use as the older model. Tabor and Normand [113] believe that the older energy-altitude-latitude model is sufficiently accurate for microelectronics applications.

The energies of the neutron flux range from keV to hundreds of MeV. For SEU applications, only the energies greater than 1 MeV are significant. Because the shape of the neutron spectrum varies little over altitude, models can be greatly simplified. **Figure 7.2.2.1** gives the neutron flux as a function of altitude for the 1 to 10 MeV range. These data are based on studies by Mendall and Korff [117] and Armstrong [118]. Note that the flux peaks at about 60,000 feet which is the same as the peak of the observed SEU rates.

Figure 7.2.2.2 gives the neutron flux in the same energy range as a function of latitude averaged over longitude. The averaging does not introduce significant error

into the relationship between the flux and latitude because the flux is reasonably invariant over longitude. The latitude dependence is due to the magnetic rigidity function that was discussed in Section 4.2. This part of the model is based on measurements by Merker *et al.* [119] and the magnetic rigidity calculations came from Adams *et al.* [21] Note that the neutron flux levels off at approximately 60° inclination. Finally, **Figure 7.2.2.3** shows the neutron flux as a function of energy. Together, these three curves provide a model of the atmospheric neutron environment.

The Wilson-Nealy model offers two improvements in accuracy over the previous model. First, the magnetic rigidity cutoff is more accurate than the latitude coordinate because it avoids averaging over longitude which is required to use latitude as the cutoff parameter. Second, the Wilson-Nealy model includes solar cycle modulation. As discussed in Section 7.2.1, the neutron flux level is a function of the GCR level which is modulated by solar activity. Measurements of neutron flux levels show that the solar modulation is about 25%, however, the Wilson-Nealy model shows only about 2% variation.

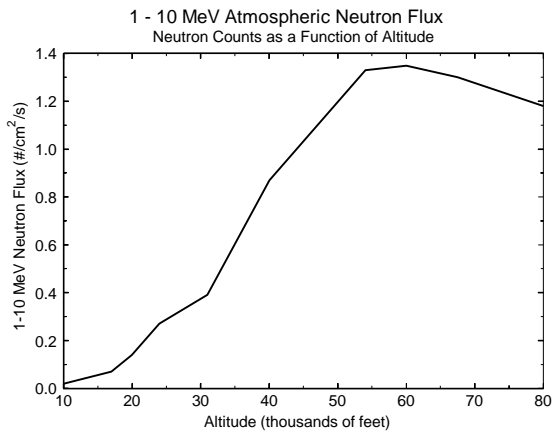


Figure 7.2.2.1: The dependence of the neutron flux on altitude is the first part of the Boeing model. *Normand et al.*

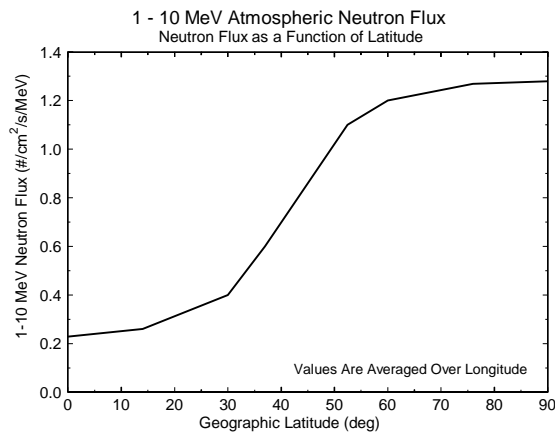


Figure 7.2.2.2: The neutron flux dependence on latitude forms the second part of the Boeing model. *Normand et al.*

The neutrons are very penetrating like the protons and heavy ions. Wilson *et al.* [26] have shown that the surface incident neutron flux is reduced by approximately 10% due to aircraft shielding.

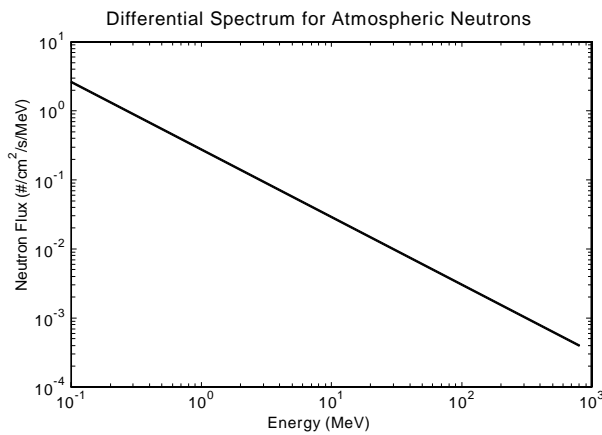


Figure 7.2.2.3: Because the neutron flux energy spectrum is invariant in latitude and altitude, it can be applied across spatial parameters. Normand *et al.*

7.2.3 Problems with the Neutron Models

The only serious problem with the two neutron models discussed in Section 7.2.2 is that they do not have the ability to predict the increases in the neutron flux due to solar events. A 5-fold increase was measured on the Concorde by Dyer *et al.* (see Section 7.2.1) during the October 1989 events. For flights at high altitudes and high latitudes, it is the neutron flux is estimated to increase by a factor of 1000-1500.

8.0 Summary and Recommendations

8.1 Summary of Environment and Available Models

Table 8.1.1 summarizes the radiation environments that must be accounted for in radiation effects analyses and the models that provide predictions of the radiation environment. **Table 8.1.2** summarizes the effects of the particles in the radiation environment on spacecraft systems. Finally, Table 8.1.3 gives information on model basics, such as, input, output, platform, and who to contact.

Table 8.1.1: Summary of Radiation Environment and Models

Particle Origin	Particle Type	Solar Cycle Effects	Variations	Orbit Configurations Affected	Models
Trapped	Protons	Solar Min-Higher Solar Max-Lower	Geomagnetic Field, Geomagnetic Storms	LEO, MEO, HEO, GTO, Transfer Orbits	AP-8 CRRESPRO Watts Pfitzer Huston et al.
	Electrons at $L < 2.8$	Solar Min-Lower Solar Max-Higher	Geomagnetic Field, Geomagnetic Storms	LEO, MEO, HEO, GTO, Transfer Orbits	AE-8 CRRESELE ESA/SEE1
	Electrons at $L > 2.8$	Masked by other effects	Local Time, Solar Rotation, Geomagnetic Storms	Polar LEO, MEO, HEO, GEO, GTO, Transfer Orbits	AE-8 CRRESELE ESA/SEE1
	Heavy Ions	Unknown	Unknown	LEO, MEO, HEO, GTO, Transfer Orbits	None
Transient	Galactic Cosmic Rays	Solar Min-Higher Solar Max-Lower	Ionization State, Orbit Attenuation, Geomagnetic Storms	Polar LEO, MEO, GEO, HEO, Interplanetary	CREME96 CHIME MACREE Badhwar & O'Neill
	Solar Protons	Solar Max- Large # of Events Solar Min- Very Few Events	Distance from Sun, Orbit Attenuation, Solar Longitude, Ionization State	LEO ($I > 45^\circ$), MEO, GEO, HEO, Interplanetary	CREME96 SOLPRO JPL92 Xapsos
	Solar Heavy Ions	Solar Max- Large # of Events Solar Min- Very Few Events	Distance from Sun, Orbit Attenuation, Solar Longitude, Ionization State	Polar LEO, MEO, GEO, GTO, Interplanetary	CREME96 JPL92 CHIME
Secondary	Neutrons- Atmospheric	Solar Min-Higher Solar Max-Lower	Barometric Pressure, Solar Events	Aircraft Altitudes, Space Shuttle Ground Level	Boeing Wilson-Nealy
	Neutrons- Spacecraft Shielding	Solar Min-Higher Solar Max-Lower	See Trapped Protons	See Trapped Protons	Dale <i>et al.</i> [120]

Table 8.1.2: Effects in Spacecraft Electronics

Particle Origin	Particle	Effect
Trapped	Protons	Total Dose SEEs Displacement Damage Solar Cell Degradation
	Electrons at L < 2.8	Total Dose Solar Cell Degradation
	Electrons at L > 2.8	Total Dose Solar Cell Degradation Electrostatic Discharging Instrument Interference (Secondary Photons)
	Heavy Ions	Possible SEEs Dose Exposure for Humans
Transient	Solar Protons	Total Dose SEEs Displacement Damage Solar Cell Degradation
	Solar Heavy Ions	SEEs
	Galactic Cosmic Rays	SEEs Dose Exposure for Humans
	Plasma Electrons	Deep Dielectric Charging
Secondary	Neutrons-Atmospheric	SEUs in Avionics
	Neutrons-Spacecraft Shielding	Displacement Damage

Table 8.1.3: Model Information

Model	Input	Output	Distribution Format	Contact	Cost
DGRF/IGRF	Lat, Lon, Alt, Date	Internal Field Magnitude	FORTRAN Source Code	NASA/GSFC NSSDC (1)	None
Olson-Pfitzer	Lat, Lon, Alt, Date, Time, Disturbance Level	External Field Magnitude	FORTRAN Source Code	NASA/GSFC NSSDC (1)	None
Tsyganenko 89	Lat, Lon, Alt, Date, Time, Disturbance Level	External Field Magnitude	FORTRAN Source Code	NASA/GSFC NSSDC (1)	None
INVARA	Lat, Lon, Alt	Internal Field Magnitude, L	FORTRAN Source Code	NASA/GSFC NSSDC (1)	None
TRARA AP-8, AE-8 Trapped Particles	Orbit Position in B,L, Energies	$\log_{10}(\text{Flux})$ (#/cm ² /s)	FORTRAN Source Code	NASA/GSFC NSSDC (1)	None
CRRESPRO Trapped Protons Solar Maximum	Orbit Parameters, Mission Duration, Magnetosphere Activity Level	Proton Fluence (#/cm ²) for Mission Duration	Binary Models, Executable Code	Gary Mullen, Air Force Phillips Laboratory (2)	None
CRRESELE Trapped Electrons Solar Maximum	Orbit Parameters, Mission Duration, Magnetosphere Activity Level	Electron Fluence (#/cm ²) for Mission Duration	Binary Models, Executable Code	Gary Mullen, Air Force Phillips Laboratory (2)	None

Model	Input	Output	Distribution Format	Contact	Cost
CRRESRAD Total Dose Solar Maximum	Orbit Parameters, Mission Duration, Magnetosphere Activity Level	Total Dose (rads-si) for Mission Duration	Binary Models, Executable Code	Gary Mullen, Air Force Phillips Laboratory (2)	None
APEXRAD Total Dose Solar Maximum	Orbit Parameters, Mission Duration, Magnetosphere Activity Level	Total Dose (rads-si) for Mission Duration	Binary Models, Executable Code	Gary Mullen, Air Force Phillips Laboratory (2)	None
SEE1 Outer Zone Electrons Solar Minimum	Lat, Lon, Alt or Orbit Parameters, Mission Duration	Electron Flux or Average Flux (#/cm ² /s)	FORTRAN Source Code	Al Vampola (3)	None
SOLPRO Solar Protons for Degradation	Mission Duration, Confidence Level	Solar Proton Fluence (#/cm ² /# of Events)	FORTRAN Source Code, Executable Code	NASA/GSFC NSSDC (1)	None
JPL SPE Solar Protons for Degradation	Mission Duration, Confidence Level, Start Date of Mission	Solar Proton Fluence (#/cm ² /Mission Duration)	FORTRAN Source Code	JPL, Joan Feynman (4)	None
CREME96 Solar Protons for SEEs	Orbit Parameters, Model	Solar Proton Flux (#/cm ² /s)	Internet Use	NRL, Allan Tylka (5)	None
CREME96 Solar Heavy Ions	Orbit Parameters, Model, Ion Range	Solar Heavy Ion Flux (#/m ² /st/s/MeV/nuc) LET Flux (#/m ² /st/s)	Internet Use	NRL, Allan Tylka (5)	None
CREME96 Galactic Cosmic Rays	Orbit Parameters, Model, Ion Range	Solar Heavy Ion Flux (#/m ² /st/s/MeV/nuc) LET Flux (#/m ² /st/s)	Internet Use	NRL, Allan Tylka (5)	None
Boeing Neutron	Alt, Lat	Neutron Flux (#/cm ² /s)	Alt, Lat, Energy Dependence Curves	Boeing, Eugene Normand (6), Literature [25]	None
Wilson-Nealy	Alt, Lat, Date	Neutron Flux (#/cm ² /s)	FORTRAN Code	NASA/Langley, John Wilson (7)	None

- (1) WEB Address: <http://nssdc.gsfc.nasa.gov.space.model/>
(2) WEB Address: <http://plcs.plh.af.mil/gps/crrespro.html>
<http://plcs.plh.af.mil/gps/crresele.html>
<http://plcs.plh.af.mil/gps/crresrad.html>
(3) Email: vampola@envnet.gpsc.nasa.gov
(4) Email: Joan.Feynman@cc2mhb.jpl.nasa.gov
(5) Email: TYLKA@crs2.nrl.navy.mil
(6) Email: eugene.normand@boeing.com
(7) Address: NASA/Langley Research Center
Building 1200, Room 211
Hampton, VA 23665-5225

8.2 Model Improvements

In spite of the monumental achievement that the present models represent, we have seen that there are shortcomings in all of the models. The most serious problems are with the AP-8 and AE-8 trapped particle models. These models were designed for simple total dose applications and not for the more complex single event effects and charging/discharging problems. The CRRESPRO and CRRESELE models offer slight improvement in that they predict fluxes for “active” times in the magnetosphere, however, their dynamic and spatial range is limited. The AP-8 model is also severely deficient in the low altitude range (<1000 km). The release of the low altitude proton model being developed under the Space Environments and Effects Program [63] should correct this problem.

The release of the CREME96 code by Tylka *et al.* [103] under the sponsorship of the Space Environments and Effects Program has corrected many of the shortcomings of the old CREME code. The most significant improvement is the solar heavy ion model which now provides predictions that are easy to obtain and are much more accurate. The only question that remains to be addressed is the increased penetration of galactic cosmic rays and solar particles during severe storms.

Finally, the solar proton fluence models for dose and degradation applications need expanded energy ranges. There should be adequate data from the GOES and IMP-8 to accomplish this.

An obstacle to new models is always the lack of space data. The authors of the new CRRES models caution that their models are based on only 14 months of data collected solely during solar maximum conditions. Daly *et al.* [53] suggest flying instruments as “hitchhikers” on small satellites as a way of obtaining space data. This could be a cost effective effort, but there are problems that must be resolved before this can become a viable alternative to dedicated environment satellites.

The biggest problem of being a “hitchhiker” on a small satellite is the severe weight restriction. Instruments must be developed that are light enough to be considered as secondary payloads while measuring the environment in the detail that is required. Another impetus for developing light-weight instruments is reducing the cost of launch. Also, the chance of being cut from the payload is less if the weight impact is minimal.

A second problem is that “hitchhiker” orbits are usually less than ideal for environment sampling. These orbits will probably not provide the coverage of a GTO type orbit and will not have the lifetime to provide the dynamic range. In other words, one or two flight opportunities cannot provide the necessary temporal and spatial coverage.

Finally, a recurring obstacle is the lack of a consistent, funded program for instrument development, for supporting flight opportunities, and for producing revised models from the measured data. The need to plan experiments to measure the environment is immediate. Mission planning for the maximum phase of the solar cycle, beginning about 1999, is well upon us. If we wish to obtain particle data for that solar cycle, we must get flight opportunities now.

9.0 Acknowledgments

This section of the Short Course and the presentation would not have been possible without the support of the staff of the NASA/GSFC's Radiation Physics Office; George Gee, Mimi Kilerlane, Daniel Nakamura, E. G. Stassinopoulos, and Craig Stauffer. Special thanks go to George Gee who showed endless patience in reformatting art for the figures and slides, to Ken Label of NASA/GSFC for his support and encouragement, and Tom Jordan for kindly editing this text and his usual excellent advice. The long list of references gives testimony to many outstanding scientists who have dedicated years to performing research and publishing in the area of space radiation environments. Most of all, I am thankful to my wonderful family for their support and encouragement; Doug for spending many nights as a single parent and providing a bottomless teapot; Joanna for organizing my hopeless mess into a library and being my sunshine, and Steven for setting a fine example of commitment and hard work.

References

- [1] E. J. Lerner, "Space Weather," Discover - The World of Science, pp. 45-61, August 1995.
- [2] D. V. Reames, "Solar Energetic Particles: A Paradigm Shift," *Revs. Geophys. (Suppl.)*, 33, 585, 1995.
- [3] J. M. Nash, "Cosmic Storms Coming," TIME, pp. 54-55, September 9, 1996.
- [4] E. G. Stassinopoulos, G. J. Brucker, D. W. Nakamura, C. A. Stauffer, G. B. Gee, and J. L. Barth, "Solar Flare Proton Evaluation at Geostationary Orbits for Engineering Applications," *IEEE Trans. on Nucl. Science*, Vol. 43, No. 2, pp. 369-382, April 1996.
- [5] J. Feynman, T. P. Armstrong, L. Dao-Gibner, and S. Silverman, "New Interplanetary Proton Fluence Model," *J. Spacecraft*, Vol. 27, No. 24, pp 403-410, July-August 1990.
- [6] J. C. Cain, S. Hendricks, W. E. Daniels, and D. C. Jensen, "Computation of the Main Geomagnetic Field from Spherical Harmonic Expansion," GSFC X-611-64-316, NASA/Goddard Space Flight Center, Greenbelt, MD, October 1964.
- [7] Announcement, "Revision of International Geomagnetic Reference Field Released," *EOS Trans.*, American Geophysical Union, Vol. 77, No. 16, April 16, 1996.
- [8] W. P. Olson and K. A. Pfitzer, "Magnetospheric Magnetic Field Modeling," Annual Scientific Report, AFOSR, Contract No. F44620-75-C-0033, McDonnell Douglas Astronautics Company, Huntington Beach, CA, 1977.
- [9] N. A. Tsyganenko and A. V. Usmonov, "Determination of the Magnetospheric Current System Parameters and Development of Experimental Geomagnetic Field Models Based on Data from IMP and HEOS Satellites," *Planet. Science*, Vol. 30, No. 10, pp. 985-998, 1982.

-
- [10] N. A. Tsyganenko, "A Magnetospheric Magnetic Field Model with a Warped Tail Current Sheet," *Planet. Space Science*, Vol. 37, No. 1, pp. 5-20, 1989.
- [11] A. L. Vampola, "Solar Cycle Effects on Trapped Energetic Particles," *Journal of Spacecraft and Rockets*, pp. 416-427, Nov-Dec 1989.
- [12] J. C. Ritter, 1996 IEEE NSREC Short Course, Indian Wells, CA.
- [13] E. G. Stassinopoulos, G. J. Brucker, J. Adolphsen, J. Barth, "Radiation-Induced Anomalies in Satellites," *J. of Spacecraft and Reckets*, Vol. 33, No. 6, pp. 877-882, Nov.-Dec. 1996.
- [14] J. H. Allen, (17 April 1997), NOAA/National Geophysics Data Center, [WWW document], URL <http://julius.ngdc.noaa.gov/stp/GEOMAG/apstar.html>
- [15] C. E. McIlwain, "Magnetic Coordinates," *Radiation Trapped in the Earth's Magnetic Field*, Proc. of the Advanced Study Inst., edited by B. M. McCormac, pp. 45-61, Bergen, Norway, August 16-September 3, 1965.
- [16] A. Hassit and C. E. McIlwain, "Computer Programs for the Computation of B and L," NSSDC 67-27, National Space Science Data Center, NASA, Greenbelt, MD, May 1967.
- [17] D. F. Smart and M. A. Shea, "Galactic Cosmic Radiation and Solar Energetic Particles," Chapter 6 in *Handbook of Geophysics and the Space Environment*, p. 6-10 edited by A. S. Jursa, Hanscom, AFB, MA, 1985.
- [18] C. Störmer, "Periodische Elektronenbahnen im Felde eines Elementarmagneten und ihre Anwendung auf Brüches Modellversuche und auf Eschenhagens Elementarwellen des Erdmagnetismus," *Z. Astrophys.*, Vol. 1, pp. 237-274, 1930.
- [19] M. Roth, "The Geomagnetic Cutoff", Chapter 6, p. 6-5 in *Handbook-Development of Improved Models of the Earth's Radiation Environment*, Technical Note 1: Model Evaluation, June 28, 1989.
- [20] M. A. Shea and D. F. Smart, "A World Grid of Calculated Cosmic Ray Cutoff Vertical Rigidities for 1980.0," 18th International Cosmic Ray Conference, Conference Papers, 3: 415, 1983.
- [21] J. H. Adams, Jr., J. R. Letaw, and D. F. Smart, "Cosmic Ray Effects on Microelectronics, Part II: The Geomagnetic Cutoff Effects," NRL Memorandum Report 5099, May 26, 1993.
- [22] P. R. Boberg , A. J. Tylka, J. H. Adams, Jr., E. O. Flueckiger, and E. Kobel, "Geomagnetic Transmission of Solar Energetic Particles During the Geomagnetic Disturbances of October 1989," *Geophys. Res. Letters*, 22, 1133, 1995.
- [23] J. H. Adams, Jr., R. Silberberg, and C. H. Tsao, "Cosmic Ray Effects of Microelectronics, Part I: The Near-Earth Particle Environment," NRL Memorandum Report 4506, August 25, 1981.
- [24] A. H. Tabor and E. Normand, "Single Upset in Avionics," *IEEE Trans. on Nucl. Science*, Vol. 40, p 120, December 1993.
- [25] E. Normand, "Single Event Effects in Avionics," *IEEE Trans. on Nucl. Science*, Vol. 43, No. 2, pp. 461-474, April 1996.
- [26] J. W. Wilson, L. W. Townsend, W. Schimmerling, G. Khandelwal, F. Khan, J. E. Nealy, F. A. Cucinotta, L. C. Simonsen, J. L. Shinn, J. W. Norbury, "Radiation Safety in the Earth's Atmosphere," in NASA RP-

-
- 1257, *Transport Methods and Interactions for Space Radiations*, p. 519, December 1991. (for corrections to some model coefficients, see Reference 27)
- [27] E. Normand and T. J. Baker, "Altitude and Latitude Variations in Avionics SEU and Atmospheric Neutron Flux," *IEEE Trans. on Nucl. Science*, Vol. 40, No. 6, pp. 1484-1490, December 1993.
- [28] A. Holmes-Siedle and L. Adams, *Handbook of Radiation Effects*, p. 16, Oxford University Press, Oxford, 1993.
- [29] A. R. Frederickson, "Upsets Related to Spacecraft Charging," *IEEE Trans. on Nucl. Science*, Vol. 43, No. 2, pp. 426-441, April 1996.
- [30] M. D. Violet and A. R. Frederickson, "Spacecraft Anomalies on the CRRES Satellite Correlated with the Environment and Insulator Samples," *IEEE Trans. on Nucl. Science*, Vol. 40, No. 6, pp. 1512-1520, December 1993.
- [31] J. Lamarie, (17 April 1997), Belgisch Instituut voor Ruimte-Aëronomie/Institut d'Aéronomie Spatiale de Belgique (BIRA/IASB), Magnetosphere, [WWW document], URL <http://www.oma.be/BIRA-IASB/welcome3.html>
- [32] W. N. Spejldvik and P. L. Rothwell, *The Radiation Belts*, Chapter 5 in *Handbook of Geophysics and the Space Environment*, p. 5-1 - 5-55 edited by A. S. Jursa, Hanscom, AFB, MA, 1985.
- [33] L. Störmer, *Polar Aurora*, Clarendon, Press, Oxford, 1955.
- [34] H. Alfvén and C. G. Fälthammar, *Cosmical Electrodynamics*, Clarendon Press, Oxford, 1963.
- [35] J. G. Roederer, *Physics and Chemistry in Space, Vol. 2, Dynamics of Geomagnetically Trapped Radiation*, Springer-Verlag, New York, 1970.
- [36] M. Schulz and L. J. Lanzerotti, *Physics and Chemistry in Space, Vol. 7, Particle Diffusion in the Radiation Belts*, Springer-Verlag, New York, 1974.
- [37] D. Boucher, S. Bourdairé, and T. Beutier, "Dynamic Modeling of Trapped Particles," *IEEE Trans. on Nucl. Science*, Vol. 43, No. 2, pp. 416-425, April 1996.
- [38] M. S. Gussenhoven, E. G. Mullen, and D. H. Brautigam, "Improved Understanding of the Earth's Radiation Belts from the CRRES Satellite," *IEEE Trans. on Nucl. Science*, Vol. 43, No. 2, April 1996.
- [39] W. Blanton, (17 April 1997), Air Force Phillips Laboratory/Space Effects Division/Geophysics Directorate, PL GEOSPACE Examples, [WWW document], URL http://www.plh.af.mil/gps/geospace_examples16.gif
- [40] C. S. Dyer, A. J. Sims, P. R. Truscott, C. Peerless, and C. Underwood, "Temporal Variations in the New Proton Belt Created in March 1991 Observed Using the CREAM and CREDO Instruments," *Advances in Space Res.*, Vol. 17, No. 2, pp. (2) 159-(2)162, 1996.
- [41] E. I. Diabog, (17 April 1997), Institute of Nuclear Physics/Moscow State University, "Report on the International Workshop for Physical and Empirical Models at Dubna," [WWW document], URL <http://wings.machaon.ru/inp50/english/dubna.html>
- [42] M. S. Gussenhoven, E. G. Mullen, and E. Holeman, "Radiation Belt Dynamics During Solar Minimum," *IEEE Trans. on Nucl. Science*, Vol. 36, No. 6, pp. 2008-2014, December 1989.

-
- [43] E. J. Daly, A. Hilgers, G. Drolshagen, and H. D. R. Evans, (17 April, 1997), ESA/ESTEC, "Space Environment Analysis: Experience and Trends," [WWW document], URL <http://www.estec.esa.nl/CONFANNOUN/96a09/Abstracts/abstract45/paper/>
- [44] S. Kanekal, (17 April 1997), NASA/Goddard Space Flight Center, SAMPEX Science, [WWW document], URL <http://lepsam.gsfc.nasa.gov/www/science.html>
- [45] H. H. Heckman and G. H. Nakano, "Direct Observation of Mirroring Protons in the South Atlantic Anomaly," *Space Res.* V, p. 329, 1965.
- [46] J. I. Vette, "The NASA/National Space Science Data Center Trapped Radiation Environment Model Program (1964-1991)," NSSDC 91-29, NASA/Goddard Space Flight Center, National Space Science Data Center, Greenbelt, MD, November 1991.
- [47] G. Knoll, K. Holzer, and G. Schmidtke, "Spatial Shift of the South Atlantic Anomaly," *J. of Geophysical Res.*, Vol. 82, No. 32, p. 7A0697, November 1, 1977.
- [48] D. M. Sawyer and J. I. Vette, "AP-8 Trapped Proton Environment for Solar Maximum and Solar Minimum," NSSDC/WDC-A-R&S, 76-06, NASA/Goddard Space Flight Center, Greenbelt, MD, December 1976.
- [49] J. I. Vette, "The AE-8 Trapped Electron Model Environment," NSSDC/WDC-A-R&S 91-24, NASA/Goddard Space Flight Center, Greenbelt, MD, November 1991.
- [50] K. A. LaBel, P. Marshall, C. Dale, C. M. Crabtree, E. G. Stassinopoulos, J. T. Miller, and M. M. Gates, "SEDS Mil-STD-1773 Fiber Optic Data Bus: Proton Irradiation Test Results and Spaceflight SEU Data," *IEEE Trans. on Nucl. Science*, Vol. 40, No. 6, pp. 1638-1644, December 1993.
- [51] R. Mangeret, T. Carrière, J. Beaucour, and T. M. Jordan, "Effects of Materials and/or Structure of Electronic Devices," *IEEE Trans. on Nucl. Science*, Vol. 42, No. 6, pp. 2665-2670, December 1996.
- [52] W. C. Fan, C. R. Drumm, S. B. Roeske, and G. J. Scrivner, "Shielding Considerations for Satellite Microelectronics," *IEEE Trans. on Nucl. Science*, Vol. 43, No. 6, pp. 2790-2796, December 1996.
- [53] E. J. Daly, J. Lemaire, D. Heynderickx, and D. J. Rodgers, "Problems with Models of the Radiation Belts," *IEEE Trans. on Nucl. Science*, Vol. 43, No. 2, pp. 403-415, April 1996.
- [54] C. S. Dyer, A. J. Sims, C. Underwood, "Measurements of the SEE Environment from Sea Level to GEO Using the CREAM and CREDO Experiments," *IEEE Trans. on Nucl. Science*, Vol. 43, No. 2, pp. 383-402, April 1996.
- [55] C. S. Dyer, A. J. Sims, P. R. Truscott, J. Farren, and C. Underwood, "Radiation Environment Measurements on Shuttle Missions Using the CREAM Experiment," *IEEE Trans. on Nucl. Science*, Vol. 39, No. 6, pp. 1809-1816, December 1992.
- [56] A. Konradi, A. C. Hardy, and W. Atwell, "Radiation Environment Models and Atmospheric Cutoff," *J. Spacecraft*, Vol. 24, p. 284, 1987.
- [57] J. W. Watts, T. A. Parnell, and H. H. Heckman, "Approximate Angular Distribution and Spectra for Geomagnetically Trapped Protons in Low-Earth Orbit," *Proc. High-Energy Radiation Background in Space*, AIP Conf. 186, AIP, New York, 1989.

-
- [58] D. Heynderickx, (17 April 1997), Belgisch Instituut voor Ruimte-Aëronomie/Institut d'Aéronomie Spatiale de Belgique (BIRA/IASB), "Trapped Radiation Environment Model Development TREND-2," [WWW document], URL <http://magnet.oma.be/trend/trend2.html>
- [59] C. I. Underwood, M. K. Oldfield, C. S. Dyer, (17 April 1997), ESA/ESTEC ESA Symposium on Environmental Modelling for Space-based Applications, "Long Term Trends in the LEO Environment as Measured by the Radiation Monitors On-board Three UoSAT-class Micro-satellites," [WWW document], URL <http://www.estec.esa.nl/CONFANNOUN/96a09/Abstracts/abstract19/>
- [60] C. S. Dyer, C. J. Watson, C. L. Peerlees, A. J. Sims, and J. Barth, "Measurements of the Radiation Environment from CREDO-II on STRV & APEX," IEEE Trans. on Nucl. Science, Vol. 43, No. 6, pp. 2751-2757, December 1996.
- [61] B. Abel, R. M. Thorne, and A. L. Vampola, "Solar Cyclic Behavior of Trapped Energetic Electrons in Earth's Inner Radiation Belt," J. Geophys. Res., Vol. 99, No. A10, p. 19427, 1994.
- [62] K. A. Pfitzer, "Radiation Dose to Man and Hardware as a Function of Atmospheric Density in the 28.5 Degree Space Station Orbit," MDSSC Rep. H5387, McDonnell Douglas Space Systems Co., Huntington Beach, CA, 1990.
- [63] D. Heynderickx, (17 April 1997), Belgisch Instituut voor Ruimte-Aëronomie/Institut d'Aéronomie Spatiale de Belgique (BIRA/IASB), Proceedings from Model Workshop, "Low Altitude Trapped Radiation Model Using TIROS/NOAA Data" by S. L. Huston, G. A. Kuck, and K. A. Pfitzer, [WWW document], URL <http://magnet.oma.be/trend/trend2.html>
- [64] D. Heynderickx and J. Lemaire, "Coordinate Systems for Mapping Low-Altitude Trapped Particle Fluxes," Proc. Taos Workshop on Earth's Trapped Particle Environments, Aug. 14-19, 1994.
- [65] J. D. Meffert and M. S. Gussenhoven, "CRRESPRO Documentation," PL-TR-94-2218, Phillips Laboratory, AFMC, Hanscom AFB, MA, 1994.
- [66] D. H. Brautigam and J. T. Bell, "CRRESELE Documentation," PL-TR-95-2128, Phillips Laboratory, AFMC, Hanscom AFB, MA, 1995.
- [67] K. J. Kerns and M. S. Gussenhoven, "CRRESRAD Documentation," PL-TR-92-2201, Phillips Laboratory, AFMC, Hanscom AFB, MA, 1992.
- [68] M. S. Gussenhoven, E. G. Mullen, M. D. Violet, C. Hein, J. Bass, and D. Madden, "CRRES High Energy Proton Flux Maps," IEEE Trans. on Nucl. Science, Vol. 40, No. 6, pp. 1450-1457, December 1993.
- [69] D. H. Brautigam, M. S. Gussenhoven, E. G. Mullen, "Quasi-Static Model of Outer Zone Electrons," IEEE Trans. on Nucl. Science, Vol. 39, No. 6, pp. 1797-1803, December 1992.
- [70] A. L. Vampola, (17 April, 1997), ESA/ESTEC, "The ESA Outer Zone Electron Model Update," [WWW document], URL <http://www.estec.esa.nl/CONFANNOUN/96a09/Abstracts/abstract34/>
- [71] M. S. Gussenhoven, E. G. Mullen, M. Sperry, K. J. Kerns, "The Effect of the March 1991 Storm on Accumulated Dose for Selected Orbits: CRRES Dose Models," IEEE Trans. on Nucl. Science, Vol. 39, No. 6, pp 1765-1772, December 1992.
- [72] M. S. Gussenhoven, E. G. Mullen, J. T. Bell, D. Madden, and E. Holeman, "APEXRAD: Low Altitude Orbit Dose as a Function of Inclination, Magnetic Activity and Solar Cycle," to be presented at IEEE/NSREC Conference, July 1997.

-
- [73] M. K. Hudson, A. D. Kotelnikov, X. Li, I. Roth, M. Temerin, J. Wygant, J. B. Blake, and M. S. Gussenhoven, "Simulation of Proton Radiation Belt Formation During the March 24, 1991 SSC," *Geophys. Res. Lett.*, Vol. 20, pp. 291-294, 1995.
- [74] D. Boucher, S. Bourdairé, and T. Beutier, "Dynamic Modeling of Trapped Particles," *IEEE Trans. on Nucl. Science*, Vol. 43, No. 2, pp. 416-425, April 1996.
- [75] C. Jacquy, J. A. Sauvaud, and J. Dandouras, "Location and Propagation of the Magnetotail Current Disruption During Substorm: Analysis and Simulation of an ISEE Multi-onset Event," *Geophys. Res. Letters*, Vol. 18, pp. 389-392, 1991.
- [76] D. Boucher, T. Beutier, and S. Bourdairé, "A Three-Dimensional Phase Space Dynamical Model of the Earth's Radiation Belts," in *Workshop on the Earth's Trapped Particle Environment*, Taos, NM, Aug 14-19, 1994.
- [77] S. Bourdairé, D. Boucher, and T. Beutier, "Modeling the Charged Particle Transport in the Earth's Internal Magnetosphere," in *Workshop of the GdR Plasmas*, Tournon, France, Apr. 10-12, 1995.
- [78] J. B. Blake and L. M. Friesen, "A Technique to Determine the Charge State of the Anomalous Low Energy Cosmic Rays," *Proc. 15th Internat. Cosmic Ray Conf. (Plovdiv)*, Vol. 2, p. 341, 1977.
- [79] N. L. Grigorov, M. A. Kondratyeva, M. I. Panasyuk, Ch. A. Tretyakova, J. H. Adams, Jr., J. B. Blake, M. Schultz, R. A. Medwaldt, and A. J. Tylka, "Evidence for Anomalous Cosmic Rays Trapped in the Magnetosphere," *Geo. Res. (Itrs.)* Vol. 18, p. 1959, 1991.
- [80] J. R. Cummings, A. C. Cummings, R. A. Mewaldt, R. S. Selesnick, and E. C. Stone, T. von Rosenvinge, J. B. Blake, "SAMPEX Measurements of Heavy Ions Trapped in the Magnetosphere," *IEEE Trans. on Nucl. Science*, Vol. 40, No. 6, pp. 1458-1462, December 1993.
- [81] A. Tylka, "Spectra and Geographical Distribution of Geomagnetically Trapped Anomalous Cosmic Rays," *Proc. 23rd Internat. Cosmic Ray Conference*, Calgary, 1993.
- [82] J. W. Cronin, T. K. Gaisser, and S. P. Swordy, "Cosmic Rays at the Energy Frontier," *Scientific American*, January 1997.
- [83] R. A. Medwaldt, "Elemental Composition and Energy Spectra of Galactic Cosmic Rays," *Proc. from Conference on Interplanetary Particle Environment*, JPL Publication 88-28, pp. 121-132, JPL, Pasadena, CA, April 15, 1988.
- [84] D. L. Chenette, J. Chen, E. Clayton, T. G. Guzik, J. P. Wefel, M. Garcia-Muñoz, C. Lapote, K. R. Pyle, K. P. Ray, E. G. Mullen, and D. A. Hardy, "The CRRES/SPACERAD Heavy Ion Model of the Environment (CHIME) for Cosmic Ray and Solar Particle Effects on Electronic and Biological Systems in Space," *IEEE Trans. on Nucl. Science*, Vol. 41, No. 6, pp. 2332-2339 December 1994.
- [85] R. B. McKibben, "Gradients of Galactic Cosmic Rays and Anomalous Components," *Proc. from Conference on Interplanetary Particle Environment*, JPL Publication 88-28, pp. 135-148, April 15, 1988.
- [86] J. H. Adams, Jr., "Cosmic Ray Effects on Microelectronics, Part IV," *NRL Memorandum Report 5901*, Naval Research Laboratory, Washington, DC, December 31, 1987.
- [87] A. J. Tylka, J. H. Adams, Jr., P. R. Boberg, W. F. Dietrich, E. O. Flueckiger, E. L. Petersen, M. A. Shea, D. F. Smart, and E. C. Smith, "CREME96: A Revision of the Cosmic Ray Effects on Micro-Electronics Code," to be presented at the IEEE/NSREC Conference in July 1997.

-
- [88] E. L. Petersen, J. C. Pickel, J. H. Adams, Jr., and E. C. Smith, "Rate Prediction for Single Event Effects - A Critique," *IEEE Trans. on Nucl. Science*, Vol. 39, No. 6, pp. 1577-1599, December 1992.
- [89] G. D. Badhwar and P. M. O'Neill, "An Improved Model of the Galactic Cosmic Radiation for Space Exploration Missions," *Nucl. Tracks Radiation Meas.*, 20, No. 3, pp. 402-410, 1992.
- [90] P. P. Majewski, E. Normand, and D. L. Oberg, "A New Solar Flare Heavy Ion Model and Its Implementation Through MACREE, An Improved Modeling Tool to Calculate Single Event Effects Rates in Space," *IEEE Trans. on Nucl. Science*, Vol. 42, No. 6, pp. 2043-2050, December 1995.
- [91] R. A. Nymmik, M. I. Panusyk, T. I. Pervark, A. A. Suslov, "A Model of Galactic Cosmic Rays," *Nucl. Tracks Radiation Meas.*, Vol. 20, No. 3, pp. 427-429, 1992.
- [92] R. Harboe-Sørensen, E. J. Daly, C. I. Underwood, J. Ward, and L. Adams, "The Behaviour of Measured SEU at Low Altitude During Periods of High Solar Activity," *IEEE Trans. on Nucl. Science*, Vol. 37, No. 6, pp. 1938-1943, December 1990.
- [93] L. Adams, E. J. Daly, R. Harboe-Sørensen, A. G. Holmes-Siedle, A. K. Ward, and R. A. Bell, "Measurements of SEU and Total Dose in Geostationary Orbit Under Normal and Solar Flare Conditions," *IEEE Trans. on Nucl. Science*, Vol. 38, No. 6, pp. 1686-1692, December 1991.
- [94] E. G. Mullen and K. P. Ray, "Microelectronics Effects as Seen on CRRES," *Adv. in Space Res.*, Vol. 14, No. 10, pp. 797-807, 1994.
- [95] R. C. Carrington, "Description of a Singular Appearance Seen on the Sun on September 1, 1859," *Mon. Not. R. Astron. Soc.* 20, 13, 1860.
- [96] E. Sabine, "On Periodical Laws Discoverable in the Mean Effects of the Larger Magnetic Disturbances," No. 2, *Phil. Trans. R. Soc. London*, 142, 103, 1852.
- [97] J. T. Gosling, "The Solar Flare Myth," *J. of Geophysical Research*, Vol. 98, No. A11, pp. 18,937-18,949, November 1, 1993.
- [98] H. V. Cane, D. V. Reames, and T. T. von Rosenvinge, "The Role of Interplanetary Shocks in the Longitude Distribution of Solar Energetic Particles," *J. of Geophys. Res.*, 93, 9555, 1988.
- [99] M. A. Shea and D. F. Smart, "Significant Proton Events of Solar Cycle 22 and a Comparison with Events of Previous Solar Cycles," *Adv. Space Res.*, Vol. 14, No. 10, pp. (10)631-(10)639, 1994.
- [100] M. A. Shea, "Intensity/Time Profiles of Solar Particle Events at One Astronomical Unit," *Proc. from Conference on Interplanetary Particle Environment*, JPL Publication 88-28, pp. 5-90, JPL, California Institute of Technology, Pasadena, CA, April 15, 1988.
- [101] J. H. King, "Solar Proton Fluences for 1977-1983 Space Missions," *J. Spacecraft and Rockets*, Vol. 11, No. 6, pp. 401-408, June 1974.
- [102] M. A. Xapsos, G. P. Summers, P. Shapiro, and E. A. Burke, "New Techniques for Predicting Solar Proton Fluences for Radiation Effects Electronics," *IEEE Trans. on Nucl. Science*, Vol. 43, No. 6, pp. 2772-2777, December 1996.
- [103] A. J. Tylka, W. F. Dietrich, P. R. Boberg, E. C. Smith, and J. H. Adams, Jr., "Single Event Upsets Caused by Solar Energetic Heavy Ions," *IEEE Trans. on Nucl. Science*, Vol. 43, No. 6, pp. 2758-2766, December 1996.

-
- [104] W. F. Dietrich, A. J. Tylka, and P. R. Boberg, "Probability Distributions of High-Energy Solar-Heavy-Ion Fluxes from IMP-8: 1973-1996," to be presented at IEEE/NSREC Conference 1997.
- [105] E. G. Stassinopoulos and J. H. King, "Empirical Solar Proton Model for Orbiting Spacecraft Applications," IEEE Trans. on Aerospace and Electronic Systems, Vol. AES-10, No. 4, pp. 442-450, July 1974.
- [106] E. G. Stassinopoulos, "SOLPRO: A Computer Code to Calculate Probabilistic Energetic Solar Flare Protons," NSSDC 74-11, NASA/Goddard Space Flight Data Center, Greenbelt, MD, April 1975.
- [107] G. Murphy, D. Croley, M. Cherng, and G. Spitale, "The JPL Solar Energetic Particle Event Environment Model," presentation material from September 1992.
- [108] D. V. Reames, H. V. Cane, and T. T. von Rosenvinge, "Energetic Particle Abundances on Solar Electron Events," The Astrophys. J., 357, pp. 259-270, July 1, 1990.
- [109] P. L. McKerracher, J. D. Kinnison, and R. H. Maurer, "Applying New Solar Particle Event Models to Interplanetary Satellite Programs," IEEE Trans. on Nucl. Science, Vol. 41, No. 6, pp. 2368-2375, December 1994.
- [110] M. Rose, J. Azarewicz, L. Cotter, H. Eisen, and J. Halpin, "Design Guidelines for Transient Radiation Effects on Army Tactical Systems," ARL-TR-702, Army Research Laboratory, Adelphi, MD, September 1996.
- [111] M. J. Teague and E. G. Stassinopoulos, "A Model of the Starfish Flux in the Inner Radiation Zone," X-601-72-487, NASA/Goddard Space Flight Center, Greenbelt, MD, December 1972.
- [112] E. Normand, "Single Event Upset at Ground Level," IEEE Trans. on Nucl. Science, Vol. 43, No. 6, pp. 2742-2750, December 1996.
- [113] A. H. Tabor and E. Normand, "Investigation and Characterization of SEU Effects and Hardening Strategies in Avionics," DNA-TR-94-123, Defense Nuclear Agency, Alexandria, VA, February 1995.
- [114] C. H. Tsao, R. Silberberg, and J. R. Letaw, "Cosmic Ray Heavy Ions At and Above 40,000 Feet," IEEE Trans. on Nucl. Science, Vol. 31, No. 6, pp. 1066-1068, December 1984.
- [115] R. Silberberg, C. H. Tsao, J. R. Letaw, "Neutron Generated Single Event Upsets," IEEE Trans. on Nucl. Science, Vol. 31, No. 6, pp. 1183-1185, December 1984.
- [116] C. S. Dyer, A. J. Sims, J. Farren, J. Stephen, "Measurements of Solar Flare Enhancements to the Single Upset Environment in the Upper Atmosphere," IEEE Trans. on Nucl. Science, Vol. 37, No. 6, pp. 1929-1937, December 1990.
- [117] R. B. Mendall and S. A. Korff, "Fast Neutron Flux in the Atmosphere," J. Geophys., 68, 5487, 1963.
- [118] T. W. Armstrong et al., "Calculation of Neutron Flux Spectra Induced in the Earth's Atmosphere by Galactic Cosmic Rays," J. Geophys. Res., 78, 2715, 1973.
- [119] M. Merker et al., "Time Dependent World-Wide Distribution of Atmospheric Neutrons and Their Products," J. Geophys. Research, 78, 2727, 1973.
- [120] C. Dale, P. Marshall, B. Cummings, L. Shamey, and A. Holland, "Displacement Damage Effects in Mixed Particle Environments for Shielded Spacecraft CCDs," IEEE Trans. on Nucl. Science, Vol. 40, No. 6, pp. 1628-1637, December 1993.